

Tribodynamic analysis of high-speed rolling element bearings in flexible multi-body environments

by
Harry Questa

Wolfson School of Mechanical, Electrical, and Manufacturing
Engineering
Loughborough University

A Doctoral Thesis submitted in partial fulfillment of the requirements for
the award of Doctor of Philosophy of Loughborough University

March 2025

Abstract

Roller bearings are critical components in electrified vehicle powertrains. They are often performance limiting, introducing NVH (Noise, Vibration and Harshness), tribological and wear challenges. With a push towards achieving zero-prototype development, the use of advanced simulation tools to accurately predict their behaviour at both component and system level is becoming more prevalent.

Modern electrified motors and transmissions operate at considerably higher speeds than traditional internal combustion powertrains. This leads to much higher lubricant entrainment velocities at the roller-race conjunction in the bearings. Consequently, the elastohydrodynamic (EHL) film can be of the same order of magnitude and even exceed that of the contact deformation predicted by the dry Hertzian assumption. This significantly influences the contact mechanics and hence total bearing stiffness.

This research presents a coupled tribological and dynamic modelling approach for high-speed rolling element bearings. Experimental studies using a novel test rig highlight the influence of the EHL film, with measured bearing motion serving as boundary conditions for tribological analyses. A coupled simulation approach is developed, integrating an implicit lubricated bearing model within a high-speed, system level, flexible multi-body dynamic model. Results at both the contact and system level are evaluated to quantify the differences between lubricated and non-lubricated analyses. An artificial neural network (ANN) is trained to predict EHL film thickness across a wide range of bearing geometries, tribological parameters and operating conditions. The ANN is then employed within the coupled simulation as a more accurate alternative to the regressed film thickness equations, with its performance evaluated against numerical and analytical approaches in terms of predictive accuracy and computational efficiency.

This multi-physics approach improves the understanding of the interaction between tribological behaviour and system dynamics. The deeper understanding of these matters will support more objective development of these modern powertrains in future to enhance their efficiency, durability and NVH refinement.

Keywords High-speed; roller bearings; tribodynamics; elastohydrodynamics; EHL; flexible multi-body dynamics; artificial neural network; ANN

Table of contents

List of figures	ix
List of tables	xiii
Nomenclature	xv
List of Abbreviations	xx
1 Introduction	1
1.1 Research Aims and Objectives	2
1.2 Contributions to Knowledge	3
1.3 Structure of Thesis	4
2 Literature Review	7
2.1 Rolling Element Bearing Introduction	7
2.2 Rolling Element Bearing Modelling	8
2.2.1 Quasi-static Bearing Models	8
2.2.2 Dynamic Bearing Models	10
2.2.3 Lubricated Dynamic Bearing Models	11
2.3 Contact Mechanics	13
2.3.1 Hertzian Contact Mechanics	13
2.3.2 Line Contacts	16
2.4 Elastohydrodynamic Lubrication	17
2.4.1 History	17
2.4.2 Numerical Methods	18
2.4.3 Starvation	20
2.4.4 Thermal EHL	21
2.4.5 Elastohydrodynamic Pressure and Film Characteristics	22
2.4.6 Lubrication Regimes	23
2.5 Artificial Neural Networks	25

2.6 Closure	27
3 Investigating the Effect of Lubrication on the Tribodynamic Behaviour of High-Speed Roller Bearings	29
3.1 Introduction	29
3.2 Workflow	30
3.2.1 Experimental Test Rig	33
3.2.2 Instrumentation	34
3.2.3 Signal Processing	36
3.2.4 Contact Mechanics at the Roller Race Conjunction	37
3.2.5 Implicit Tribological Model	38
3.2.6 Friction Calculations	40
3.3 Numerical EHL Model	42
3.3.1 Reynolds Equation	42
3.3.2 Finite Difference Formulation	45
3.3.3 Effect of Pressure on Lubricant Viscosity	46
3.3.4 Effect of Pressure on Lubricant Density	47
3.3.5 Effect of Temperature on Viscosity	47
3.3.6 1D EHL Solution Methodology	47
3.3.7 Numerical EHL Model Validation	49
3.3.8 Experimental Result Verification	49
3.4 Results and Discussion	52
3.4.1 Film Thickness and Load Across Speed Sweep	52
3.4.2 Friction	54
3.4.3 EHL Regimes	55
3.4.4 Dry vs Lubricated Tribodynamic Model	56
3.4.5 Numerical EHL Results	58
3.5 Conclusions	61
4 Modelling Lubricated Bearings in a Flexible Multi-Body Dynamic Environment	63
4.1 Introduction	63
4.2 Methodology	64
4.3 System Level Flexible Model	64
4.3.1 Lubricated Component Level Model	68
4.3.2 Representative Excitation Methodology	73
4.3.3 Co-Simulation of Coupled Models	74
4.4 Results and Discussion	79

4.4.1	Conclusions	83
5	Artificial Neural Networks for EHL Film Thickness Predictions	85
5.1	Introduction	85
5.2	Numerical vs Analytical Film Thickness Estimations at High Entrainment Velocities	86
5.3	ANN Fundamentals	87
5.3.1	Network Architecture	88
5.3.2	Forward Propogation	89
5.3.3	Backpropagation	89
5.4	Methodology	90
5.4.1	EHL Input Data Generation	92
5.4.2	ANN Structure Evaluation	95
5.4.3	Explicit Bearing Film Thickness Predictions	102
5.4.4	Implicit Bearing Film Thickness Predictions	104
5.5	Results and Discussion	104
5.5.1	ANN Structure Evaluation	104
5.5.2	Explicit Bearing Film Thickness Predictions	108
5.6	Conclusions	110
6	Conclusions and Future Works	113
6.1	Overall Conclusions	113
6.2	Contributions to Knowledge	115
6.3	Addressing the Research Questions	116
6.4	Future Works	117
	References	119

List of figures

2.1	Electrified powertrain.	8
2.2	Torque-speed characteristics of permanent magnet synchronous motor (PMSM).	9
2.3	Roller-race model for line contact.	14
2.4	Ball-race model for point contact.	14
2.5	Hertzian contact deflection.	15
2.6	Effect of dimensionless inlet distance on film thickness for starvation modelling.	21
2.7	EHL film and pressure distribution.	23
2.8	Stribeck curve and specific film thickness values.	24
3.1	Methodology overview.	31
3.2	Cylindrical roller bearing in equilibrium position.	32
3.3	Mutual separation and convergence of inner and outer races.	32
3.4	EHL film thickness and pressure distribution at contact.	34
3.5	Experimental rig schematic.	35
3.6	Accelerometer locations on test bracket.	35
3.7	Laser vibrometer locations on shaft.	36
3.8	Validation of dimensionless pressure distribution, present model (solid), Masjedi and Khonsari (dashed).	50
3.9	Validation of dimensionless film thickness distribution, present model (solid), Masjedi and Khonsari (dashed).	50
3.10	Bearing bore displacement frequency spectra.	53
3.11	Shaft displacement frequency spectra.	53
3.12	Contact load and film thickness - Outer race.	54
3.13	Film and load - EHL to hydrodynamic regime.	55
3.14	Viscous and boundary friction at the outer race contact.	56

3.15 EHL and hydrodynamic conditions during roller operation. Key: IR = Iso-viscous Rigid, VR = Viscous Rigid, VE = Viscous Elastic, IE = Iso-viscous Elastic.	57
3.16 Contact load difference between dry and lubricated model.	58
3.17 Dry and lubricated model load difference: a) 3 050 rpm, b) 14 135 rpm, c) 14 855 rpm.	59
3.18 Selected points for the numerical EHL model.	60
3.19 EHL pressure and film thickness distributions: a) Node 1, b) Node 2, c) Node 3, d) Node 4, e) Node 5, f) Node 6.	60
4.1 Flowchart of models.	65
4.2 System level model schematic.	66
4.3 Bearing schematic.	68
4.4 Dry vs lubricated roller-race contact.	69
4.5 Contact level validation.	71
4.6 PMSM torque profile and maximum and minimum torque fluctuation. .	74
4.7 Hub motor excitation model.	75
4.8 Communication vector and degrees of freedom.	76
4.9 Output port Demux blocks and degrees of freedom.	77
4.10 Input port Mux blocks and degrees of freedom.	78
4.11 Simulink® model schematic.	78
4.12 Rolling element contact stiffness - Dry vs lubricated maximum values. .	79
4.13 Rolling element contact force - Dry vs lubricated percentage increase. .	80
4.14 Inner race stiffness - Dry vs lubricated operating envelope.	81
4.15 Inner race displacement - Dry vs lubricated operating envelope.	81
4.16 Inner race acceleration - Dry vs lubricated operating envelope.	82
4.17 Rolling element contact stiffness - Dry vs lubricated minimum values. .	82
4.18 Film thickness vs contact force 21 000 rpm.	83
4.19 Film thickness vs contact force 12 500 rpm.	83
5.1 Central film thickness - EHL vs analytical.	87
5.2 ANN schematic	88
5.3 ANN data flow, models and training flowchart	91
5.4 Greenwood informed training data vs Marian et al.	94
5.5 Workflow to constrain training input data using Greenwood regimes .	96
5.6 Greenwood informed training data vs unconstrained data.	97
5.7 ANN structure to predict EHL central film thickness (9 – [14 – 14 – 14]3 – 1)	98

5.8	Bearing operating conditions vs Greenwood informed training data. . .	103
5.9	Normal contact load vs cage angular displacement	104
5.10	R^2 performance of ANN structure ($N=14$, $t=3$) using a Logistic Sigmoid activation function at each hidden layer: a) 600 points, b) 1000 points, c) 2000 points, d) 5000 points	107
5.11	ANN, numerical and analytical central film thickness comparisons. . . .	108
5.12	Central film thickness - EHL vs ANN vs analytical speed sweep. thickness comparisons at increasing rotational speeds	109

List of tables

3.1	Surface Topography Data	42
3.2	Bearing Specification	51
3.3	Lubricant and Material Properties	52
3.4	Extrapolated Film Formulae and Numerical Model Central Film Thickness Comparison	61
4.1	Cylindrical Roller Bearing Specification	73
4.2	Bearing Rheological Properties	73
4.3	Pinion Geometry	75
4.4	Gear Geometry	76
5.1	Range of ANN film thickness calculation parameters	95
5.2	Sensitivity study of ANN structure	98
5.3	Roller Bearing Parameters	102
5.4	Operating Conditions	102
5.5	R^2 performance of ANN structures using 600 data points and a LogSig activation function	105
5.6	R^2 performance of ANN structures using 600 data points and a Tanh activation function	106
5.7	R^2 performance of ANN structures using 600 data points and a Tanh activation function	106
5.8	Training time of ANN structures with LogSig activation function and 600 data points	106
5.9	Training time of ANN structures with LogSig activation function and 1000 data points	106
5.10	Training time of ANN structures with LogSig activation function and 2000 data points	106
5.11	Training time of ANN structures with LogSig activation function and 5000 data points	107

5.12 Film thickness computation methodology performance relative to the numerical solution	109
--	-----

Nomenclature

The nomenclature of all symbols used in the body of this work is given in the following sections. This work combines concepts from various research domains, including multi-body dynamics, elastohydrodynamic lubrication and computer science. Since each field has its own established notation, overlap for certain symbol invariably occurs. The nomenclature is therefore divided by chapter to maintain convention and reduce potential confusion.

Chapter 3

A_a	Asperity apparent contact area (m^2)
A	Apparent contact area (m^2)
a	Acceleration ($\text{m} \cdot \text{s}^{-2}$)
b	Half-length of the contact (mm)
C	Radial clearance (μm)
c'	Solid specific heat capacity ($\text{J} \cdot \text{kg}^{-1} \cdot \text{K}^{-1}$)
D_r	Diameter of roller (mm)
D_p	Pitch diameter (mm)
E_r	Equivalent (reduced) elastic modulus (Pa)
F_x	Radial load in x-direction (N)
F_y	Radial load in y-direction (N)
f	Total friction (N)
f_b	Boundary friction (N)
f_v	Viscous friction (N)
f_{bpi}	Ball pass frequency of inner race (Hz)
f_{bpo}	Ball pass frequency of outer race (Hz)
f_{shaft}	Shaft rotational frequency (Hz)
G^*	Dimensionless equivalent geometry (-)
h_c	Central film thickness (m)
k	Stiffness ($\text{N} \cdot \text{m}^{-1}$)
K	Lubricant thermal conductivity ($\text{W} \cdot \text{m}^{-1} \cdot \text{K}^{-1}$)
L	Roller length (mm)
n	Exponent of localized deflection (-)
N	Number of rolling elements (-)
p	Contact pressure (Pa)
\bar{p}	Average pressure at the apparent contact (Pa)
r_{in}	Radius of inner race (mm)
R_{zx}	Equivalent radius of contact (mm)
u	Speed of entraining motion ($\text{m} \cdot \text{s}^{-1}$)
U^*	Dimensionless speed parameter (-)
v	Velocity ($\text{m} \cdot \text{s}^{-1}$)
W	Contact load (N)

W^*	Dimensionless load parameter (-)
W_a	Asperity load (N)
x	Displacement in x-direction (m)
x_c	Conjunction x-coordinate (-)
y	Displacement in y-direction (m)
y_c	Conjunction y-coordinate (-)

Greek Symbols

θ	Angular position (rad)
α	Pressure viscosity coefficient ($m^2 \cdot N^{-1}$)
δ	Contact deflection (m)
κ	Average asperity tip radius of curvature (m)
λ	Stribeck parameter (-)
η_0	Atmospheric lubricant dynamic viscosity ($Pa \cdot s$)
η	Lubricant dynamic viscosity ($Pa \cdot s$)
ρ	Lubricant density ($kg \cdot m^{-3}$)
ρ_0	Atmospheric lubricant density ($kg \cdot m^{-3}$)
ρ'	Solid density ($kg \cdot m^{-3}$)
σ	Composite surface roughness (m)
ς	Boundary shear strength of asperities (-)
τ_0	Eyring stress (Pa)
ω_c	Angular velocity of cage ($rad \cdot s^{-1}$)
ω_{ri}	Angular velocity of inner race ($rad \cdot s^{-1}$)
ω_s	Angular velocity of shaft ($rad \cdot s^{-1}$)
γ	Relaxation factor (-)
ζ	Asperity density (m^{-2})

Chapter 4

C	Radial clearance (m)
d	Body material damping ($\text{N} \cdot \text{s m}^{-1}$)
E	Elastic modulus (Pa)
E_r	Equivalent (reduced) elastic modulus (Pa)
F_d	Damping force (N)
f_{damp}	Damping factor (-)
f_F	Force vector (N)
f_M	Moment vector ($\text{N} \cdot \text{m}$)
f	Force on partial mass (N)
f^a	External loads (N)
f^*	Non-linear excitation force (N)
G^*	Dimensionless equivalent geometry (-)
h_c	Central film thickness (m)
I_C	Inertia tensor of partial mass ($\text{kg} \cdot \text{m}^2$)
K	Body stiffness matrix ($\text{N} \cdot \text{m}^{-1}$)
k	Body material stiffness ($\text{N} \cdot \text{m}^{-1}$)
K_c	Contact stiffness ($\text{N} \cdot \text{m}^{-1}$)
K_b	Total bearing stiffness ($\text{N} \cdot \text{m}^{-1}$)
K_{EHL}	EHL film stiffness ($\text{N} \cdot \text{m}^{-1}$)
l_a	Active length of roller (m)
l	Length of roller slice (m)
m	Mass of partial mass (kg)
M	Mass matrix of body (kg)
N	Partial mass number (-)
n	Degree of freedom (-)
p^*	Non-linear inertia terms ($\text{kg} \cdot \text{m}^2$)
q	Displacement (m)
\ddot{q}	Velocity ($\text{m} \cdot \text{s}^{-1}$)
\ddot{q}	Acceleration ($\text{m} \cdot \text{s}^{-2}$)
R	Bearing inner race radius (m)
r	Roller radius (m)
R_r	Equivalent radius of contact (m)

s	Slice number (–)
T	Total contact moment ($\text{N} \cdot \text{m}$)
u_t	Translational displacement of partial mass (m)
U^*	Dimensionless speed parameter (–)
W	Total contact load (N)
w	Force per unit length ($\text{N} \cdot \text{m}^{-1}$)
x	Displacement in x-direction (m)
x_c	Conjunction x-coordinate (–)
y	Displacement in y-direction (m)
y_c	Conjunction y-coordinate (–)
z	Displacement in z-direction (m)

Greek Symbols

θ	Roller angular displacement (rad)
\emptyset	Rotational displacement of partial mass (rad)
α	Pressure viscosity coefficient ($\text{m}^2 \cdot \text{N}^{-1}$)
δ	Contact deformation (m)
δ_m	Material deformation (m)
η_0	Atmospheric lubricant dynamic viscosity ($\text{Pa} \cdot \text{s}$)
ρ_0	Lubricant inlet density ($\text{kg} \cdot \text{m}^{-3}$)
ω	Angular velocity of shaft (rad)

List of Abbreviations

ANN	Artificial Neural Network
AI	Artificial Intelligence
BEVs	Battery Electric Vehicles
DOF	Degree of Freedom
EHL	Elastohydrodynamic Lubrication
FEM	Finite Element Method
FMBD	Flexible Multi-Body Dynamics
IE	Isoviscous Elastic
IR	Isoviscous Rigid
LHD	Latin Hypercube Design
LHS	Latin Hypercube Sampling
ML	Machine Learning
MSE	Mean Squared Error
NVH	Noise, Vibration and Harshness
PE	Piezoviscous Elastic
PHEVs	Plug-In Hybrid Electric Vehicles
PR	Piezoviscous Elastic
PINNs	Physics Informed Neural Networks
STFFT	Short-Time Fast-Fourier Transform

Chapter 1

Introduction

The automotive industry is transitioning into the next phase of powertrain technology. As automotive manufacturers are forced to meet tightening fleet-wide emissions regulations, the electrified vehicle market share is increasing. The European Union (EU) has established ambitious policy [1], mandating that all new cars and vans sold in Europe be zero-emission by 2035 as part of a broader strategy to achieve climate neutrality by 2050. The EU aims to have electrified vehicles - both Battery Electric Vehicles (BEVs) and Plug-in Hybrid Electric Vehicles (PHEVs) - make up 80 % of its automotive market share by 2030. In China, government subsidies and investment in battery technology is also yielding a rapid advancement in electrified vehicle adoption - primarily in the passenger car segment. Whilst the direction of the industry remains susceptible to geopolitical and market influences, it is clear that future powertrains will rely on electrification.

To achieve high-efficiency and adhere to packaging constraints, modern electrified powertrains utilize ultra-high speed and low load motors [2]. These motors introduce new challenges regarding NVH (Noise, Vibration and Harshness) and the tribology of interacting conjunctions. The compact, lightweight and efficient motors operate under significantly different working conditions and are subject to different underlying physics; such as regime of lubrication, dynamic response and magneto-mechanical interactions. This style of powertrain architecture therefore involves high-speed rolling element bearing operation in both the motor and transmission.

These bearings are crucial structural components and their dynamic response significantly affects the behaviour of the interconnected structures. The dynamic behaviour of the bearing prevails the force transmission from the excitation source to the housing and structure. It also influences the tribological contact conditions between rollers and raceways.

With a trend towards cost saving zero-prototype development, the use of simulation tools in modern powertrain development is growing. Multi-system vehicle powertrain

concepts are pushing complexity of simulation models and this requires accurate and robust component level understanding. Performance characteristics of the bearings, such as NVH, friction, and wear must be accurately modelled at the development stage to ensure full system success.

1.1 Research Aims and Objectives

The primary aim of this work is to investigate the interaction between tribology and dynamics in rolling element bearings, with particular focus on the significance of this multi-physics interaction in high-speed automotive powertrain applications. With rotational speeds up to 25 000 *rpm*, the entrainment velocity of lubricant into the roller-race contact is significant, and conventional dry analyses may no longer be valid. Specifically, this work examines the influence of the elastohydrodynamic (EHL) film, and assesses the necessity of its implicit inclusion in dynamic bearing modelling within flexible multi body environments. The research also aims to investigate the contribution of artificial neural networks (ANNs) to tribological modelling, and if EHL film thickness prediction accuracy at high-speeds can be achieved. These research points are addressed through the following aims and objectives:

Aims

1. Investigate how the EHL film affects the contact load and stiffness of rolling element bearings at the high speed, low torque operating conditions representative of electrified vehicle powertrains.
2. Assess how implicit modelling of this film affects system dynamics at these operating conditions in a flexible, system-level model.
3. Investigate methods of calculating the central EHL film thickness, and assess if an ANN can be used to predict film thickness across a broad range of rolling element bearing input parameters.
4. Explore the possibility of employing an ANN to model tribological phenomena implicitly at the roller-race contact in an FMBD model.

Objectives

1. Develop a high-speed experimental test rig to measure bearing orbital motion as a kinematic input to tribological models. Use this to identify the required workflows

and necessary models for tribodynamic analysis, as well as analyse the influence of the EHL film on contact and component behaviour.

2. Develop a lubricated component bearing model, considering the EHL film implicitly at the contact between rolling elements and raceways.
3. Embed the lubricated bearing model within a flexible multi-body dynamic model to assess the influence of the EHL film on the dynamic response of the system.
4. Develop an artificial neural network, capable of computing central EHL film thickness for a wide range of the required input parameters. Assess the computational viability of integrating this implicitly within the FMBD model.

This work was performed in collaboration with AVL List GmbH in order to disseminate the outcomes of this research in the development of commercial codes: AVL EXCITETM M and AVL EXCITETM Power Unit.

1.2 Contributions to Knowledge

The main novelties and contributions to knowledge from this thesis are summarised below:

1. A novel experimental test rig was constructed to measure the kinematic motion of a bearing at rotational speeds and loads up to 750 N and 15 000 *rpm* respectively. The bearing orbital motion was measured and used for conjunction and component level tribological analysis. The methodology of coupling experimental test with numerical tribological models has not been previously reported in this manner at these speeds. The outcome of this demonstrated the requirement of implicitly modelling the EHL film in future high-speed applications, since it contributed to a 149% contact load increase at 15 000 *rpm* when compared to conventional dry analyses.
2. A coupled co-simulation approach was established to implicitly consider the EHL film in roller bearings within a high-speed system-level FMBD model. The model replicates the operating conditions of a 54 kW permanent magnet synchronous motor (PMSM) coupled to a first stage gear pair, operating at speeds up to 21 000 *rpm*. This was the first time in open literature that an implicitly lubricated multi-physics bearing model has been considered in the context of electrified powertrain dynamics. The outcome of this demonstrated that the increased contact deflection, due to the lubricant film inclusion, increases total

bearing stiffness by 24.9 % at 21 000 rpm. This effectively behaves as a non-linear, speed dependant radial preload on the bearing. The contribution of this stiffness increased the natural frequency of the system, and hence affected NVH response. This proves the requirement to consider the EHL film implicitly for rolling element bearing modelling under the high speeds, low load operating conditions of electrified powertrains.

3. An ANN was trained using input data calculated using a 1D numerical EHL model. A wide value range of input variables necessary for the EHL central film thickness calculation were used to train the model. The value range was consistent with common machine element contacts, with its applicability also extending to gear pairs and cam contacts. The novel methodology of constraining the training data using the Greenwood regime ensured high data quality whilst only requiring 600 training data points. The ANN achieved an MSE of $3.89 \times 10^{-6} \mu\text{m}^2$ when benchmarked against the numerical solution, whilst reducing calculation time by a factor of 1 500. This methodology will further contribute to the computational efficiency and accuracy of tribological ANNs.
4. The ANN was embedded within an FMBD system-level model to calculate EHL film thickness and consider it implicitly in the evaluation of the bearing and system dynamics. The film thickness evaluation achieves the accuracy of numerical models without the associated computational limitations. This modelling method of combining component level ANN within a flexible system has not been previously reported.

1.3 Structure of Thesis

The research in this thesis is presented in the following structure:

Chapter 1 introduces the topic of the thesis and provides the specific research questions that the work aims to answer.

Chapter 2 provides a review of the literature pertinent to the thesis topic, as well as covering the necessary principles required to address the research questions.

Chapter 3 presents a high-speed experimental test rig which was used to obtain kinematic boundary conditions for tribological models. The importance of including the

lubricant film in high-speed dynamic bearing models is assessed here. The governing equations for the thesis are also introduced in this chapter.

Chapter 4 integrates the tribological models used in Chapter 3 into a system-level FMBD model. High-speed simulations are performed with operating conditions representative of those in an electrified transmission. The EHL film is modelled implicitly at the roller-race conjunction, and its affect on system dynamics is evaluated.

Chapter 5 introduces an ANN to address the shortcomings of the analytical approach when estimating EHL film thickness at high speeds. The ANN is trained using a wide design space of input variables. The accuracy of the model and computational efficiency is assessed. The ANN is embedded within the dynamic system level model from Chapter 4 as an alternative approach to the analytical solution for film thickness.

Chapter 6 presents the general conclusions of the work, and outlines potential future work that could follow this research.

Chapter 2

Literature Review

This chapter reviews the literature pertinent to this research topic. It covers the development of bearing models, ranging from simple quasi-static to high-degree-of-freedom (DOF) dynamic models. Recent advancements on the implicit coupling of tribological and dynamic bearing models is then reviewed. The fundamentals of contact mechanics, essential to the research questions, are introduced alongside a discussion of contact modelling techniques. An overview of elastohydrodynamic lubrication modelling, including numerical methods, characteristics, regimes of lubrication and empirical formulae is presented. Finally, the application of artificial neural networks in the field of tribology and their impact on future modelling is explored.

2.1 Rolling Element Bearing Introduction

The term rolling element bearing encompasses both ball and roller type bearings. These common machine elements permit motion of, or about, shafts in a wide range of devices; from wheel bearings in bicycles and cars to electric motors and aircraft gas turbines. The general use of rolling element bearings occurred from the start of the Industrial Revolution, however the origin of what constitutes modern bearing design dates back as far as *ca.*1500. Leonardo Da Vinci, in his Codex Madrid, conceived a thrust ball bearing design consisting of spherical balls with conical separation elements [3]. Prior to the scientific advancements of the atomic age, the design of rolling element bearings was regarded as more an art than a science. Alas, this thesis is not a work of art (hyperbole notwithstanding), but rather an advancement of the scientific knowledge that precedes it.

In automotive transmissions, these bearings support the rotation of the shaft and the radial and axial forces applied during gear meshing. Figure 2.1 presents a 2-speed e-Axle. The motor, bearings and gear stages are labelled. Single or two stage gearing in electric transmissions mean that bearings in both the electric motors and input shaft

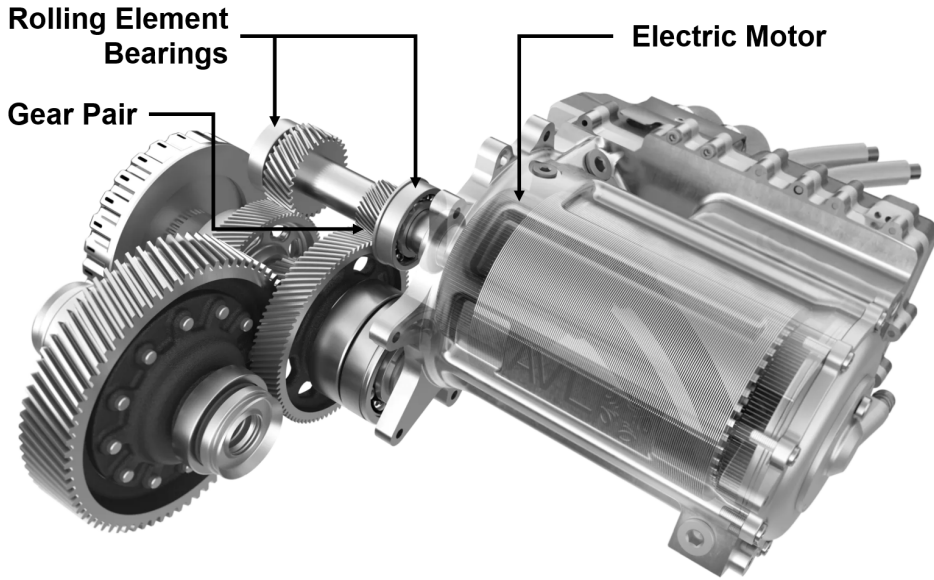


Figure 2.1 Electrified powertrain.

to the gearboxes operate under high speeds, up to 25 000 *rpm*. A typical torque/speed operating range of a 54 kW PMSM used within these electrified drive systems is shown in Figure 2.2. With such high speeds, these powertrains are able to produce high output power with relatively low torque requirements from the motor.

2.2 Rolling Element Bearing Modelling

Before the 1960's, bearing studies were primarily conducted experimentally. Empirical formulations were derived to model their performance in early work by Stribeck [4] and Lundberg and Palmgren [5] [6] amongst others. As computer technology improved post-1960, modelling theory and application grew rapidly, pioneered largely by the work of Jones [7] and Harris [8]. In the pursuit of highly efficient and reliable bearings, modelling and the need for accurate representation of the physical phenomena has become important. It is not possible to conduct experimental testing for the large array of design and operational parameters that bearings are required for, therefore experimentally validated numerical analysis is employed.

2.2.1 Quasi-static Bearing Models

Early models predicting load distribution in the rolling elements can calculate bearing stiffness and fatigue life with relative accuracy. These were primarily quasi-static and based on force equilibrium. Studies of static ball bearings under simple radial loading were performed by Stribeck [4] and improved upon by Palmgren [6] for the case of

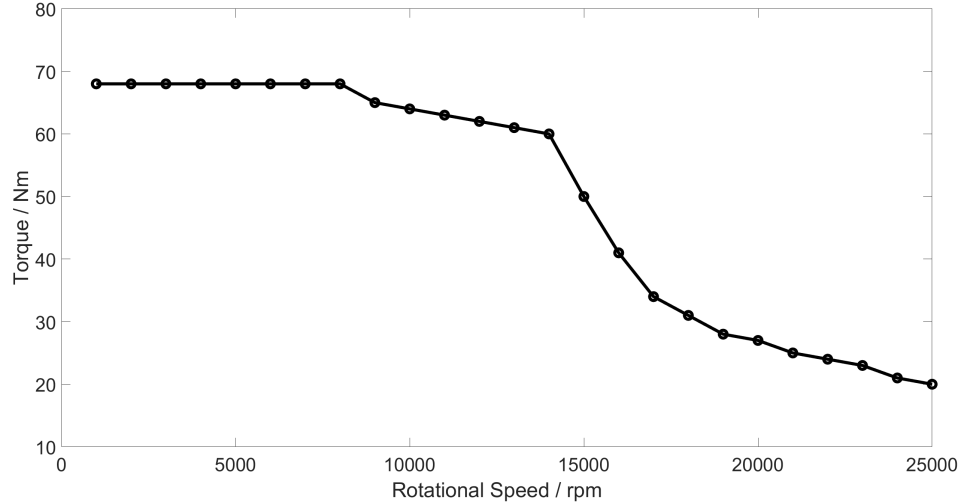


Figure 2.2 Torque-speed characteristics of permanent magnet synchronous motor (PMSM).

nominal internal clearance. Static models computing radial and axial loads based on a load distribution factor and the angular position of the roller were found using Sjovall's integration model [9], however this was only applicable if the ratio of radial to axial loads is within a particular range. Rumbarger [10] developed a model using Sjovall's integral method for purely axial loading of thrust bearings, capable of calculating moment load due to axial load eccentricity.

It was the work of Jones [7] and his general theory for load deflection analysis of bearings that extended the capability of these models. His work accounted for centrifugal and gyroscopic loading, and unlike previous models, the inner bearing race had 5 degrees of freedom (DOFs); three translational and two rotational displacements that correspond to the external forces in all three cartesian coordinates and moments applied about two. Bearing equilibrium is obtained at each rolling element by observing the load and corresponding motion of the elements. Jones also included the individual stiffness at the contact between rolling elements and raceways, using the Hertzian contact load-deflection relationship to obtain roller load based on contact deflection. This technique could be applied to both ball and roller bearings by varying the exponent of localised deflection.

Jones' model was considered limited due to the assumption that misalignment effects on the elements are negligible. Harris [8] improved on it by introducing the slicing method along the length of the rollers. This enabled determination of the load distribution along the contact in roller bearings. This method, known as the Jones-Harris method, was then applicable for highly loaded conditions and able to compute misaligned cases. Vector and matrix methods to analytically solve the quasi-static problem based on

the work of Jones and Harris were then presented for tapered roller bearing cases by Andréason [11] and Liu [12]. de Mul et al. [13] developed a model for ball and roller bearing equilibrium and stiffness matrix calculations which has the advantage of having load-deflection equations in matrix form, therefore implementation of this model is simpler.

Additional functionality has been added to these models such as the effects of thermal expansion on the load-deflection analysis [14]. Numerical models for heat generation based on frictional torque and 3-dimensional transfer through contacting elements was used to account for the expansion. It was found that expansion increased the bearing stiffness and thus natural frequency of the shaft-spindle system due to greater interference of the roller race contact. The authors also investigated the effect of ring expansion due to centrifugal force at high speeds [15] and found that natural frequency of the spindle decreased at higher rotational speeds – of particular note for high speed automotive applications.

Quasi-static models are only applicable under steady-state operating conditions; however, the static equilibrium solutions [11] [12] [16] are of use to calculate load-deflection and individual element loading within dynamic models.

2.2.2 Dynamic Bearing Models

Transient operating conditions such as acceleration or deceleration of the bearing requires dynamic modelling, particularly important for high-speed applications. In dynamic bearing models, a system of differential equations based on Newton's second law of motion are used. This allows for a time-varying input force such as eccentric rotor unbalances or fluctuating loading conditions present in transmissions. Static equilibrium solutions such as those presented are used within these models to calculate load-deflection and individual element loading.

Hitherto, a multitude of models predicting bearing dynamics have been posed for roller bearings. These investigate the dynamic effect of geometrical and topographical parameters such as surface waviness, surface defects, and the variable compliance affect. This variable compliance effect is caused by time-varying stiffness variations off the inner and outer race bearing contact as rollers change their orbital position and pass through the loaded region. Even with perfect bearing geometry free from any defects, vibration will still occur due to this [17].

Simplified 2 degree of freedom models [18] consider purely in-plane motion of rolling elements in the radial and lateral directions of the bearings for investigation of frequency response to defects [19] and the varying compliance effect [20]. Time varying

forces on cutting tool spindles and the effects on radial loading assuming no axial thrust loads or vibration can also be investigated in 2 DOF [21]. These models increase in complexity up to 5-DOF to observe moment loading and centrifugal effects [22] [23] [24]. Most of these models assume the bearing rollers and races are rigid bodies. All of these analyses also assume a dry contact between rolling elements and races which was assumed valid under the elastohydrodynamic regime of lubrication. The fluid film behaves as an amorphous, incompressible solid and generated pressures conform closely to a Hertzian distribution in the loaded region. This, however, neglects the effect of the lubricant film thickness in the contact mechanics and thus underestimates the contact deflection and hence load.

2.2.3 Lubricated Dynamic Bearing Models

Based on the experimental and numerical findings [25] [26] [27], the EHL film at the roller-race conjunction can be shown to increase the bearing stiffness, which continues to rise non-linearly with speed. It is therefore clear that the lubricant film in roller bearings operating at high speeds must be implicitly included in dynamic analyses. As stated by Bizarre et al. [28], there are few studies in the open literature that combine the stiffness and damping of an EHL contact with classical bearing dynamics.

Historically the analysis of rolling element bearings has been decoupled into two stages. The first stage is a classic dry Hertzian-contact analysis of the roller-raceway contact due to the cyclic variation in geometric bearing centre. The displacement of the bearing centre is obtained through solving equations of motion and roller load is obtained using the Hertzian load-deflection relationship. Extrapolated film thickness equations use the transient load yielded from dry analysis in a second stage study to find central film thickness. This approach does not implicitly consider the effect of the lubricant film on the prevailing bearing motion and load, which is hence underestimated. To overcome these shortcomings, quasi-static analyses employing film thickness formulae in conjunction with Hertzian contact mechanics are required.

Early lubricated bearing models use extrapolated formulae to provide a relationship between the load share and film thickness at each element's contact with the bearing raceways [29]. Aini et al. [30] implemented the extrapolated film approach from the work of Rahnejat and Gohar [29] into a five-DOF bearing equilibrium model. The work computes the deformation at each roller-race contact, combining the EHL film thickness with the elastic deformation of the contacting solids. The force-displacement relationship is shown to follow a non-linear trend.

Film shape and the elastohydrodynamic pressure profile at the contact could not be calculated in these studies, preventing more detailed analysis such as thermal and subsurface stress analysis. To determine tribological contact conditions, Mohammadpour et al. [31] employed a similar implicit tribodynamic analysis and then utilised a full numerical EHL analysis explicitly for further tribological studies.

Mohammadpour et al. [31] employed a similar implicit tribodynamic analysis and then utilised a full numerical EHL analysis explicitly for further tribological studies. In their analysis, input shaft speeds of 209 rad/s resulted in much slower entrainment velocities than are applicable for electrified powertrain analyses.

Film shape and the elastohydrodynamic pressure profile at the contact could not be calculated in these studies, preventing more detailed analysis such as thermal and subsurface stress analysis. To determine tribological contact conditions, Mohammadpour et al. [31] utilised a full numerical elastohydrodynamic analysis explicitly. Load values on an individual roller at each instantaneous position of the orbit were obtained from the implicit tribodynamic analysis and used within the numerical model.

Sopanen and Mikkola [17] modelled the influence of various surface characteristics on bearing dynamics, including contributions from surface waviness, roughness, localised and distributed effects. Their six-DOF model accounts for the Hertzian contact deformation and the EHL film implicitly within the contact. This model was embedded in a multi-body dynamic (MBD) software to utilise its mathematical capabilities. This work does not, however, demonstrate the effect that the EHL film has on bearing stiffness, and the effect on system dynamics using flexible bodies is not analysed [32]. Sawalhi and Randall [33] used a constant preload approach to imitate the stiffening effect of the film. Whilst this effective preload captures the increased contact stiffness due to the presence of the EHL film, the film thickness does not vary based on the contact conditions.

More recently, Liu and Shao [34] investigated the effects of surface waviness, including the effect of the lubricant film using an equivalent stiffness model. Nonato and Cavalca [35] presented a methodology to model EHL contacts using a set of non-linear springs and viscous dampers. Bizarre et al. [28] applied this lubricated non-linear force contact to a five-DOF model of an angular contact ball bearing. This enabled a combined solution scheme for the bearing force equilibrium and the EHL contact. The formulated system of equations was solved, achieving force equilibrium for each rotation of a bearing under constant external load. The authors of this study noted the interest of combining such models within FMBD system level models.

None of the combined models above are embedded within a system level model comprising flexible bodies, and the effect of the change in the contact stiffness due to

the lubricant film is not investigated at the system level. Furthermore, the high-speed operation and time-varying loads representative of electrified vehicle transmissions are not considered.

2.3 Contact Mechanics

A critical aspect of this work is the interface between rolling element and race; a field of engineering referred to as Contact Mechanics. The following section gives a brief introduction to the modelling and development of such models. This subject is elaborated further in Section 3.2.4 and Section 4.3.1.

2.3.1 Hertzian Contact Mechanics

Two types of contacts occur in machine elements: conformal and non-conformal. Conformal contacts occur between a concave and a convex body of similar radius, such as in journal bearings. This leads to a relatively large contact area over which load can be distributed and resultant pressures are in the order of MPa . The contact between rolling elements and races is non-conformal in nature as the contacting surfaces are both convex. This type of contact creates a very small contact region over which force is transmitted, leading to very high contact pressures being generated in the order of GPa . Under these pressures, the contact surfaces deform elastically. In the case of a lubricated contact, a lubricant film forms in between the contacting surfaces in the order of microns (typically $< 2 \mu m$) [36]. Non-conformal contacts are typically found in rolling element bearings, gear contacts and cam follower pairs.

A fundamental characteristic of these contacts is that the approach of the bodies under external load leads to the deformation of both bodies and the emergence of a contact patch. For two cylinders in contact with their axes parallel, a rectangular or line contact is formed along the length of the cylinders with width $2b$ (see Figure 2.3). An elliptical point contact results from contacting bodies that have different radii along both principal axes [37] (see Figure 2.4). In the case of cylindrical elements, such as those in Needle Roller Bearings (NRBs), Cylindrical Roller Bearings (CRBs) and Tapered Roller Bearings (TRBs), the mutual approach of the roller and race forms a line contact. Spherical elements, such as those found in Deep Groove Ball Bearings (DGBBs) and Angular Contact Ball Bearings (ACBBs), generate an elliptical contact at their conjunction with the raceway.

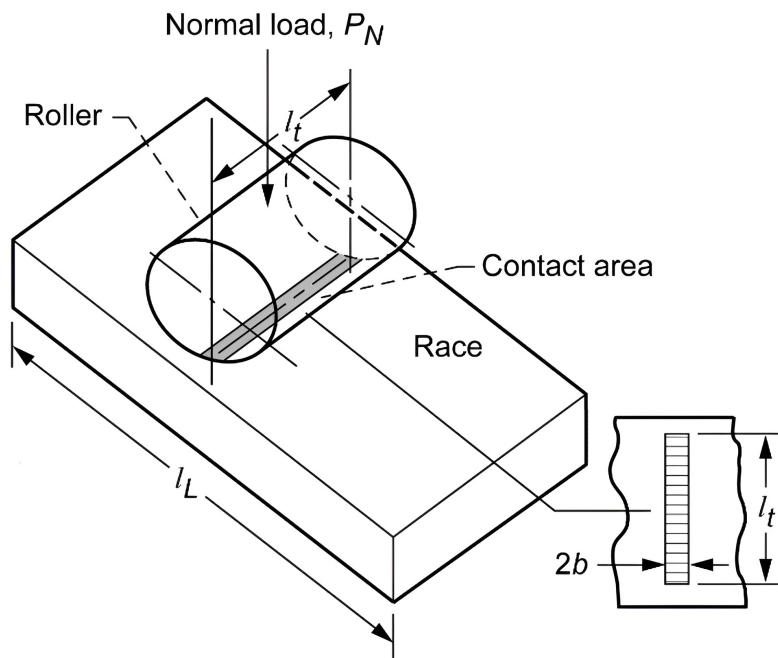


Figure 2.3 Roller-race model for line contact. [38]

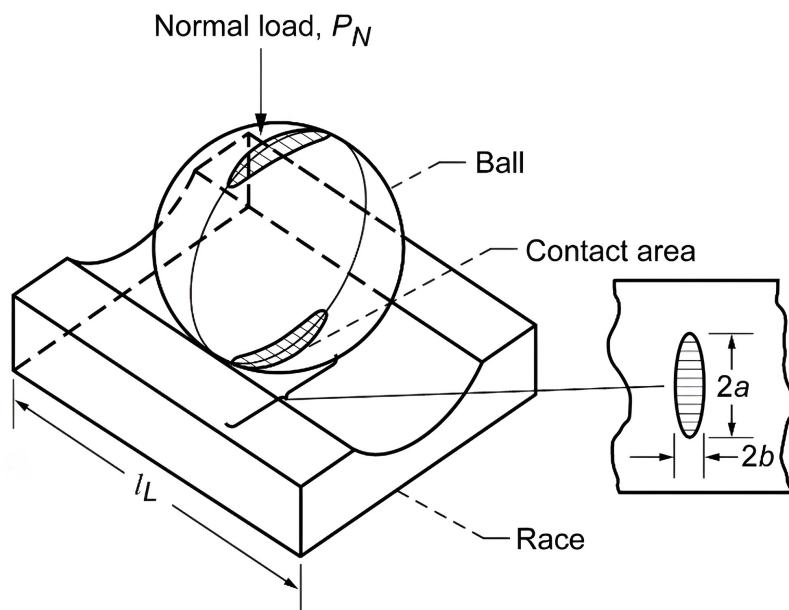


Figure 2.4 Ball-race model for point contact. [38]

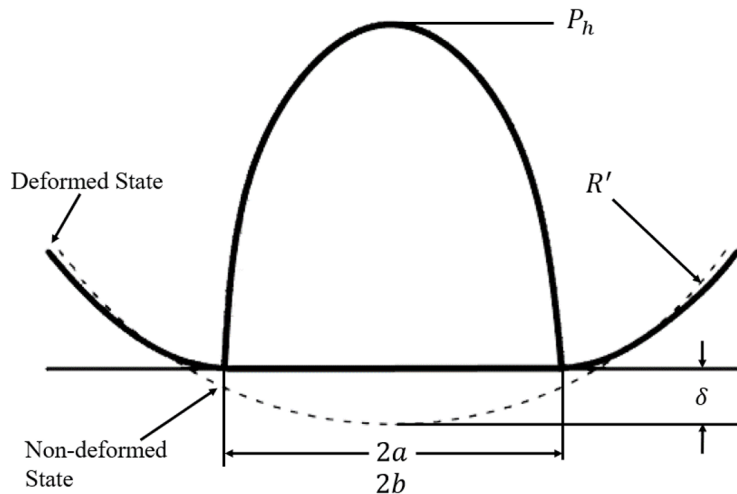


Figure 2.5 Hertzian contact deflection.

Two cylinders with radii R_1 and R_2 contacting in a non-conformal manner can be simplified as a rigid cylinder in contact with an elastic half-space. This cylinder, as represented in Figure 2.3, has a radius known as the reduced radius, R' :

$$\frac{1}{R'} = \frac{1}{R_1} + \frac{1}{R_2} \quad (2.1)$$

The material properties of the two bodies are evaluated in a similar way. The elastic modulus, E and Poisson's ratio, ν , of both bodies are combined to calculate the reduced elastic modulus:

$$\frac{1}{E'} = \frac{1}{2} \left(\frac{1 - \nu_1^2}{E_1} + \frac{1 - \nu_2^2}{E_2} \right) \quad (2.2)$$

According to Hertz's theory of elastostatic solids in contact [39], assuming the contact is frictionless, when load is applied to the cylinder it will experience very small strains. The amount that the cylinder deflects is much smaller than the radius of the cylinder, that is $\delta \ll R'$. The total area of the contact is also much smaller than the radius of the cylinder $a \ll R'$ (exaggerated in 2.5). For example, a cylinder with a radius in order of *mm* will have a contact width of a few tenths of a *mm* and deflection a few tenths of a micron ($\delta < a \ll R'$).

The value of the deflection determines the stiffness of the contact and the displacement of the inner bearing race with respect to the outer. The contact area determines the contact pressures and hence maximum sub-surface stresses. Excessive sub-surface stress could lead to inelastic deformation and subsequent fatigue spalling.

Analytical formulae provide a way of calculating the dimensions of the contact patch, b , and the resultant maximum Hertzian pressure, P_h given a known force, w , material properties and geometry of bodies. For the case of the line contact these are:

$$b = \sqrt{\frac{8wR_{zx}}{\pi E_r}} \quad (2.3)$$

$$P_h = \sqrt{\frac{2w}{\pi b}} \quad (2.4)$$

where w is load per unit length.

2.3.2 Line Contacts

The contact between rolling elements and raceways and the subsequent load and deformation generated at this contact is regarded as one of the most important issues in rolling-element bearing modelling. For a ball bearing, classical Hertzian theory is used to calculate the load-deformation relationship. However, the line contact is more complex.

There exist three methods to determine this relationship for the line contact in roller bearings: the slicing technique, 3D contact method and the alternative slicing technique. The slicing technique [11] divides the roller-race contact region into a finite number of slices, with the total contact forces calculated from the summation of forces of each individual slice. Various formulae have been developed to perform this calculation, all yielding very similar results. A drawback of this method is that the load on each slice does not influence the surrounding slices as they are treated independently. This means that pressure concentrations such as edge stresses on the contact are not captured. The 3D contact method uses the Boussinesq half-space force-displacement relationships and flexibility method of structural analysis. The contact pressure distribution and normal approach between the bodies is found using an iterative scheme, making this a time-consuming method. Kabus et al. [40] addressed this in their 6-DOF quasi-static time-domain bearing model by pre-processing a series of contacts at different centreline approaches and roller tilt angles, then interpolating these results in the actual simulations. This negated the need to solve the iterative scheme at each time step. This allowed for bearing misalignment, roller centrifugal forces, flange contact and roller tilt moments to be analysed.

Teutsch and Sauer [41] improved on the slicing technique with their alternative slicing method. Using a matrix of weighted influence coefficients, the effects of force on the deflection of neighbouring slices was captured. It is not too dissimilar in concept

to the 3D contact method but with improved computation times. de Mul et al. [13] compared the slicing technique with their more complex non-Hertzian model and concluded that the simplicity and accuracy of the slicing method yielded accurate and faster results. Harris and Kotzalas [3] also concluded that the slicing technique, whilst unable to reflect edge stress concentrations, provides a suitably accurate load-displacement result as stresses are only distributed over a small area. For the purpose of load equilibrium, these stresses can be neglected. Misalignment or loading on roller ends is not captured using this technique, therefore for fatigue life estimates this may produce non-conservative results; for this, the approach by Kabus et al. should be used. In general, the slicing technique is the most widely used, owing to its simplicity, speed, and sufficient accuracy.

2.4 Elastohydrodynamic Lubrication

2.4.1 History

Under the EHL regime, both the elastic deformation of the solids in contacts as well as hydrodynamic theory are considered. Elastic bodies in contact for the case of ellipsoidal contacts was first investigated by Hertz in 1881 [39], allowing him to obtain the pressure distribution within an ellipsoidal contact. Separate studies on hydrodynamic lubrication were being performed by Reynolds in 1886 [42], based on a simplified version of the Navier-Stokes equation. It took a further 30 years before the two studies would be combined.

Early EHL studies began in 1916 when the pioneering work by Reynolds was applied to a simplified model of a gear-tooth contact by Martin [43]; replicated as two contacting cylinders. This analysis assumed that the solid bodies were rigid and the lubricant to behave with constant viscosity (ie. a hydrodynamic analysis). The resultant pressures were too high and the film thickness so low (1-10 nm) that coverage of asperities (typical order of 100 nm for machined gear teeth) was not possible. This contradicted experimental findings where machining tracks on high-speed gear tooth flanks were still visible after prolonged usage, which could only be explained by the presence of a sufficient lubricant film.

Between the 1930's and 1950's, significant research was performed to include both the elastic deformation of the surfaces and the effect of pressure on viscosity. Peppler [44] and Meldahl [45] both included the effects of surface deformation for non-conformal contacts, with Gatcombe [46] amongst others investigating viscosity increase due to the high pressure in the contact area. Typical EHL pressures are in the range of 0.5-4 GPa

and the resulting piezo-viscous properties were found to be partially instrumental to forming the film.

Considered the origin of EHL, Grubin's pioneering work in 1949 [47] combined both elastic deformation and viscosity increase under pressure in film thickness calculations for the first time. In this analysis, he assumed that the deformed surface profiles in a highly loaded lubricated contact matched those produced in a classic dry Hertzian contact of the same materials and loading conditions. Reynolds equation could then be solved at the inlet region of the contact and a more accurate determination of the separation of the solids in the central region was found. This led to a film thickness in the predicted range (an order higher than Martin's theory) and a more realistic pressure distribution than previous work. This pioneering study formed the basis for future EHL studies.

The first numerical solution of the line contact problem was presented shortly after by Petrushevich [48] which agreed with Grubin's main conclusions. It contained the three main features of an EHL contact: a nearly parallel film in the contact zone with local constriction at the exit, a Hertzian pressure profile, and secondary local maximum pressure or 'spike' at the outlet (see Figure 2.7). In 1959, Dowson and Higginson [49] presented their numerical solution to the isothermal line contact EHL problem. Their iterative inverse method enabled the evaluation of film thickness and pressure distribution for line contact problems for lightly loaded cases. Throughout the 1960s, the authors investigated the effects of variables such as dimensionless surface velocity, materials parameter and load on EHL solutions. The authors then curve fitted their results and generated an empirical formula for isothermal line contacts [50], which was then improved upon by Dowson [51] and Dowson and Toyoda [52]. The formulae predict the minimum film thickness as a function of the rolling velocity, load and material parameters.

Empirical formulae are widely used today for analytical calculations that do not require the computational intensity of a full numerical solution. They are, however, somewhat limited to the operating parameters used in original simulations and do not offer the capabilities of a full numerical solution, such as the modelling of inlet starvation at high speeds.

2.4.2 Numerical Methods

There are 2 main numerical methods for solving the elastohydrodynamic problem; direct and inverse. Typically, Reynolds equation is solved for pressure based on the lubricant

film thickness. Early studies using this direct method suffered from convergence in highly loaded cases.

Inverse Method Ertel [53] introduced the inverse method for the hydrodynamic problem, which was adopted by Dowson and Higginson [49] for the EHL line contact problem. Here, the film thickness profile is found from a given pressure distribution. Solving the elastic deformation equation provides a second film thickness profile that corresponds to the same pressure distribution. This pressure distribution is then modified manually until the film thickness solutions converge.

This approach has some disadvantages. For low load cases with a non-parallel film shape in the contact region, this method is not suitable since the deviation of the Hertzian starting solution is too large. The film thickness equation is also insensitive to local variations in pressure. Finally, it is only suitable for line contact 1-dimensional cases since the Reynolds equation cannot be integrated for the two-dimensional case. Evans and Snidle [54] overcame the 2-dimensional limitation by using their quasi-static solution where a direct method was applied at the inlet zone and the inverse method in the contact zone. The aim was to overcome the instabilities of the forward iterative method to solve heavily loaded contacts which were limited to 0.5 GPa , whereas common stresses in practice are typically in the order of 1.5 GPa , reaching as high as 4 GPa in some cases. A solution was only found for heavily loaded cases and the approach was limited by the need for an accurate initial estimate for pressure.

Direct Method The direct iterative method is the most common method whereby Reynolds equation is solved to find the pressure with a given film thickness. This pressure distribution is used with the elastic equation to calculate a new film shape. The pressure distribution must also achieve equilibrium with the externally applied load.

Two different direct methods have been used to solve the discretized Reynolds equation. The first is the iterative technique which has been applied to the 1-dimensional line contact problem [55] as well as the two-dimensional point [56] and elliptical [57] contact problem. The Gauss-Seidel scheme was used, solving Reynolds equation for pressure based on film thickness and iterating between the two until convergence was met. Force equilibrium in an outer loop was calculated by integrating pressure across the contact domain and ensuring convergence between the resultant force and the applied external load. The solution comprises of 3 nested loops that must all converge. Under relaxation between successive iteration is applied to aid convergence, however this iterative method does not converge for high loads. Furthermore, the number of iterations

to achieve convergence is large (ie. of the square of the number of computational points used) and thus excessive computation times result.

The second solution method is the Newton-Raphson method. This was first applied by Okumara [58] and later by Houpert and Hamrock [59], where pressures as high as 4.8 GPa were obtained with low CPU times. These low CPU times are a significant advantage of the Newton-Raphson methodology, with a smaller number of iterations resulting in much faster convergence than Gauss-Seidel.

Further numerical development came in the form of the multi-level method, first used by Lubrecht et al. in 1986 [60]. Venner et al. [61] used a multilevel multi-integration for point and line contacts in 1990 to reduce the computational cost of solving the film thickness integral. This allowed more nodes in the computational domain to be used for more complex problems with again much faster solution times. Finer grids could therefore be used, yielding faster results than Newton-Raphson for more complex cases. The solution time was proportional to $n \log(n)$, with n being the total number of nodes in the computational domain. This work was mainly focussed on reducing computational time for the point contact problem, with the authors acknowledging the applicability of the Newton-Raphson numerical scheme for the line contact problem.

2.4.3 Starvation

The assumption of a fully flooded inlet region to the contact is not always valid. Starvation may occur if insufficient lubricant is entrained into the contact; significantly affecting EHL characteristics such as film formation and friction coefficient. This starvation is found to be greater at higher speeds, with higher viscosity lubricants and limited lubricant supply [62]. At high speeds, lubricant replenishment is diminished. For a fully flooded contact, the pressure builds upstream of the contact starting from a pressure gradient close to zero. With insufficient lubricant, the contacting bodies entrain two layers of lubricant, which then merge and form a meniscus at the contact inlet; causing the pressure rise to occur closer to the contact centre with a non-zero pressure gradient and reduced shape of the characteristic pressure distribution [63].

Analytical work on this topic began for the line contact problem by Wolveridge et al. [64] and later developed for the elliptical contact problem by Hamrock and Dowson [65]. In these studies, the inlet distance to the centre of the contact domain is varied as an input parameter. As the inlet distance is extended, the flooded condition at the entrance to the contact becomes greater. At a certain inlet distance, the film thickness in the contact is hardly affected (see Figure 2.6), and this is defined as the threshold between starvation and a fully flooded inlet condition. For the case of shorter inlet distances and

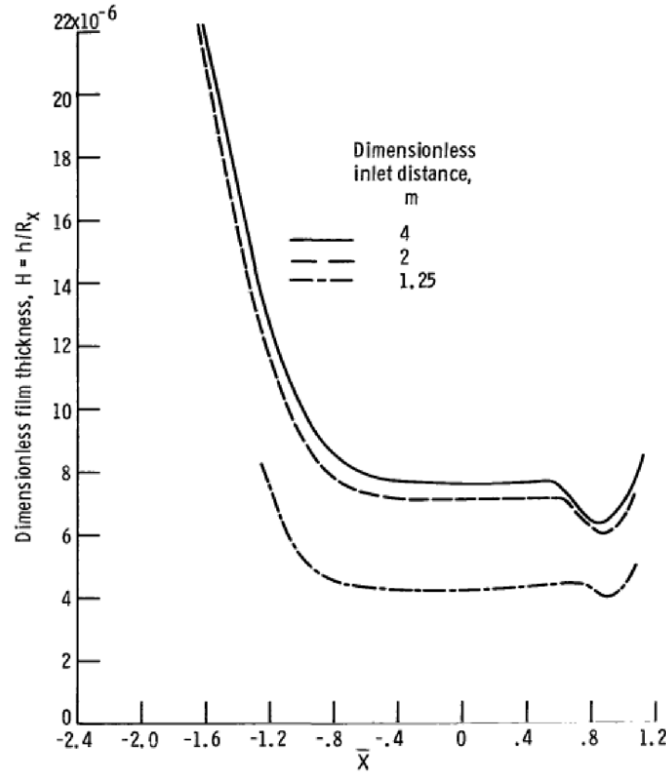


Figure 2.6 Effect of dimensionless inlet distance on film thickness for starvation modelling. [65]

subsequent starved condition, an equation was presented that could adjust the starved film thickness based on the starvation level and flooded film thickness.

2.4.4 Thermal EHL

Heat is generated in an EHL contact in two ways: due to the viscous shearing of the lubricant and the compressive action of the generated pressures [31]. Classic EHL theory is isothermal and considers a Newtonian fluid with no temperature rise from sliding at the conjunction. For the case of pure rolling, this is sufficient to predict film thickness and inlet temperature rise. Rolling element bearings, however, can undergo complex rolling and sliding motions depending on the nature of the loading and contact conditions. The presence of sliding requires a rheological model that considers the viscosity relationship with pressure as well as the use of the energy equation to calculate temperature rise within the lubricant film.

The three-dimensional energy equation has been solved by various authors for the line contact [66], point contact [67],[68] and finite line contact [69]. The generated heat is carried along the direction of entraining motion, in the direction of side leakage from the contact, and through the bounding surfaces of the contact. This can be reduced to

fewer dimensions for the assumption of negligible heat transfer to the contacting bodies in the direction of the film thickness.

It has been found in the case of the point contact under low loads, thermal effects on pressure distribution and film thickness are negligible [70]. However, Kim and Sadeghi [67] concluded that with higher loads, the temperature rise in the film is significant. Under pure rolling conditions, the lubricant film temperature rise was only a moderate 15 °C above ambient and occurred at the inlet zone. As the slide/roll ratio was increased to 0.2, for the same load and speed conditions a temperature rise of 140 °C above ambient resulted at the contact centre, with the dominant mode of heat transfer being shear heating in the contact. The authors also adjusted the ellipticity parameter of the contact [68], with higher ellipticity parameters bringing the elliptical shape of the contact closer to that of a line. In this study, the load was more moderate, and the temperature rise for pure rolling and a slide/roll ratio of 0.2 was 4.5 °C and 16 °C respectively.

Habchi et al. [71] found that even under light loads and moderate speed conditions, thermal effects were still noticeable for Newtonian fluids. For lightly loaded cases, thermal and isothermal results were comparable up to entrainment velocities of 1 m/s but began to diverge slightly above this: in line with experimental findings. Additionally, as the slide/roll ratio is increased above 0.5, both central and minimum films are found to decrease for the thermal model, whereas the isothermal model remains constant. This is due to shear heating reducing lubricant viscosity. The difference was found to be only 0.015 μm between pure rolling and close to pure sliding for a lightly loaded contact.

Shear thinning of the lubricant also occurs at the inlet region to the contact. EHL films are micron level thickness, and assuming a fully flooded inlet, not all of the lubricant will traverse into the contact. Rejected lubricant will then produce some reverse flows which will shear the lubricant, increasing the inlet temperature and hence reduce the viscosity of the fluid [4].

It is therefore clear that a thermal elastohydrodynamic model is necessary for highly loaded conditions with modest slide/roll ratios.

2.4.5 Elastohydrodynamic Pressure and Film Characteristics

If there is relative velocity between two lubricated contacting surfaces, a thin film is formed due to the wedge mechanism and lubricant is entrained into the contact. The pressure profile across the contact deviates from the dry Hertzian parabolic distribution due to the presence of the lubricant.

Figure 2.7 shows the deviation of the film pressure from the dry Hertzian pressure. The main deviation occurs at the outlet of the contact due to the exit conditions. At

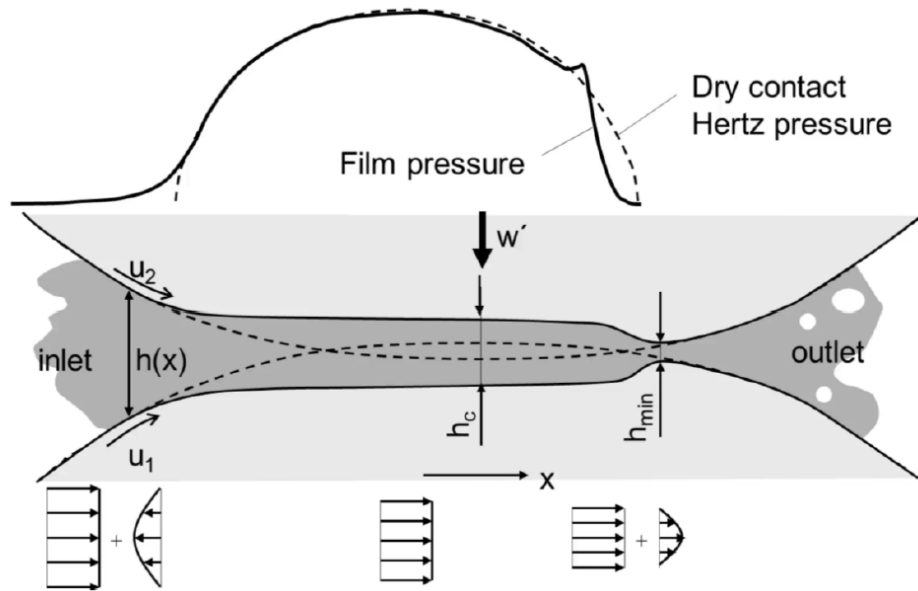


Figure 2.7 EHL film and pressure distribution. [72]

the entry of the contact, the increasing pressure profile acts to oppose the flow of lubricant into the contact due to the entraining motion. At the outlet, the Couette profile and the pressure differential acts in the same direction to force lubricant out of the contact. For mass flow rate of the lubricant across the contact to be conserved, an outlet constriction is formed to reduce the flow area. The pressure spike at the outlet generates this deformation of the surfaces to maintain this flow balance and is a result of the piezo-viscosity of the lubricant. The two laws that must be obeyed are therefore the force equilibrium (the differential of pressure across the contact must equal the applied force), and the flow continuity.

2.4.6 Lubrication Regimes

Lubricated contacts fall into four main regimes, these are:

- **Hydrodynamic:** Contacting surfaces are completely separated by the lubricant film. Load is light, typically several Newtons. The contact surfaces do not experience deformation and resultant pressures are in the region of MPa.
- **Elastohydrodynamic:** Contacting surfaces are completely separated by lubricant film; however, load is medium to heavy. Contact deformation occurs and resultant contact pressures are in the region of GPa.

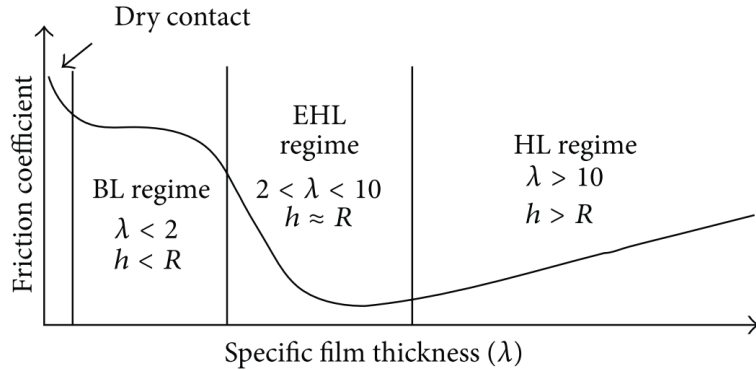


Figure 2.8 Stribeck curve and specific film thickness (λ). [73]

- **Mixed:** An interrupted oil film separates the two surfaces, ie. some asperity interaction occurs. Mixed lubrication can occur under any load and is dependent on the film thickness and asperity height.
- **Boundary:** The lubricant film is negligible, and surfaces directly interact. This is regarded as a dry contact. At medium and high loads, Hertzian contact conditions can be assumed.

The loaded contact region of bearings are typically in the elastohydrodynamic regime of lubrication. The film thickness to asperity roughness height (lambda ratio, λ_s) is large enough that the surface features do not typically influence the lubricant thickness and often a smooth surface is assumed. Under operation, emerging clearances result in unloaded regions of the bearing which can cause the roller-to-race contact to deviate from the elastohydrodynamic lubrication regime towards hydrodynamic regime, resulting in sliding and roller-cage collisions [31]. Hence, the contact may go through different regimes of lubrication throughout its rotation.

Film thickness and surface roughness are related by Stribeck [4] using the specific film thickness:

$$\lambda_s = \frac{h}{\sigma} \quad (2.5)$$

where h is the lubricant film thickness and σ is the roughness height of the asperities on the contact surfaces. Figure 2.8 presents the various lubrication regimes and their associated coefficient of friction. For rougher surfaces, mixed-EHL occurs where contact of surface asperities occurs, increasing friction. The coefficient of friction then reduces as the film increases or asperity height reduces, until the hydrodynamic regime is reached, and the thicker films increase viscous friction.

2.5 Artifical Neural Networks

The most common ML algorithm used in tribological applications are ANNs. The first utilization of these were in the 1990s [74]. Ezugwu et al. implemented and ANN for wear rate and hence life predictions of ceramic cutting tools [75]. Their model had an 80% success rate in predicting the failure mechanism of the tools. Rutherford et al. [76] and Jones et al. [77] developed on this success, focussing on wear rate predictions for coating materials and mechanical systems respectively. Jones et al. were able to achieve 90% wear rate predication accuracy by optimising their ANN architecture using R^2 coefficients as a performance indicator. Similar studies were then conducted in the domain of friction and wear rate of composite materials [78] [79] [80], as well as tools steels [81].

Whilst the friction in the aforementioned studies was modelled under dry conditions, friction in lubricated contacts has also been modelled using ANNs. Bhaumik et al. [82] used ANNs to develop a new lubricant with multiple friction modifiers (FM), considering load, speed and FM concentration as input variables, with the target output being coefficient of friction. A similar methodology was employed to develop biodegradable oils [82], validating both sets of studies using pin-on-disc friction measurements. Traction coefficients under various thermal-elastohydrodynamic operating conditions have also been investigated [83], with the authors noting fast predictions of results with excellent accuracy (lower than 3% error in most cases). Further lubricated studies involving relative viscosity predictions [84] [85] have achieved deviation margins of 1.5% and 0.07% respectively, substantially lower than empirical correlations.

Many further studies have been performed in the field of wear in manufacturing processes [86]. Previous studies had multiple input variables to the ANNs (speed, load, temperature, shear rate). For specific manufacturing processes with particular lubricant-surface combinations, the input data array can be drastically reduced to process-specific variables such as load, speed, and vibration. This approach was taken to investigate flank wear in drilling [87] and surface roughness of machined parts [88]. By reducing the number of input parameters, less training data was required to achieve good fits.

The studies referenced ([75] - [88]) all shared a common approach of utilizing experimental data to train the ANNs. Whilst experimental data benefits from the lack of assumptions in numerical models, there is the limitation of high costs and time required for generating large datasets. Consequently, the training datasets for the ANN were limited to approximately one hundred points [80] [79], or fewer [75] [76], with the largest (216 points) utilised by Cavalieri et al. [81]. Since the training process optimizes the ability of the ANN to interpolate between data points for varying input conditions, a

greater number of training points is advantageous. It was noted by Ezugwu et al. [75] and Zhang et al. [80] that a significant improvement in ANN fit was achieved with a larger training data set. This is an observation shared across several studies and scientific applications [89].

An alternative method of achieving large data sets without the high financial and time cost of experimentation is to use numerical modelling. Wang et al. [90] identified the need for larger training sets in the field of tribology. Their prediction for maximum Hertzian pressure in thermohydrodynamic contacts utilised a training data set that was generated using Reynolds equation. Whilst limited to the accuracy of the numerical model, the ANN benefits from much faster computation time. It crucially also allows for larger data sets to be generated that can cover a much larger range of input data; a requirement for implementation within dynamic models.

The Reynolds boundary value problem has also been solved using Physics Informed Neural Networks (PINN) by Almqvist [91]. The study was not to improve on the numerical accuracy or efficiency of standard finite-difference based methods, rather to present an application of PINN in the field of tribology. Error analysis showed good agreement with the analytical solution, however further work is needed to improve the solving efficiency. Since the ANN is to be implicitly embedded within a dynamic simulation, efficiency is critical. Data driven solutions are therefore preferable. Marian et al. [92] demonstrated for the first time the generation of EHL film thickness data using a Finite Element Method (FEM) to train an ANN. The ANNs could predict locally-resolved film thickness across the contact domain 25-times faster than FE-based EHL simulations.

Although ANNs lack the physical understanding provided by numerical solutions, they offer nearly real-time performance comparable to analytical solutions while benefiting from the accuracy of numerical methods [83].

Echávarri et al. [83] comment on the "black box" nature of ANNs. Results from intermediate calculations are lost, which is often of interest for more in-depth analysis of contact condition; film thickness and pressure distributions and temperature for example.

WHY DECIDED TO USE ANN - Look at study by Marian

It is now known that data-driven solutions, such as machine learning, can greatly enhance the computational efficiency of tribo-dynamic simulations without sacrificing accuracy. In this study, artificial neural networks (ANNs) were trained using numerical solutions constrained by lubrication regimes to ensure the quality of the training data set.

2.6 Closure

A review of the open literature shows that considerable advancements have been and continue to be made in the field of dynamic bearing modelling and tribology. However, there is a paucity of work integrating the two in the context of electrified automotive powertrains. The EHL film is shown to influence contact stiffness and hence dynamic behaviour at high entrainment velocities. With the trend towards high-speed motors in future automotive powertrains, this film growth must be considered. Furthermore, the investigation of this multi-physics interaction is constrained by the substantial computational effort required. The literature shows that ANNs can be successfully used to model tribological phenomena, suggesting that their integration into a dynamic model could provide an efficient and accurate solution.

Chapter 3

Investigating the Effect of Lubrication on the Tribodynamic Behaviour of High-Speed Roller Bearings

3.1 Introduction

A review of the literature revealed that a comprehensive understanding of bearing performance in modern electrified powertrains requires a multi-physics approach comprising dynamics and tribology at high speeds. The working conditions for the tribological contacts between rollers and races are affected by the dynamic behaviour of the bearing. The dynamic behaviour itself is affected by the tribological phenomena at the lubricated conjunctions via introduced frictional dissipation and potential stiffness [93] [94] and damping effects of the lubricant film. Therefore, a coupled tribodynamic methodology must be established for more accurately capturing the system's behaviour.

Bearing orbital motion is conventionally obtained from dynamic models by solving the equations of motion. However, these are computationally intensive and often lack required physics such as system flexibility, flexibility of races and thermal effects [21] [95] [96]. To circumvent the requirement for a complex flexible dynamic model when conducting an initial feasibility review, displacement of the bearing centre and hence contact deflection is captured from experimental test results.

This chapter presents a high-speed experimental test rig which has been instrumented to obtain boundary conditions for tribological models. This work was performed to ascertain which models must be developed in the tribology domain without the need for an extensive dynamic model. The contact load, film thickness, viscous and boundary friction as well as the EHL pressure and film thickness distributions are then obtained

using an implicit tribological model and an explicit 1D numerical EHL model. The requirement for lubricated rather than dry contact models, regimes of lubrication and workflows such as implicit or explicit modelling are investigated.

3.2 Workflow

An experimental test rig is used to obtain the relative displacement between the inner and outer bearing races. Then, using the Hertzian load-deflection relationship and accounting for the lubricant film thickness, load on an individual roller is found at each instantaneous position around the bearing centre through a speed sweep of 0 – 15 000 *rpm*. An implicit analytical tribological model is used which calculates the film thickness at the contact. This loop is iterated to account for the tribodynamic coupling. After the experimentally informed implicit tribodynamic model is solved, load and speed values at specific rotational velocities are used within an explicit numerical EHL model to calculate film thickness and pressure distribution across the contact. The flow diagram in Figure 3.1 illustrates the methodology used. Interactions between each stage will be explained in subsequent sections.

The rollers within a bearing carry an instantaneous share of the overall applied load [97]. Deviation of the supported shaft centre from its nominal geometric centre results in a loaded region of the bearing. In the conjunction between the bearing roller and race, the non-conformal nature of contact generates very high pressures when under load. This causes local surface deformation and an increase in lubricant viscosity, resulting in EHL film formation [98] [47]. Emerging clearances in unloaded regions of the bearing results, which can cause the roller-to-race contact to deviate from the EHL regime towards the hydrodynamic regime, result in sliding and roller-cage collisions [31]. Hence, the contact may go through different regimes of lubrication throughout its rotation [99].

Figure 3.2 shows the cylindrical roller bearing (CRB) in equilibrium position with zero preload or design clearance. Under zero applied radial load, F_0 , the initial deformation, δ_o , and radial clearance, C_0 , between rollers and races are both zero. Due to external force application and system dynamics, an instantaneous radial load, F , will displace the inner bearing race from its equilibrium state (Δx and Δy). By analysing an individual roller at its instantaneous angular position, θ_i , the resultant displacement of the bearing centre can be used to find deflection at the roller-race contact, δ_i . These contact deformations will result in contact forces, W_i , which act to keep the rollers and races in dynamic equilibrium. The above interpretation is valid considering rigid inner and outer races.

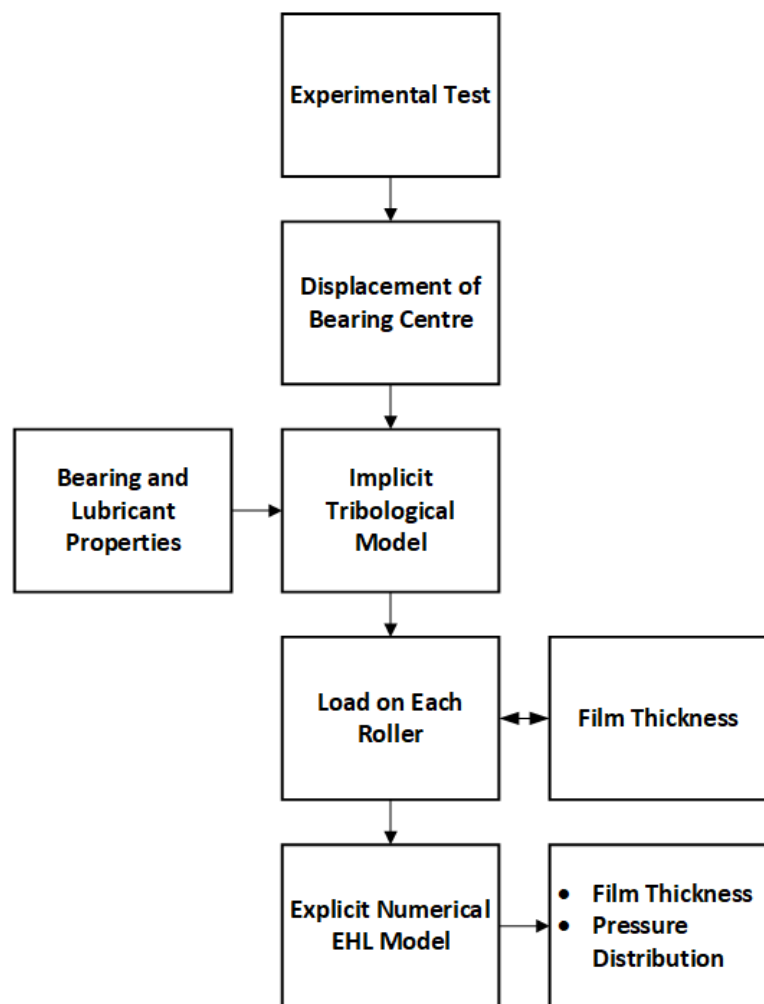


Figure 3.1 Methodology overview.

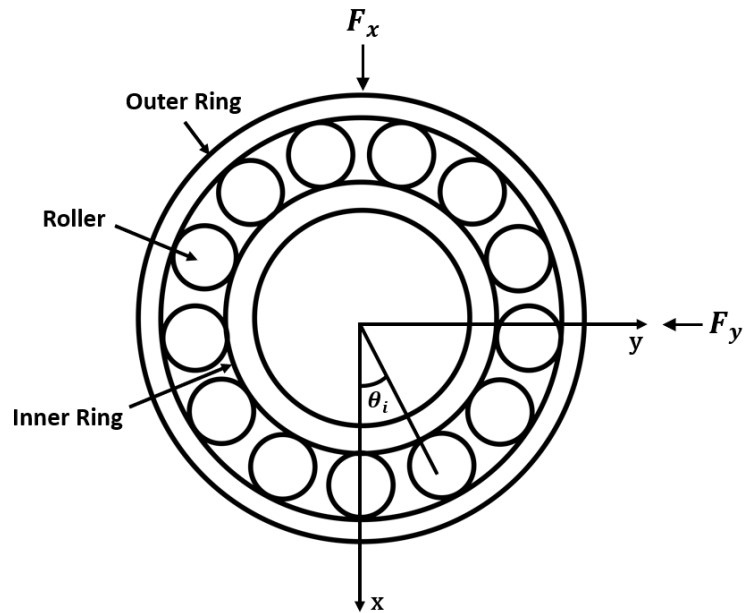


Figure 3.2 Cylindrical roller bearing in equilibrium position.

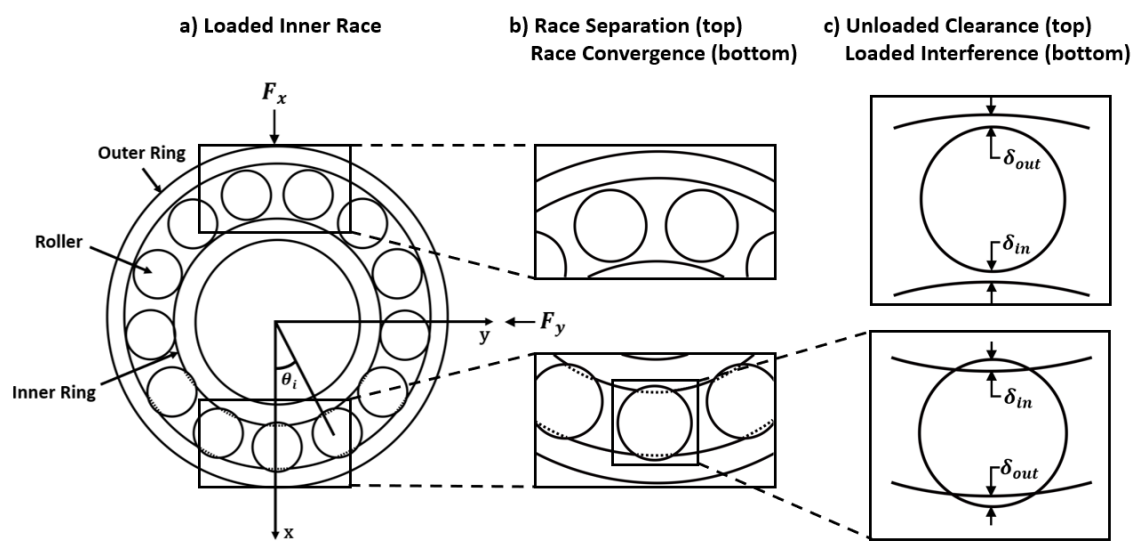


Figure 3.3 Mutual separation and convergence of inner and outer races.

Figure 3.3 presents the case whereby an instantaneous force is applied to the inner race. This causes deflection of the rollers in the loaded region and clearance around the rollers in the unloaded region. The value of the total deflection, δ_i at the inner and outer race corresponds to the component of displacement of the bearing centre at the instantaneous position of that particular roller. In the current study, this value was experimentally measured from the test rig and is used quasi-statically as the boundary condition for the tribological model. It should be noted that in-plane two degrees of freedom motion are analysed in this study which is a valid assumption under dominant radial loading with secondary horizontal motion from the full system dynamics. Misalignment along the length of the rollers is not considered due to the high stiffness of the shaft and bracket, hence a 1D analysis for EHL is sufficient [22].

In the loaded region, the Hertzian load-deflection relationship is used to obtain the resulting instantaneous load on the roller. This value is then used implicitly within an analytical tribological model to calculate contact film thickness for an individual roller as it passes through different angular positions during a speed sweep. An extrapolated film thickness formula is used for this purpose. The calculated film thickness imposes additional deformation at the contact points which itself changes the calculated load. Hence, an iterative approach is required between the force calculation and implicit tribological model. In this part of the workflow, the stiffness and damping of the EHL film is neglected due to its rigid-like stiffness, which is several orders of magnitude higher than the Hertzian contact [100] [101] [102].

For in-depth tribological investigations, the numerical solution of the fluid film is essential. This provides the pressure, film thickness and shear distributions in the contact to study the durability and frictional efficiency of the system. In the current study, the load on the roller and contact kinematics obtained from the implicit bearing model is used explicitly in a 1D elastohydrodynamic model to obtain film thickness and pressure distribution at the contact for specific loading periods through the speed sweep, as is shown in Figure 3.4. This explicit approach significantly improves the computational efficiency of the model and in principle, maintains the accuracy since only the central value of the film is required in the load calculation.

3.2.1 Experimental Test Rig

The displacement of the bearing centre governs the conditions at the contact and was found experimentally using a high-speed bearing test rig, originally reported by Walker et al. [103]. A 5 kW AC synchronous motor, capable of speeds up to 32 000 rpm was coupled to a steel shaft that is supported by two bearing brackets. Radial force was

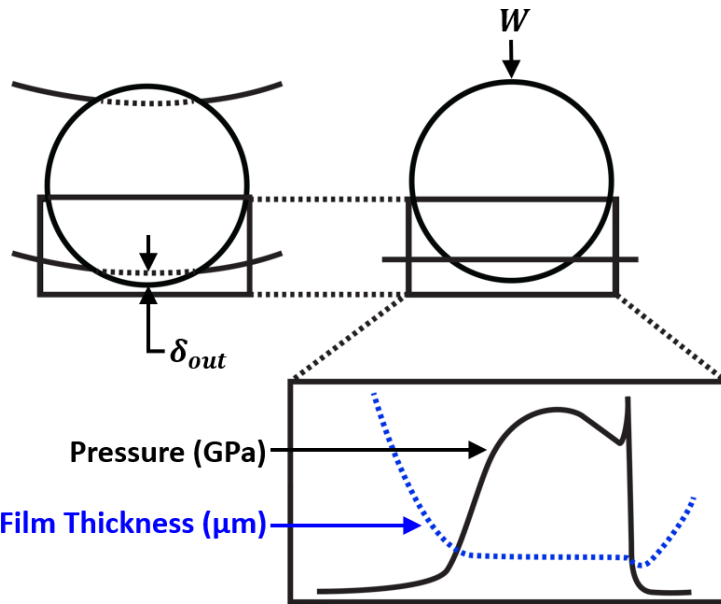


Figure 3.4 EHL film thickness and pressure distribution at contact.

transferred to inner bearing race via the shaft using a hinge/arm mechanism and a load application device on the shaft. Displacement data were obtained from an instrumented bearing bracket. Figure 3.5 shows a schematic of the rig.

The motor control unit was connected to a voltage input, transmitted via an NI cDAQ-9178 USB chassis for optimum resolution of the input voltage. A MATLAB script controlled the voltage ramp over a specified time-period and thus the spindle acceleration. In this study, a transient speed sweep was performed from 0 – 15 000 rpm in a 4 s period, with 750 N of static radial load applied to the shaft. The bearing under test was a single row cylindrical roller bearing, NU 205 ECP, located in an aluminium test bracket that had an extruded bore for instrumentation.

3.2.2 Instrumentation

The outer surface of the bearing bore was instrumented with two Type 4383 single-axis piezo-electric charge accelerometers, with a frequency range of 0.1 – 8.5 kHz and sensitivity of 3.16 pC/ms². These measured acceleration of the bracket's bore, corresponding to the outer race of the bearing (Figure 3.6). Two single beam laser vibrometers measured the displacement of the shaft at the edge of the bearing which corresponds to the displacement of the inner race of the bearing (Figure 3.7). A dual-beam vibrometer was used to measure the rotational speed of the shaft. All laser vibrometers had a frequency range of 0 – 10 kHz and maximum speed of 20 000 rpm.

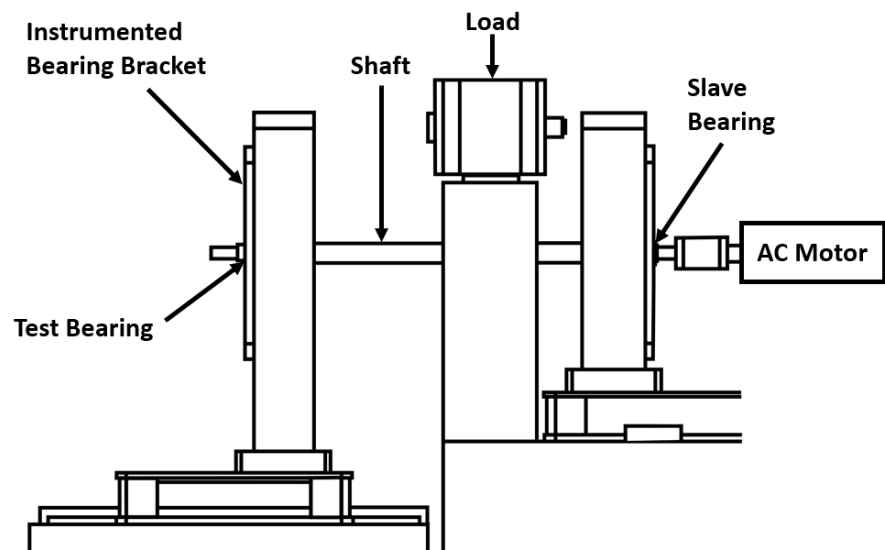


Figure 3.5 Experimental rig schematic.

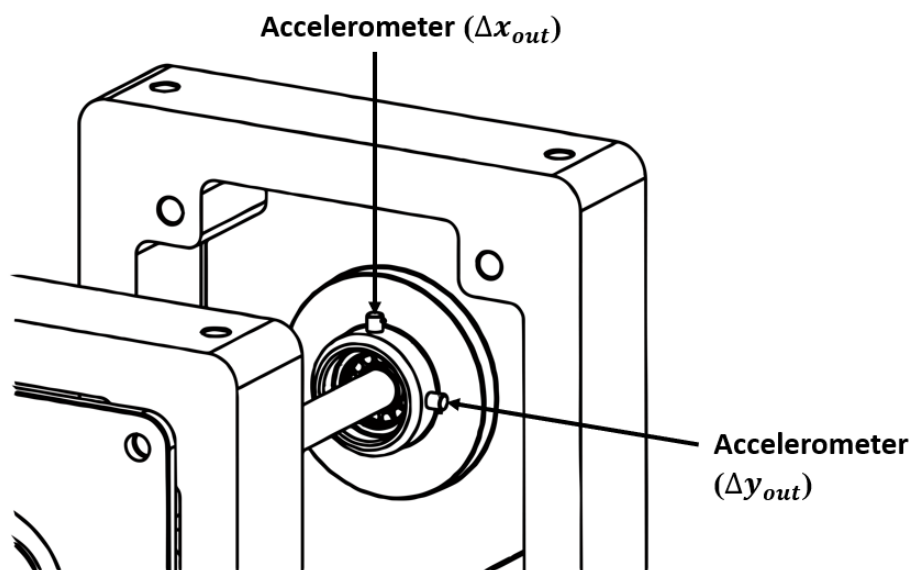


Figure 3.6 Accelerometer locations on test bracket.

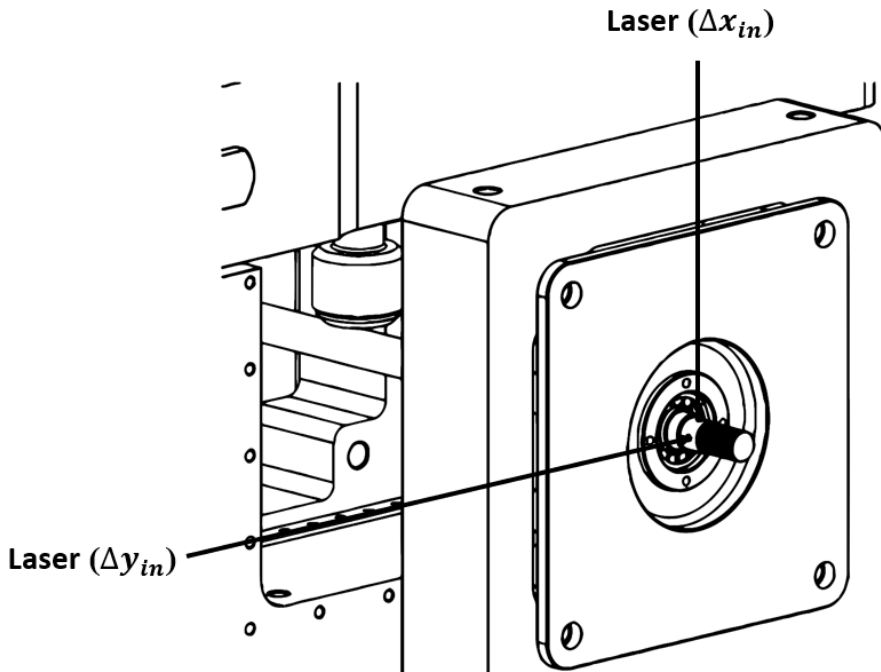


Figure 3.7 Laser vibrometer locations on shaft.

A program in MATLAB controlled the speed of the shaft through a ramped voltage input. Data was simultaneously acquired from the accelerometers and laser vibrometers through synchronised input channels at a sampling rate of 100 kHz. Simultaneous control and data acquisition ensure accurate results between different instrumentation locations.

3.2.3 Signal Processing

The bearing race displacements were obtained from the instrumented bearing using time-domain data from the accelerometers and laser vibrometers. The laser vibrometer directly provided displacement data, whereas the accelerometer data required post-processing of acceleration data. To ascertain the displacement of the bearing bore and thus outer bearing race, the accelerometer results were integrated twice:

$$v_{out}(t) = v_{0,out} + \int_0^t a_{out} dt \quad (3.1)$$

$$x_{out}(t) = x_{0,out} + \int_0^t v_{out} dt \quad (3.2)$$

As this double integration amplifies non-linearities in the original signal, it requires pre-processing [104]. Low frequency drift is removed from the unfiltered time-domain data by applying a linear fit to the data and then removing the trend from it.

To extract the frequency content of the speed ramp, waterfall plots were generated using the accelerometer and laser vibrometer data. Short-time fast-Fourier transform (STFFT) was used, with data windows of six shaft rotations at each 100 rpm increment. The resulting signal was then filtered using a Butterworth bandpass filter for a frequency range of 70 - 10 000 Hz to remove the high amplitude low frequency noise that was inherent to the equipment setup. The filter used 3 dB of passband ripple and 7 dB attenuation in the stopbands, which were set at 35 - 12 500 Hz. The relative displacement of the bearing centre could then be obtained from the relative displacement between the shaft (measured using the single beam laser vibrometer) and bearing bore:

$$\Delta x = \Delta x_{in} - \Delta x_{out} \quad (3.3)$$

$$\Delta y = \Delta y_{in} - \Delta y_{out} \quad (3.4)$$

where Δx_{in} and Δx_{out} correspond to the displacements of the shaft and bearing bore respectively.

3.2.4 Contact Mechanics at the Roller Race Conjunction

The contact between roller and race is modelled as an elastic deformation between an equivalent finite length elastic cylinder and rigid plate. This assumption is realistic under the conditions of an EHL contact. The contact force on an individual roller at each instantaneous position, W_i , is obtained from the Hertzian load-deflection relationship:

$$W_i = k\delta_i^n \quad (3.5)$$

where k is the Hertzian contact stiffness non-linearity between a rolling element and the inner or outer raceway groove. For the case of rolling element bearings, the exponent of localised deflection, n , is equal to 10/9 [8]. The contact deflection of a roller relative to the race, δ_i , is due to the normal dynamic motion (i.e. the local mutual convergence) of the inner and outer bearing races, contribution of lubricant film thickness and any additional clearance or interference fit [31]. This is expressed as:

$$\delta_i = 2(h_{c,i} - C) + x \cos(\theta_i) + y \sin(\theta_i) \quad (3.6)$$

where C is the local radial clearance, and x and y are the displacement components of the inner bearing race from its geometric centre. This normal approach between both races is the sum of the total deformation of the rollers and both races [105], hence:

$$\delta_i = \delta_{i,in} + \delta_{i,out} \quad (3.7)$$

The equilibrium of forces in a system of stiffnesses in series is therefore:

$$W_i = W_{i,out} = W_{i,in} \quad (3.8)$$

To find the individual deflection of each contact due to differences in contact stiffness, the following relationship is used:

$$\delta_{i,in}k_i = \delta_{i,out}k_{out} \quad (3.9)$$

The deflection value at each contact based on the total deflection and relationship between contact stiffness is then found from Equations 3.7 and 3.9 to give:

$$\delta_{i,out} = \frac{\delta_i}{\left(\frac{k_{out}}{k_{in}}\right)^{\frac{1}{n}} + 1} \quad (3.10)$$

The normal stiffness of the inner and outer races differs due to their geometry. To calculate the stiffness at each contact, the following equation is used:

$$\delta = \frac{F}{\pi E_r L} \left[\ln \left(\frac{4\pi E_r R_{zx} L}{F} \right) - 1 \right] \quad (3.11)$$

The deflection for a range of loads is calculated based on the geometry and material properties at the inner and outer race contacts. This non-linear relationship is numerically obtained and then curve fitted and represented by a power function in the form $F = a\delta^b$, with $b = 10/9$ and a representing the contact stiffness. Individual contact stiffness and deflection at the inner and outer race contacts is then found. The overall contact stiffness, $K_{i,total}$, is given by:

$$K_{i,total} = \frac{1}{\left(\frac{1}{K_{i,in}}\right) + \left(\frac{1}{K_{i,out}}\right)} \quad (3.12)$$

where $K_{i,in}$ and $K_{i,out}$ are the stiffnesses of the inner and outer race contacts respectively.

3.2.5 Implicit Tribological Model

A stepwise solution was performed on an individual roller as it passes through each angular position. The roller bearing and bracket tolerances are such that the internal clearance is $0 \mu m$ between roller and race. This means that in an unloaded state, there

is no deflection of elements or raceway. It also means that displacement in positive x-y corresponds to the same total magnitude of deflection of roller and race contact. For each time step, the bearing is first assumed to be in equilibrium position, and film thickness is assumed to be $0\mu m$. The deflection of the bearing is calculated under these conditions and is therefore a function of the relative displacement between inner and outer bearing races. With deflection at the time step calculated, the resultant lubricant regime and subsequent analytical solutions can be performed based on the following three conditions:

1. $\delta = 0$ indicates a film of $0 \mu m$ and no load.
2. $\delta < 0$ indicates complete separation of the roller and race. In this instance, the lubricant is assumed to fill the separation gap, with the film thickness value equalling the magnitude of the separation:

$$h_i = |\delta_i| \quad (3.13)$$

Under this condition, the lubrication is in the hydrodynamic regime. The hydrodynamic lubricant reaction load was derived by Rahnejat [106], and is given by:

$$W_i = \frac{2bu_i\eta_0 R_{zx}}{h_i} \quad (3.14)$$

where b is the half length of the contact, u_i is the speed of lubricant entrainment into the contact, η_0 is the lubricant viscosity, R_{zx} is the reduced radius of the roller and race and h is lubricant film thickness.

3. $\delta > 0$ indicates deflection at the roller-race contact. This means that contact pressure is sufficiently high for the lubrication regime to be elastohydrodynamic. For the elastohydrodynamic regime, an iterative process is performed to solve film thickness. This is due to the contribution of EHL film towards deformation and consequently the load in the contact.

The cylindrical roller and race contacts are modelled by an equivalent rigid roller against a semi-infinite elastic half space of equivalent elastic modulus, E_r . The extrapolated central film thickness for a line contact is therefore obtained [52] from:

$$h_c = R_{zx} \left[3.06G^{*0.56}U^{*0.69}W^{*-0.1} \right] \quad (3.15)$$

where the following dimensionless parameters are used:

$$G^* = \alpha E_r \quad (3.16)$$

$$U^* = \frac{u\eta_0}{R_{zx}E_r} \quad (3.17)$$

$$W^* = \frac{W}{LE_rR_{zx}} \quad (3.18)$$

where R is the reduced radius of the contact, L is the length of the roller and u is the speed of entraining motion into the contact and W is the contact load. Assuming pure rolling, the speed of entraining motion is given by:

$$u_i = \frac{1}{2} (\omega_{c,i} - \omega_{ri,i}) r_{in} \quad (3.19)$$

An iterative process is used to calculate load on the roller based on total deflection including lubricant film (Equation 3.6). At each time step where an EHL film is present, the following convergence criteria must be met before the next time step is calculated:

$$\frac{h_i^n - h_i^{n-1}}{h_i^{n-1}} \leq 0.01 \quad (3.20)$$

3.2.6 Friction Calculations

Frictional power is a crucial factor for characterising their performance. Under modern high-speed conditions, it is important to also understand the frictional behaviour of the system. Roller bearings often operate within the mixed elastohydrodynamic regime of lubrication. Friction is generated by a combination of viscous shear of the lubricant and asperity interactions. Total friction at the mixed-EHL contact is a combination of the boundary friction, f_b , and hydrodynamic or viscous friction, f_v :

$$f = f_v + f_b \quad (3.21)$$

Boundary friction is a function of asperity contact pressure, and is calculated using the Greenwood and Tripp model [107]:

$$f_b = \tau_0 A_a + \zeta W_a \quad (3.22)$$

where τ_0 is the Eyring shear stress of lubricant and ζ is the pressure coefficient for shear strength of asperities, obtained from asperity level friction measurement. Asperity load, W_a , and area occupied by asperities within the apparent contact A_a are obtained as below, assuming a Gaussian distribution of asperity peak counts:

$$W_a = \frac{16\sqrt{2}}{15} \pi (\zeta \kappa \sigma)^2 \sqrt{\frac{\sigma}{\kappa}} E_r A_a F_{5/2}(\lambda) \quad (3.23)$$

and

$$A_a = \pi^2 (\zeta \kappa \sigma)^2 A F_2(\lambda) \quad (3.24)$$

where $\lambda = \frac{h}{\sigma}$ is the Stribeck parameter and $F_{5/2}(\lambda)$ and $F_2(\lambda)$ are statistical functions obtained from numerical integration of the Gaussian distribution of asperities.

Viscous Friction due to shearing of the lubricant film in the EHL contact is found using the below experimentally validated formulae [108]:

$$f_v = \mu W \quad (3.25)$$

where

$$\mu = 0.87 \alpha \tau_0 + 1.74 \frac{\tau_0}{\bar{p}} \ln \left[\frac{1.2}{\tau_0 h} \left(\frac{2K\eta_0}{1+9.6\xi} \right)^{\frac{1}{2}} \right] \quad (3.26)$$

where \bar{p} is the average pressure at the apparent contact, K is the lubricant thermal conductivity and ξ is given by:

$$\xi = \frac{4}{\pi} \frac{K}{h/R_{zx}} \left(\frac{\bar{p}}{E_r R_{zx} K \rho' c' u} \right)^{\frac{1}{2}} \quad (3.27)$$

where K' , ρ' and C' are respectively the thermal conductivity, density, and specific heat capacity of the contacting solid.

To inform the boundary friction model, surface topography data are required. An Alicona InfiniteFocus Variation Microscope with a $\times 10$ objective was used for topography measurements to calculate the roughness parameter, $n\sigma\beta$. This had a vertical resolution of 30 nm and sampling point separation of 176.9 nm in the $y-z$ plane of the roller and 1 nm in x . An area of 530 by 588 μm was captured. Data was processed using Vision65 Map Premium software, where the profile of the radius of the roller was removed. The measured parameters are presented in Table 3.1

Table 3.1 Surface Topography Data

Parameter	Value
Root-mean-square height	$0.197 \mu m$
Density of peaks	$0.00116 1/(\mu m)^2$
Arithmetic mean peak curvature	$0.180 1/\mu m$

3.3 Numerical EHL Model

Whilst the analytical solution used in the implicit tribological model provides central film thickness, the film thickness and pressure distributions can only be obtained explicitly through the full solution of Reynolds equation in conjunction with rheological and elastic field models. In a line contact, where contact dimensions in the side-leakage direction, y_c , are much larger than the direction of entraining motion, x_c , pressure in y_c direction is assumed constant due to the negligible gradient and the contact can be analysed in one dimension. This assumption is valid in the contact apart from small regions near the edge. A simplified 1D version of Reynolds equation can therefore be used.

3.3.1 Reynolds Equation

Reynold's equation [42] is the governing equation of fluid film lubrication theory. For Newtonian fluids it can be derived from the full Navier-Stokes equations making the following assumptions, primarily the neglection of inertial forces and only retaining viscous forces on the lubricant [98]:

1. Body forces are negligible (mass of film is negligible)
2. Pressure is constant through the lubricant film (z-direction) due to thin film (dimensions of the region of pressure are typically 100 times the central film thickness).
3. No slip at boundaries
4. Lubricant flow is laminar (low Reynolds number)
5. Inertia and surface tension forces are negligible compared with viscous forces (working fluid has low mass and low acceleration)
6. Shear stress and velocity gradients are only significant across the lubricant film

7. The lubricant behaves as a Newtonian fluid
8. Lubricant viscosity is constant across the film
9. The lubricant boundary surfaces are parallel or at a small angle with respect to each other

Reynolds equation is a second order, non-linear partial differential equation. It is made up of the pressure induced terms (Poiseuille flow) and the boundary velocity-induced term (Couette flow).

The simplified 1D version of Reynolds equation is given by:

$$\frac{\partial}{\partial x} \left[\frac{\rho h^3}{6\eta} \left(\frac{\partial p}{\partial x} \right) - \rho h u \right] = 2 \frac{\partial(\rho h)}{\partial t} \quad (3.28)$$

To solve Reynolds equation numerically, it must first be discretized and then solved using the finite-difference method. The following procedure explains this discretization.

Due to the steady state nature of the investigations, with the absence of shock loading, the transient squeeze term can be removed:

$$\frac{\partial}{\partial x} \left[\frac{\rho h^3}{6\eta} \left(\frac{\partial p}{\partial x} \right) - \rho h u \right] = 0 \quad (3.29)$$

Due to the many orders of magnitude differences between lubricant film thickness (μm) and pressures (GPa), the numerical solution often becomes unstable. Dimensionless parameters are therefore defined to remove this instability. These are as follows:

$$\begin{aligned} U &= \frac{u}{u_{av}} & \partial x &= a \partial X \\ X &= \frac{x}{a} & \partial \rho &= \rho_0 \partial \bar{\rho} \\ \bar{\rho} &= \frac{\rho}{\rho_0} & \partial \eta &= \eta_0 \partial \bar{\eta} \\ \bar{\eta} &= \frac{\eta}{\eta_0} & \partial h &= \frac{a^2}{R_{zx}} \partial H \\ H &= \frac{h R_x}{a^2} & \partial p &= p_h \partial P \\ P &= \frac{p}{p_h} \\ W^* &= \frac{w}{E_r R_{zx} L} \end{aligned} \quad (3.30)$$

Terms in the simplified Reynolds equation are replaced with dimensionless parameters. Similar terms are then grouped and rearranged to give the final form:

$$\frac{\partial}{\partial X} \left[\frac{\bar{\rho}H^3}{6\bar{\eta}} \left(\frac{\partial P}{\partial X} \right) \right] = \Psi \left[\frac{\partial}{\partial X} \bar{\rho}HU \right] \quad (3.31)$$

where

$$\Psi = \frac{12u_{av}R_{zx}^2\eta_0}{p_h} \quad (3.32)$$

Grouping terms for simplicity

$$M = \frac{\bar{\rho}H^3}{6\bar{\eta}} \quad (3.33)$$

$$Q = \bar{\rho}H \quad (3.34)$$

Making substitutions

$$\frac{\partial}{\partial X} \left[M \left(\frac{\partial P}{\partial X} \right) \right] = \Psi \frac{\partial}{\partial X} [QU] \quad (3.35)$$

$$\left[M \frac{\partial^2 P}{\partial X^2} + \left(\frac{\partial M}{\partial X} \right) \frac{\partial P}{\partial X} \right] = \Psi \left[U \frac{\partial Q}{\partial X} + Q \frac{\partial U}{\partial X} \right] \quad (3.36)$$

The final term is removed, as velocity, U , is independent of x when no stretching of the surfaces occurs. This is then differentiated to give:

$$\frac{\partial M}{\partial X} = \frac{\partial}{\partial X} \left[\frac{\bar{\rho}H^3}{6\bar{\eta}} \right] = \frac{H^2}{2\bar{\eta}} \left[\left(\frac{H}{3} \right) \frac{\partial P}{\partial X} + \bar{\rho} \frac{\partial H}{\partial X} - \left(\frac{\bar{\rho}H}{2\bar{\eta}} \right) \frac{\partial \bar{\eta}}{\partial X} \right] \quad (3.37)$$

and

$$\frac{\partial Q}{\partial X} = \frac{\partial}{\partial X} [\bar{\rho}H] = H \frac{\partial \bar{\rho}}{\partial X} + \bar{\rho} \frac{\partial H}{\partial X} \quad (3.38)$$

Substituting into Equation 3.36 gives the following:

$$\frac{\bar{\rho}H^3}{6\bar{\eta}} \frac{\partial^2 P}{\partial X^2} + \frac{H^2}{2\bar{\eta}} \left[\frac{H}{3} \frac{\partial \bar{\rho}}{\partial X} + \bar{\rho} \frac{\partial H}{\partial X} - \frac{\bar{\rho}H}{2\bar{\eta}} \frac{\partial \bar{\eta}}{\partial X} \right] \frac{\partial P}{\partial X} - \Psi U \left[H \frac{\partial \bar{\rho}}{\partial X} + \bar{\rho} \frac{\partial H}{\partial X} \right] = 0 \quad (3.39)$$

$$\frac{\partial^2 P}{\partial X^2} + \frac{3}{\bar{\rho}H} \left[\frac{H}{3} \frac{\partial \bar{\rho}}{\partial X} + \bar{\rho} \frac{\partial H}{\partial X} - \frac{\bar{\rho}H}{2\bar{\eta}} \frac{\partial \bar{\eta}}{\partial X} \right] \frac{\partial P}{\partial X} - \frac{6\bar{\eta}}{\bar{\rho}H^3} \Psi U \left[H \frac{\partial \bar{\rho}}{\partial X} + \bar{\rho} \frac{\partial H}{\partial X} \right] = 0 \quad (3.40)$$

The final form of the equation is therefore:

$$\frac{\partial^2 P}{\partial X^2} + \left[\frac{1}{\bar{\rho}} \frac{\partial \bar{\rho}}{\partial X} + \frac{3}{H} \frac{\partial H}{\partial X} - \frac{3}{2\bar{\eta}} \frac{\partial \bar{\eta}}{\partial X} \right] \frac{\partial P}{\partial X} - \frac{6\bar{\eta}}{H^2} \left[\frac{1}{\bar{\rho}} \frac{\partial \bar{\rho}}{\partial X} + \frac{1}{H} \frac{\partial H}{\partial X} \right] \Psi U = 0 \quad (3.41)$$

3.3.2 Finite Difference Formulation

For finite difference formulation, the central difference formula based on Taylor series expansion [109] is used. The second derivative of pressure using second order central discretization for the spatial domain is therefore:

$$\frac{\partial^2 P}{\partial X^2} = \frac{P_{i-1} - 2P_i + P_{i+1}}{\Delta X^2} \quad (3.42)$$

and the first derivative is given by:

$$\frac{\partial P}{\partial X} = \frac{P_{i+1} - P_{i-1}}{2\Delta X} \quad (3.43)$$

Replacing terms in the final form of discretized Reynold equation:

$$\frac{P_{i-1} - 2P_i + P_{i+1}}{\Delta X^2} + \left[\frac{1}{\bar{\rho}} \frac{\partial \bar{\rho}}{\partial X} + \frac{3}{H} \frac{\partial H}{\partial X} - \frac{3}{2\bar{\eta}} \frac{\partial \bar{\eta}}{\partial X} \right] \frac{P_{i+1} - P_{i-1}}{2\Delta X} - \frac{6\bar{\eta}}{H^2} \left[\frac{1}{\bar{\rho}} \frac{\partial \bar{\rho}}{\partial X} + \frac{1}{H} \frac{\partial H}{\partial X} \right] \Psi U = 0 \quad (3.44)$$

$$\frac{P_{i-1} + P_{i+1}}{\Delta X^2} + \left[\frac{1}{\bar{\rho}} \frac{\partial \bar{\rho}}{\partial X} + \frac{3}{H} \frac{\partial H}{\partial X} - \frac{3}{2\bar{\eta}} \frac{\partial \bar{\eta}}{\partial X} \right] \frac{P_{i+1} - P_{i-1}}{2\Delta X} - \frac{6\bar{\eta}}{H^2} \left[\frac{1}{\bar{\rho}} \frac{\partial \bar{\rho}}{\partial X} + \frac{1}{H} \frac{\partial H}{\partial X} \right] \Psi U = \frac{2P_i}{\Delta X^2} \quad (3.45)$$

Pressure at each node point can then be represented by:

$$P_i = \frac{\frac{P_{i-1} + P_{i+1}}{\Delta X^2} + \left[\frac{1}{\bar{\rho}} \frac{\partial \bar{\rho}}{\partial X} + \frac{3}{H} \frac{\partial H}{\partial X} - \frac{3}{2\bar{\eta}} \frac{\partial \bar{\eta}}{\partial X} \right] \frac{P_{i+1} - P_{i-1}}{2\Delta X} - \frac{6\bar{\eta}}{H^2} \left[\frac{1}{\bar{\rho}} \frac{\partial \bar{\rho}}{\partial X} + \frac{1}{H} \frac{\partial H}{\partial X} \right] \Psi U}{2 \left(\frac{1}{\Delta X^2} \right)} \quad (3.46)$$

Simplified to

$$P_i = \frac{P_{xx} + P_x - E}{2 \left(\frac{1}{\Delta X^2} \right)} \quad (3.47)$$

where

$$P_{xx} = \frac{P_{i-1} + P_{i+1}}{\Delta X^2} \quad (3.48)$$

$$P_x = \frac{P_{i+1} - P_{i-1}}{2\Delta X} \left[\frac{1}{\bar{\rho}} \frac{\partial \bar{\rho}}{\partial X} + \frac{3}{H} \frac{\partial H}{\partial X} - \frac{3}{2\bar{\eta}} \frac{\partial \bar{\eta}}{\partial X} \right] \quad (3.49)$$

$$E = \frac{6\bar{\eta}}{H^2} \left[\frac{1}{\bar{\rho}} \frac{\partial \bar{\rho}}{\partial X} + \frac{1}{H} \frac{\partial H}{\partial X} \right] \Psi U \quad (3.50)$$

3.3.3 Effect of Pressure on Lubricant Viscosity

EHL temperatures are typically in the region of 0.5-4 GPa. The resultant behaviour of the viscosity at these pressures is instrumental in forming the EHL film and must be accounted for. The Barus law [110] determines viscosity increase with pressure assuming constant ambient temperature:

$$\eta = \eta_0 \exp(\alpha p) \quad (3.51)$$

where η is the lubricant viscosity at gauge pressure, p , η_0 is the viscosity at $p = 0$, and α is the pressure-viscosity coefficient (m^2/N) and is specific to the lubricant. This relationship does not account for the change in α with temperature and pressure [111], becoming inaccurate above 0.5 GPa.

A more comprehensive relationship which simultaneously includes the effects of temperature and pressure was one proposed by Roelands [112] and developed by Houptert [113]. Roelands law is therefore accurate at higher contact pressures:

$$\eta = \eta_0 \exp(\alpha^* p) \quad (3.52)$$

The Roelands pressure-viscosity coefficient, α^* , is a function of both p and θ , with θ_0 being the reference or ambient temperature, for example at the inlet:

$$\alpha^* p = [\ln(\eta_0 + 9.67)] \left\{ \left(\frac{\theta - 138}{\theta_0 - 138} \right)^{-S_0} \left[\left(1 + \frac{p}{p_0} \right)^{Z_0} - 1 \right] \right\} \quad (3.53)$$

where

$$z_0 = \frac{\alpha}{5.1 \times 10^{-9} [\ln(\eta_0) + 9.67]} \quad (3.54)$$

and

$$S_0 = \frac{\beta (\theta_0 - 138)}{\ln(\eta_0) + 9.67} \quad (3.55)$$

The oil constants Z_0 and S_0 are independent of both pressure and temperature, and Z_0 can be typically taken as 0.68 for computational purposes.

3.3.4 Effect of Pressure on Lubricant Density

For accurate film EHL film shape calculations, the effect that pressure has on the lubricant density must be considered. The most common equation for this is the widely used Dowson and Higginson model [114]:

$$\rho = \rho_0 \left(1 + \frac{0.6 \times 10^{-9} p}{1 + 1.7 \times 10^{-9} p} \right) \quad (3.56)$$

where ρ_0 is the lubricant atmospheric pressure. Further modifications can be made to account for the effects of temperature:

$$\rho = \rho_0 \left(1 + \frac{0.6 \times 10^{-9} p}{1 + 1.7 \times 10^{-9} p} \right) [1 - 0.65 \times 10^{-3} (\theta - \theta_0)] \quad (3.57)$$

3.3.5 Effect of Temperature on Viscosity

Most EHL work assumes constant temperature of the contact and that viscosity and density are dependent on pressure only. Standard experiments have been performed to assess effect of temperature on viscosity. Results have previously been curve fit by Crouch and Cameron [115], with the most simple fit due to Reynolds:

$$\eta = \eta_s \exp(-\beta \Delta \theta) \quad (3.58)$$

where η_s is the viscosity of the lubricant at temperature θ_s , η is the viscosity at representative temperature, θ , and $\Delta \theta$ represents the temperature difference between the two. β is the thermoviscous constant and is lubricant specific. This relationship is only valid for small temperature rises of the lubricant. A more accurate and widely used equation is the expression from Vogel:

$$\eta = K \exp \left(\frac{b}{\theta + c} \right) \quad (3.59)$$

with the three constants dependant on the lubricant, obtained from knowing three pairs of values for θ and η .

3.3.6 1D EHL Solution Methodology

The methodology for the 1D EHL solution used within this thesis is as follows.

Reynolds equation is used to calculate contact pressures. Assuming a thin film of Newtonian lubricant in a line contact, the following form is used and discretized as described in Section 3.3.2:

$$\frac{\partial}{\partial X} \left[\frac{\bar{\rho} H^3}{6\bar{\eta}} \left(\frac{\partial P}{\partial X} \right) \right] = \Psi \left[\frac{\partial}{\partial X} \bar{\rho} H U \right] \quad (3.60)$$

where X is the direction of entraining motion into the contact. Squeeze film motion is neglected for this analysis. The pressure-density relationship in the compressible model is modelled using Dowson-Higginson [114] (3.56). Roelands equation [112] (3.52) is used for the pressure-viscosity relationship.

Pressure distribution is obtained from the variations in film thickness at the contact, which is defined as below:

$$h = h_0 + \frac{x^2}{2R_{zx}} - \frac{2}{\pi E_r} \int_{x_{c,in}}^{x_{c,out}} p \ln(x-x')^2 dx' \quad (3.61)$$

where h_0 is the central film thickness, the second term represents an idealised film thickness parabola, with the final term representing the localised contact deflection. Central film thickness is first estimated using [52]:

$$h_0 = R_{zx} 3.06 G^{*0.56} U^{*0.69} W^{*-0.1} \quad (3.62)$$

$$G^* = \alpha E_r \quad (3.63)$$

$$U^* = \frac{u \eta_0}{R_{zx} E_r} \quad (3.64)$$

$$W^* = \frac{w}{L E_r R_{zx}} \quad (3.65)$$

Below, the method of solution for the numerical EHL model is provided:

1. Input the load value obtained from the implicit tribological model for an instantaneous position as well as contact kinematics from experimental conditions.
2. An initial estimation of lubricant film thickness, h_0 is made.
3. Inlet and outlet distances are set to $-4.5a$ to $1.5a$ based on the contact half width calculation. This sets up the computational domain, and assumes fully flooded inlet conditions [65].
4. Pressure distribution and film thickness are obtained through simultaneous solutions of equations 3.60 to 3.62 using the dimensionless parameters defined in 3.30. The Newton-Raphson iterative scheme is used for speed and robustness

of convergence [58]. Pressure convergence criterion is required for the iterative solution:

$$\text{Err}_{\text{pressure}} = \frac{\sum_{i=1}^n |p_{\text{new}} - p_{\text{old}}|}{\sum_{i=1}^n p_{\text{old}}} \leq \varepsilon_p \quad (3.66)$$

where $\varepsilon_p = 1 \times 10^{-5}$.

Under-relaxation is applied between successive iterations where the criterion is not met:

$$p_{\text{new}} = (1 - \gamma)p_{\text{old}} + \gamma p_{\text{new}} \quad (3.67)$$

where the under-relaxation factor is typically $0.01 \leq \gamma \leq 0.8$

5. Hydrodynamic reaction load is calculated using the integration of pressure over the computational domain:

$$W_h = L \int pdx \quad (3.68)$$

The total reaction from the hydrodynamic load should be equal to the total load share on the roller, W_i , obtained from the explicit tribological model. The following convergence criterion is applied:

$$\frac{|W_i - W_h|}{W_i} \leq \varepsilon_W \quad (3.69)$$

where $\varepsilon_W = 0.001$

3.3.7 Numerical EHL Model Validation

Conjunction level validation of the numerical method for solving the EHL film thickness and pressure distributions was performed using the work of Masjedi and Khonsari [116]. These were validated against their smooth surface plots with no asperity pressure contribution. The dimensionless input parameters were $W^* = 1 \times 10^{-4}$, $U^* = 1 \times 10^{-11}$ and $G^* = 4500$. The results shown in Figure 3.8 and Figure 3.9 show a good agreement between the model used in the study and the work of Masjedi and Khonsari for the dimensionless pressure, P , and dimensionless film thickness, H , respectively.

3.3.8 Experimental Result Verification

The experimental results obtained from the presented rig were verified against analytically calculated frequency contents. This was to ensure the correct post processing of

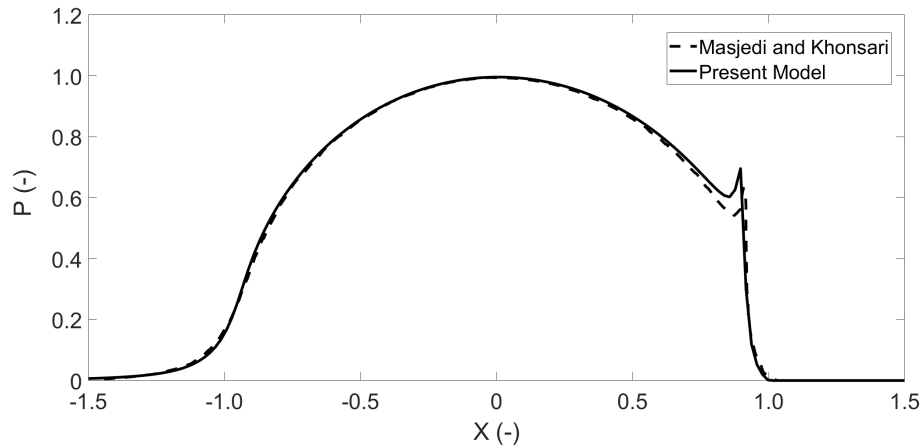


Figure 3.8 Validation of dimensionless pressure distribution, present model (solid),
Masjedi and Khonsari (dashed).

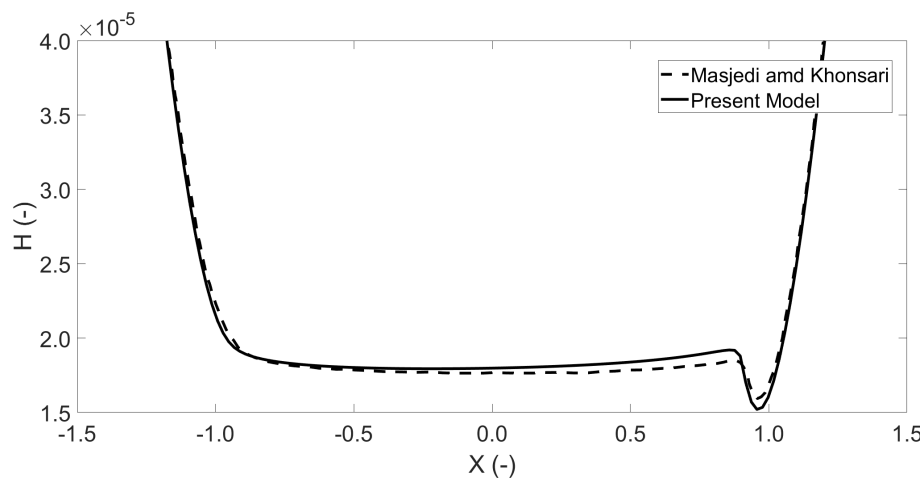


Figure 3.9 Validation of dimensionless film thickness distribution, present model (solid),
Masjedi and Khonsari (dashed).

Table 3.2 Bearing Specification

Parameter	Value
Inner race bore	25 mm
Inner race diameter	31.5 mm
Outer race diameter	46.5 mm
Roller diameter	7.5 mm
Roller length	9 mm
Number of rollers	12
External load	750 N
Radial interference	0 μm

data for the input to numerical models. The bearing and lubricant data properties are given in Table 3.2 and Table 3.3 respectively which were also used in simulations.

Primary frequencies in the system due to the interaction of the rolling elements, races and the shaft could then be verified. These frequencies were calculated analytically, with f_{bpi} and f_{bpo} representing the ball pass frequencies of the inner and outer race respectively and f_{shaft} being the rotational frequency of the shaft:

$$f_{bpi} = \frac{\omega_s}{2\pi} \frac{N}{2} \left(1 - \frac{D_r}{D_p} \right) \quad (3.70)$$

$$f_{bpo} = \frac{\omega_s}{2\pi} \frac{N}{2} \left(1 + \frac{D_r}{D_p} \right) \quad (3.71)$$

$$f_{shaft} = \frac{\omega_s}{2\pi} \quad (3.72)$$

At 14 000 rpm, the theoretical inner and outer race frequencies are calculated to be 1669 Hz and 1131 Hz respectively, with the experimental results being 1611 Hz and 1131 Hz. The first order shaft rotational frequency from the experiment was 232 Hz compared to theoretical calculation of 233 Hz. The above frequencies can be seen clearly in Figure 7, which shows the bearing bore displacement spectra, and Figure 8 which represents the shaft displacement spectra. The verification frequencies are identical in both, confirming that the bearing motion is accurately measured by the experimental methodology. It is observed that at certain speeds, the ball pass frequency of the outer race has a larger contribution than the inner race. This is particularly highlighted at

Table 3.3 Lubricant and Material Properties

Parameter	Value
Pressure viscosity coefficient (α)	$2.1 \times 10^{-8} \text{ Pa}^{-1}$
Atmospheric lubricant dynamic viscosity	0.08 Pa.s
Lubricant inlet density (ρ_0)	$833.8 \text{ kg} \cdot \text{m}^{-3}$
Eyring stress (τ_0)	2 MPa
Shear strength of asperities (ζ)	0.3
Thermal conductivity of fluid	$1600 \text{ W} \cdot \text{m}^{-1} \cdot \text{K}^{-1}$
Modulus of elasticity of contacting solids	210 GPa
Poisson's ratio of contacting solids	0.3
Density of contacting solids	$7850 \text{ kg} \cdot \text{m}^{-3}$
Thermal conductivity of contacting solids	$46 \text{ W} \cdot \text{m}^{-1} \cdot \text{K}^{-1}$
Specific heat capacity of contacting solids	$470 \text{ J} \cdot \text{kg}^{-1} \cdot \text{K}^{-1}$

12 000 - 14 000 *rpm*. These regional effects are contributed by modal behaviour of the bracket and the bed. The critical speed of the unloaded shaft, where lateral bending frequency of the shaft is equal to the rotation frequency [117], occurs at 12 660 *rpm* and 211 *Hz*.

3.4 Results and Discussion

This section presents the results of the numerical tribological models. The kinematic data from the experimental test rig are used as the boundary conditions to the implicit and explicit models.

3.4.1 Film Thickness and Load Across Speed Sweep

The variation in EHL film thickness and roller contact load across the speed sweep from 0 - 15 000 *rpm* at the outer race contact are shown in Figure 3.12. Only the EHL regions are shown, where loads are significant enough to cause contact deformation. The upper limit of the film is where the roller and races diverge and approach the hydrodynamic regime where the film is hence governed by the entraining motion of lubricant into the

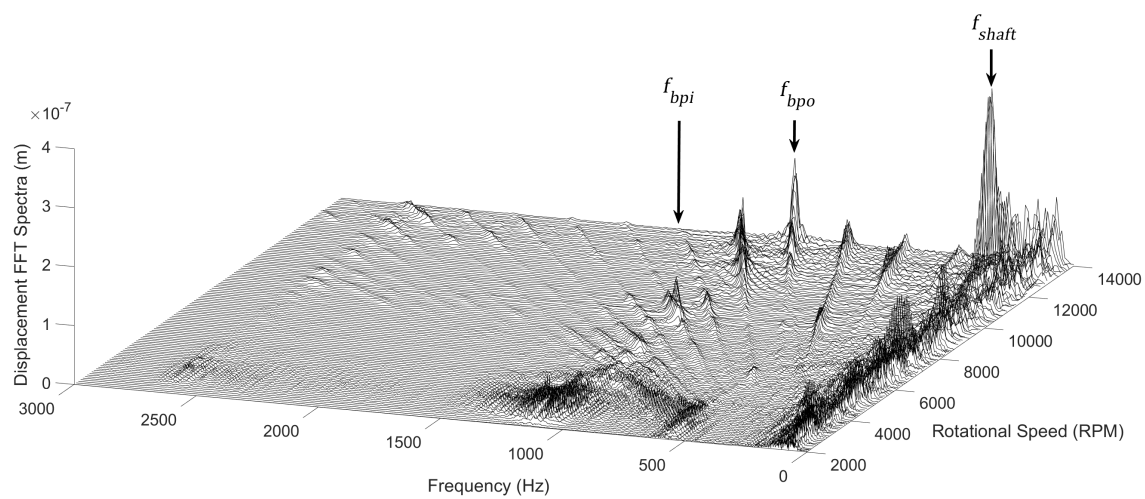


Figure 3.10 Bearing bore displacement frequency spectra.

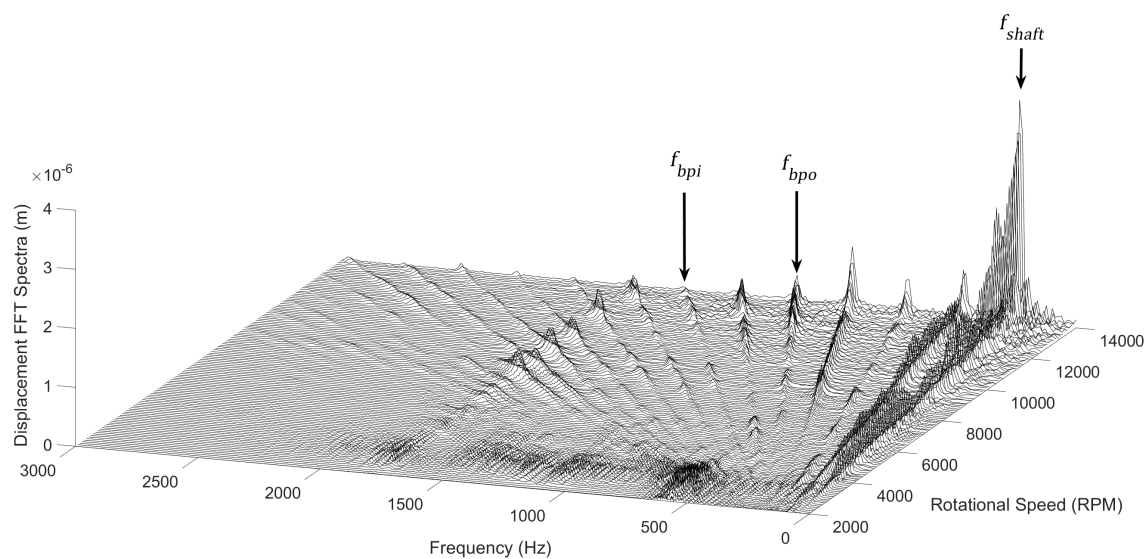


Figure 3.11 Shaft displacement frequency spectra.

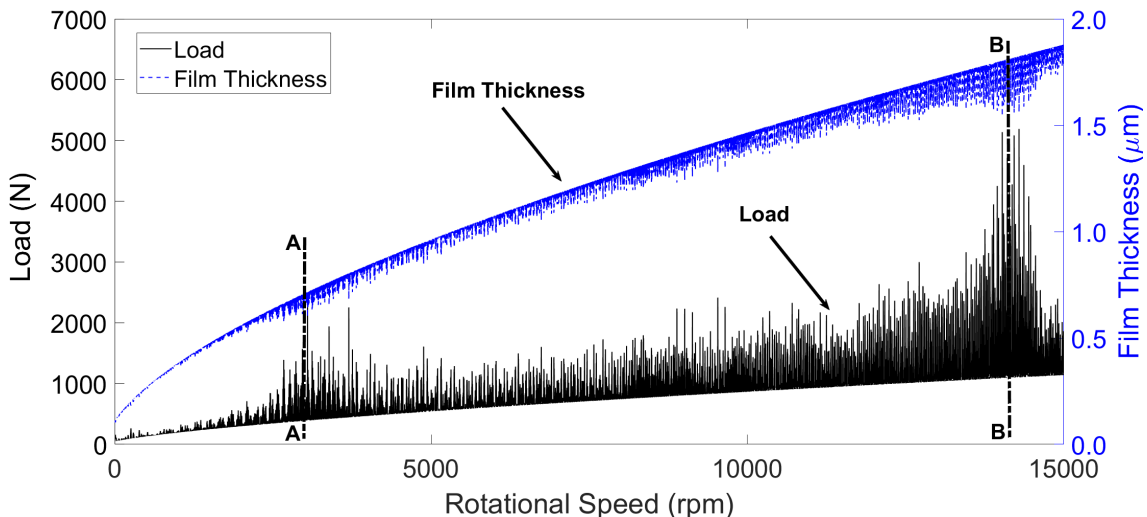


Figure 3.12 Contact load and film thickness - Outer race.

contact. The lubricant film, as seen from the film thickness equation, is more affected by the speed of entraining motion rather than the load. This explains the increasing film thickness values in Figure 3.12 despite increasing load. The film thickness is increased from 0.1 to 1.9 μm across the speed sweep, revealing a significant increase that can affect the tribodynamic behaviour of the bearing, as explained in following sections. From the tribological model, it is possible to observe the transition between mixed-EHL to the purely hydrodynamic regime as the roller passes in and out of the loaded region of the bearing. Full system and rotor dynamics also contribute to the total load on the roller, with periods of resonance at 3 000 rpm and 14 000 rpm , marked as *A* and *B* respectively in Figure 3.12.

Figure 3.13 presents an interval of the speed sweep where the effect of the EHL load on reducing the film thickness under oscillating conditions can be observed and the hydrodynamic film growth as the roller is unloaded. It is possible to see the effect of the resonant frequency at 1765 Hz superimposed on the lower fundamental train frequency within the loaded region as the inner and outer rings converge and diverge. The results in Figure 3.13 confirm the significant effect of dynamic behaviour as well as multi-regime nature of the lubrication due to dynamic effects.

3.4.2 Friction

Focussing on data from the EHL regime, boundary and viscous friction through the speed sweep can be analysed. Figure 3.14 shows the boundary and viscous friction across the speed sweep. As the film thickness increases with speed, the separation of the contacting surfaces increases, reducing the boundary interaction of asperities. The

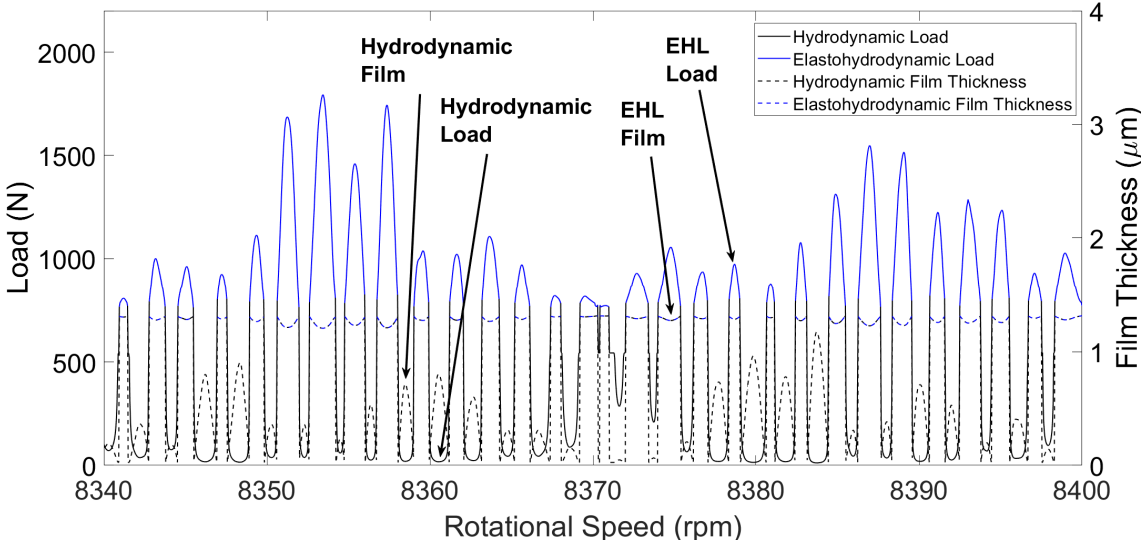


Figure 3.13 Film and load - EHL to hydrodynamic regime.

resonant period at 14 000 *rpm* reduces the film height, increasing the likelihood of asperity interaction in that region and hence boundary friction and potential for wear. In general, the boundary friction reduces towards higher rotational and entrainment velocities. This does not, however, account for lubricant inlet starvation at high speeds or roller sliding. Viscous friction increases with higher speed and hence the shear as expected. Although the film thickness also increases at higher speeds which may reduce the amount of shear, the effect of increasing speed is more dominant. The peak values occurring again at a resonance speed of 14 000 *rpm* where the highest loads and smallest film occurs.

3.4.3 EHL Regimes

As has been demonstrated in the results analysis, the contact conditions deviate from the elastohydrodynamic regime of lubrication into the hydrodynamic regime throughout the roller orbital motion. These conditions can be verified by presenting the results on the Greenwood chart for fluid regimes of lubrication. The charts display the physical effects instrumental to EHL formation under isothermal conditions: viscosity rise due to pressure and elastic deformation of the surface. These two effects are quantified by two dimensionless parameters, G_e and G_v , as defined below [98]:

$$G_e = \frac{W^*}{U^{*1/2}} \quad (3.73)$$

$$G_v = \frac{W^{*3/2} G^*}{U^{*1/2}} \quad (3.74)$$

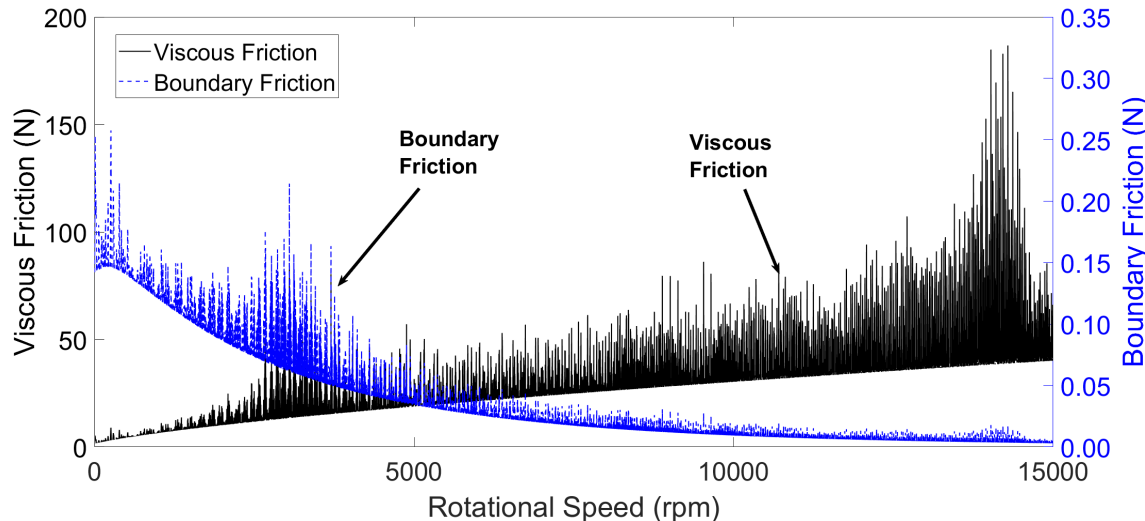


Figure 3.14 Viscous and boundary friction at the outer race contact.

Four regions exist and the boundaries of these regions are defined by the geometry of contacting bodies, material, and lubricant properties. As is shown in Figure 3.15, the outer roller-race contact conditions move between the viscous elastic and iso-viscous rigid regimes, representing EHL and hydrodynamic respectively. The viscous elastic regime signifies the EHL regime of lubrication where contact pressures are such that elastic deformation of the surfaces and viscosity rise due to pressure increase is significant. The iso-viscous rigid regime occurs when the magnitude of elastic deformation is insignificant, and the contact pressures are low enough that viscosity rise is negligible, i.e. hydrodynamic lubrication [118]. The boundary between the two also corresponds well with the distinction being made between hydrodynamic and EHL in this methodology, presented by the black and blue regions of the plot.

3.4.4 Dry vs Lubricated Tribodynamic Model

Previously presented results confirmed the significance of considering tribodynamic coupling on the tribological predictions. The aim of this section is to assess the significance of this coupling on dynamics via affecting contact load and stiffness values. The surface deformation at the EHL contact is further exacerbated by the presence of the lubricant film. Since the contact load and contact stiffness are governed by this deformation, neglecting the film leads to an underestimation of the total load at the roller-race contact. At higher speeds, such as those present in modern electrified powertrains, the growth of the lubricant film due to the increased entraining motion into the conjunction cannot be neglected – as is shown in Figure 3.12 with a film growth from 0.1 to $1.9 \mu\text{m}$. The implicit tribological model was run for two cases, including and negating lubricant film

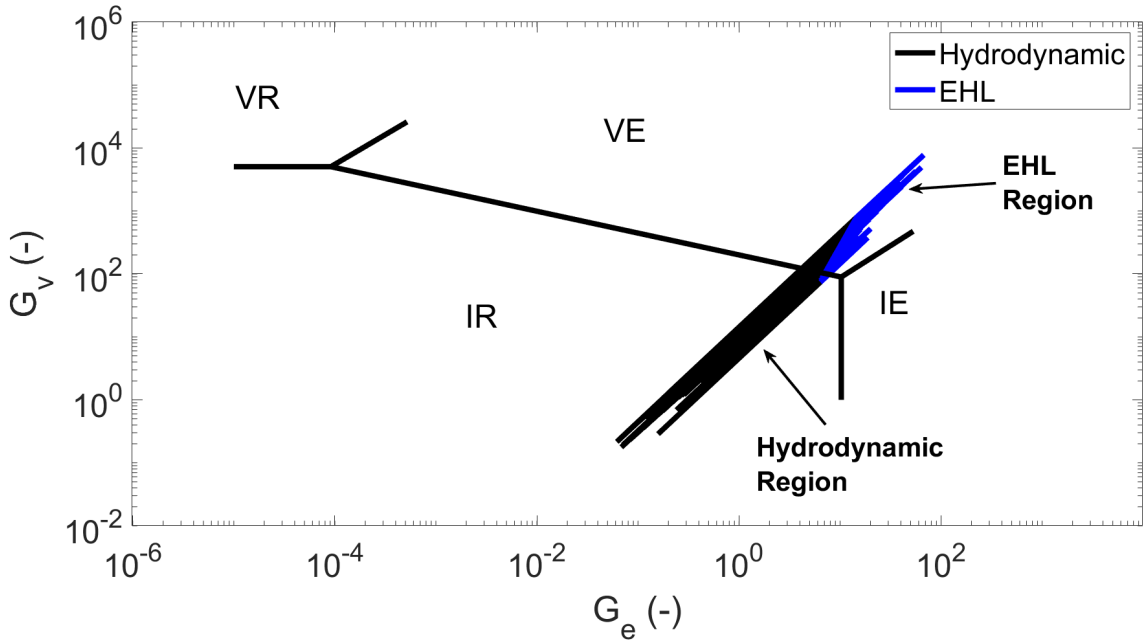


Figure 3.15 EHL and hydrodynamic conditions during roller operation. Key: IR = Iso-viscous Rigid, VR = Viscous Rigid, VE = Viscous Elastic, IE = Iso-viscous Elastic.

thickness in the deformation obtained from Equation 3.6. The difference in magnitude at each time step is computed, and the increase in load magnitude between a dry and lubricated model is calculated. For EHL loads, the magnitude of the load difference through the speed sweep is plotted in Figure 3.16.

There is an increasing contact load difference across the speed sweep, with fluctuations arising from the dynamics of the system. It is clear that neglecting lubricant film thickness leads to significant underestimation of the contact load, hence inaccurate dynamics as well as tribological calculations. This effect gains more significance at higher speeds which highlights the necessity of considering tribodynamic coupling for high-speed conditions in electrified powertrains. To fully understand the requirement for a lubricated bearing model, the percentage difference between both cases is presented at three different rotational speed snapshots of 3 050 *rpm*, 14 135 *rpm*, and 14 855 *rpm* in Figure 3.17. At low speeds and relatively low dynamic load, the addition of the film contributes to a 14.8% greater load prediction than a dry model, showing that the film inclusion has a significant contribution even at low rotational speeds. At shaft speeds of 14 135 *rpm*, the first order resonance in the system, as shown in the frequency plots, creates high dynamic loading. At peak load, the growth of the film is still present, however, the high contact deformation is close to the magnitude of the film growth, hence the difference between dry and lubricated model reaches 25.1%. As the system passes through this resonant region and the overall dynamic load is reduced, the percentage

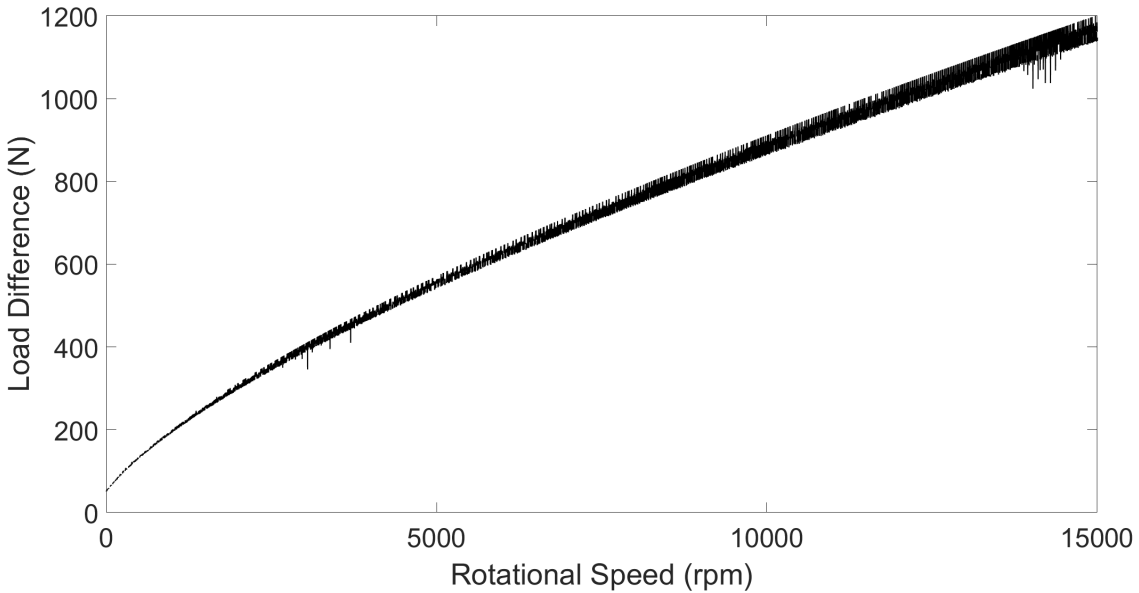


Figure 3.16 Contact load difference between dry and lubricated model.

load difference reaches values as high as 149% as the effect of the film growth at high speeds exceeds that of the surface deformation.

At high speeds in periods of resonance, the magnitude of the bearing load dominates, and the effect of the increasing film thickness with speed diminishes in regions of resonance. The percentage difference between the dry and lubricated model is lower as the external force and corresponding surface deformation prevails the effect of the film. However, at high speeds outside of this period of resonance, the film thickness is of the same order as the deformation and the percentage difference between the two models is much greater.

3.4.5 Numerical EHL Results

Full numerical simulation is required to obtain detailed pressure and film thickness distributions. These distributions reveal the realistic pressure and film values at the contact for in depth durability, efficiency and thermal analysis. At 8 350 rpm, focussing on one roller orbit, the selected points for EHL numerical analysis are shown in Figure 3.18. These load values are found from the implicit tribological model when the roller enters the loaded region of the bearing. The corresponding points on the bearing circumference are also shown.

The load values are passed explicitly to the numerical EHL model along with entrainment velocity, lubricant and solid properties. From the nodes presented, the pressure distribution and film thickness across the contact are obtained. These are presented in Figure 18.

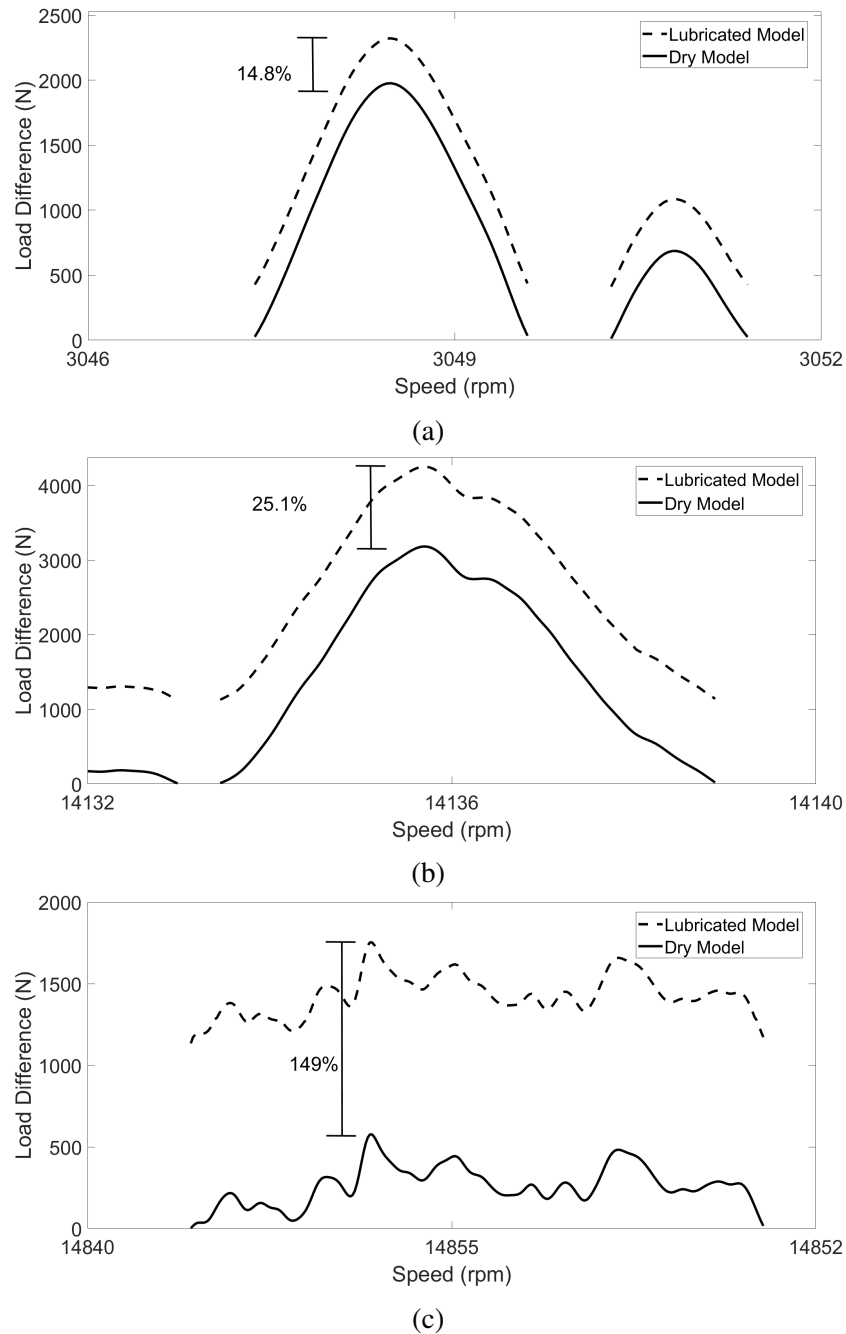


Figure 3.17 Dry and lubricated model load difference: a) 3 050 rpm, b) 14 135 rpm, c) 14 855 rpm.

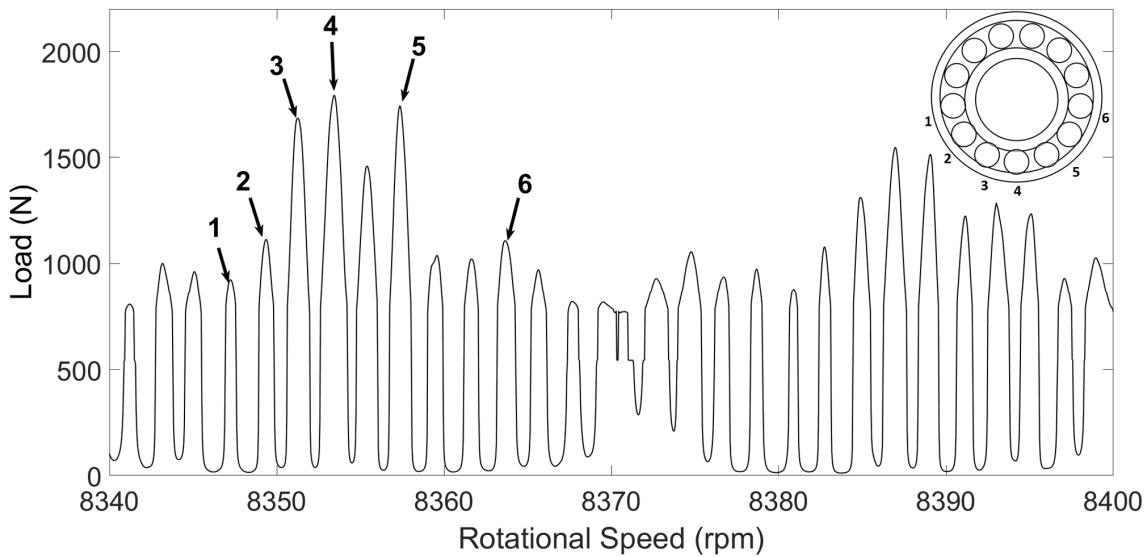


Figure 3.18 Selected points for the numerical EHL model.

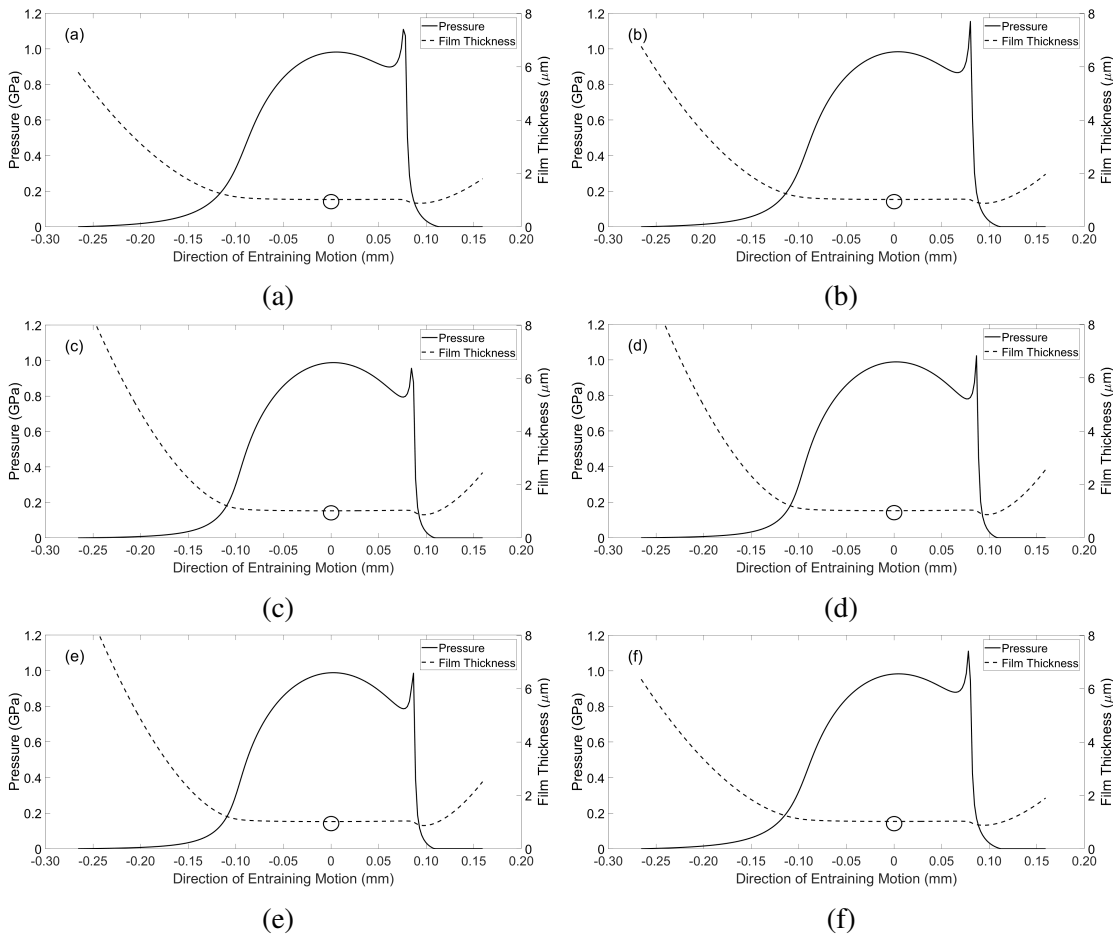


Figure 3.19 EHL pressure and film thickness distributions: a) Node 1, b) Node 2, c) Node 3, d) Node 4, e) Node 5, f) Node 6.

Table 3.4 Extrapolated Film Formulae and Numerical Model Central Film Thickness Comparison

Node	Extrapolated Formulae Central Film Thickness (μm)	Numerical Model Central Film Thickness (μm)	Percentage Difference (%)
1	1.142	1.026	11.3
2	1.122	1.025	9.46
3	1.075	1.019	5.49
4	1.068	1.016	5.11
5	1.072	1.018	5.30
6	1.122	1.025	9.46

In each of these plots, it is possible again to see the central film thickness drop as the roller enters, then exits the loaded region. These central film values are represented by circles in Figure 18. Agreement between the extrapolated film formulae and the numerical model for calculating central film values are presented in Table 3.4. This confirms the validity of using extrapolated film thickness equation in the implicit tribological model. It is shown that the central nodes which correspond to the higher loads in the loaded region have the lowest percentage difference in comparison to the lightly loaded nodes at the outer edges.

3.5 Conclusions

A new methodology comprising experiments and numerical modelling has been developed to allow component and conjunction level tribodynamic analysis of a roller bearing under speeds and loading conditions previously not reported. The experimental data contain the physics of the dynamics and tribology within the bearing, negating the need for a simplified and computationally intensive dynamic bearing model. The tribological conditions at the contact between an individual roller and raceways are numerically analysed. All possible lubrication regimes, including mixed-EHL and hydrodynamic, are considered as the roller passes through loaded and unloaded regions. The following conclusions can be made based on presented results:

1. The contact experiences an order of magnitude increase in film thickness across the speed sweep. This highlights the necessity of implicitly including the lubricant

film in any predictive tribodynamic model; an approach that is not reported on in open literature for high-speed dynamic roller bearing analysis.

2. A comparison between the dry and lubricated contact model further reinforces the need to include the lubricant film in high-speed roller bearing analysis, with percentage differences in load between both models up to 149% at 15 000 rpm. Neglecting this film by using the common dry Hertzian approach would lead to an underestimation of the total load at the roller-race contact.
3. At higher speeds, such as those present in modern electric powertrains, it is shown that the growth of the lubricant film must be included implicitly within the dynamic bearing analysis.
4. The load values obtained from the lubricated tribological model have been used explicitly within a 1D EHL model to calculate the pressure distribution and film thickness across the contact. The workflow of using an explicit EHL model based on the analytical tribological contact mechanics is valid, with good agreement between central film thickness values for both.
5. The explicit EHL approach significantly improves the computational efficiency of the model whilst maintaining accuracy, since only the central value of the film is required in the load calculation. This can be implicitly coupled to broaden the scope of the analysis that is being performed.

Chapter 4

Modelling Lubricated Bearings in a Flexible Multi-Body Dynamic Environment

4.1 Introduction

The previous chapter highlights the necessity of implicitly modelling the EHL film at the roller-race contact. A workflow was established to implicitly account for the lubricant film at the roller-race conjunction. However, bearing motion is obtained experimentally, which limits the investigation to component level analysis. Since this work aims to investigate the effect of the EHL film at system level, and dynamic model must be developed.

This chapter presents a new flexible dynamic model for drive systems comprising lubricated bearings operating under conditions representative of electrified vehicle powertrains. This is achieved by embedding a non-linear lubricated bearing model within an FMBD model; something which has not, to the authors' knowledge, been reported on hitherto. The time-varying system operating conditions reflect that of an electrified powertrain. The kinematic behaviour of a flexible shaft at each time step of a dynamic simulation is passed to the bearing model. A contact slicing method [11] is employed to calculate the reaction forces of the individual rolling elements based on the roller-race contact deflection [119]. The total deflection is influenced by the thickness of the EHL film within the contact, which is implicitly included within the analysis through an iterative procedure. The resulting race forces are returned to the system level model and the equations of motion are solved at each time step. Comparisons are made between modelling the bearings as dry and lubricated. The dynamic results including

acceleration, force magnitudes and stiffness variations have been obtained for realistic loading conditions of a 54 kW electric hub motor up to speeds of 21 000 *rpm*.

The elastohydrodynamic (EHL) film is shown to increase contact deflection, leading to increased contact forces and total bearing stiffness as rotational speeds increase. Results show that at 21 000 *rpm*, the input bearing EHL film reaches a thickness of 4.15 μm . The lubricant entrainment increases the roller–race contact deflection, causing the contact stiffness to increase non-linearly with speed. The contribution of the lubricant film leads to a 16.6% greater bearing stiffness at 21 000 *rpm* when compared to conventional dry bearing modelling methods used in current multi-body dynamic software.

4.2 Methodology

A co-simulation methodology combines a system level model of a flexible shaft and rigid housing, developed in AVL EXCITETM, with component level models of the lubricated bearings, developed in MATLAB and Simulink. Operating conditions such as rotational speed and external forces are defined in the system level model. Time step, iteration accuracy and simulation length are also defined. Material, geometric and rheological properties of the bearings are defined in the component level model. The kinematic conditions from the system level model (i.e., displacements and velocities in all active degrees of freedom) are passed to the component level model at each time step. For each individual rolling element, the non-linear force–deflection relationship is employed in conjunction with the EHL film calculations to compute the contact reaction force between the roller and race. The resultant force on the inner bearing race due to the contact forces and orbital positions of all elements is then returned to the system level model. The equations of motion are then solved, and the time step is advanced once numerical convergence is achieved. A flowchart of these models representing each time step of the simulation is shown in Figure 4.1.

4.3 System Level Flexible Model

The system level model consists of a flexible shaft, supported by two cylindrical roller bearings in a rigid housing (see Figure 4.2). The shaft is 472.5 mm between bearing centres, with a 50 mm main diameter and 25 mm diameter bearing seats. The cylindrical roller bearings act as interference elements between the shaft and housing. The shaft can exhibit lateral motion in both vertical (z) and horizontal (y) directions and rotation about the x -axis (see Figure 4.2). External load is applied at the shaft centre as a time-varying

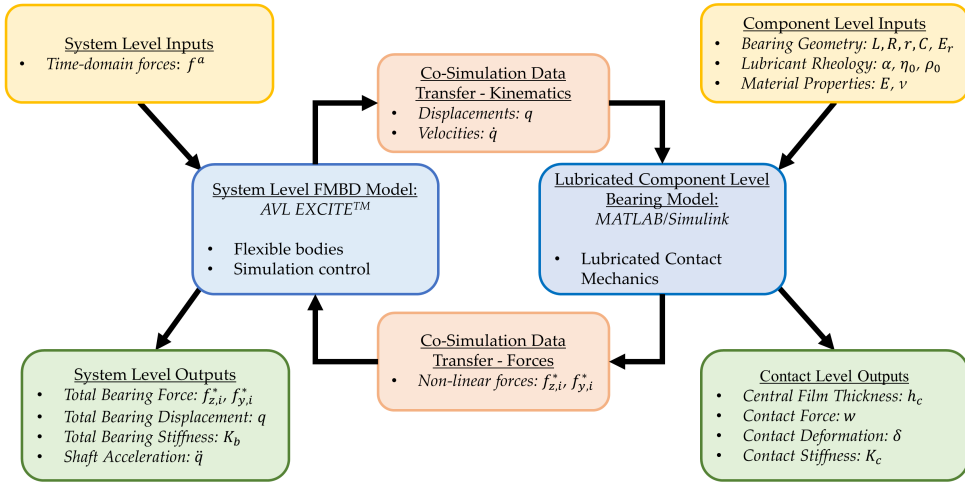


Figure 4.1 Flowchart of models.

input force, to simulate the gear mesh excitation, or as a static load. The rotational speed is input as a boundary condition.

In typical configurations containing flexible structures, it is possible for both the inner and outer races of a rolling element bearing to move when subject to load. For this analysis, however, it is sufficient to fix the outer race in space and consider only the displacement of the inner bearing race [13]. The housing in this study is treated as a rigid body of infinite stiffness; therefore, the race dynamics of the bearing are influenced only by the motion of the flexible shaft in the model. The loading on the inner race is reacted by the rolling elements on the inner raceway; this must therefore be solved to achieve a dynamic equilibrium.

Within the model, the shaft is treated as a body having linear elastic behaviour and the housing is treated as rigid. The bearings are modelled via non-linear contact forces acting between the shaft and housing.

The shaft is represented by a condensed finite element model and is discretised into a sufficiently high number of partial masses [120]. The total elastic deformation of the shaft is represented by translational and rotational displacement components of these individual partial masses. The mathematical modelling used in the FMBD solver is based on Newton's equations of motion and Euler's equation of angular momentum, respectively:

$$m_i \frac{\partial^2 x_i^{Abs}}{\partial t^2} = f_{F,i}^{Abs} \quad (4.1)$$

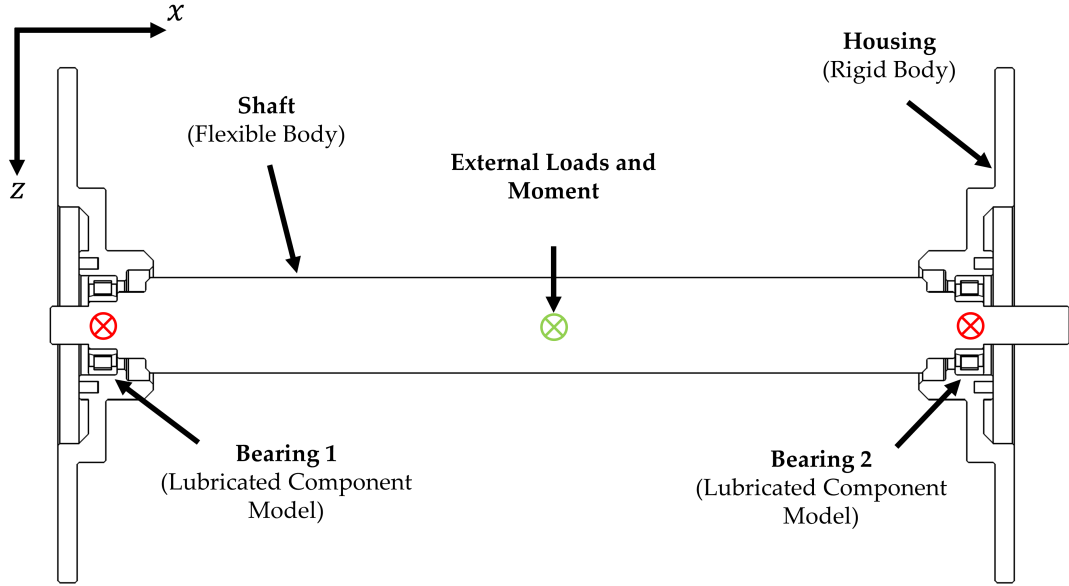


Figure 4.2 System level model schematic.

$$\frac{\partial}{\partial t} \left(I_{C,i}^{Abs} \omega_i^{Abs} \right) = f_{M,i}^{Abs} \quad (4.2)$$

where m_i and $I_{C,i}^{Abs}$ represent the mass and inertia tensors of the partial masses, i . The vectors of displacement and angular velocity are represented by x_i^{Abs} and ω_i^{Abs} respectively and are related to the centre of gravity of each partial mass. The force and moment vectors, $f_{F,i}^{Abs}$ and $f_{M,i}^{Abs}$, must be fulfilled for all partial masses in the shaft.

The combination of displacement and rotations of the shaft takes the form:

$$M\ddot{q} = f \quad (4.3)$$

where M represents the block-diagonal mass matrix of the shaft, consisting of the sub-matrices $M_i, i \in \{1, \dots, n\}$ that make up each partial mass of the full shaft. Acceleration, \ddot{q} , represents the second derivative of the displacement vector of all partial masses, $q = (q_1, q_2, \dots, q_n)^t$. Each element of this vector has 6 elements associated with it that represent the 6 degrees of freedom - 3 rotational and 3 translational ($q_i = (u_{i1}, u_{i2}, u_{i3}, \theta_1, \theta_2, \theta_3)^t$)

The forces and moments acting on each partial mass are contained in sub-vectors of force, $f = (f_1, f_2, \dots, f_n)^t$. These are split into a sum of internal force terms, f_i^{int} , external force terms, f_i^{ext} , and non-linear inertia terms, p^* . As with the partial mass terms, these are made up of six elements, each representing a degree of freedom:

$$f_i^{int} = \begin{pmatrix} f_{i,1}^{int} \\ f_{i,2}^{int} \\ f_{i,3}^{int} \\ f_{i,4}^{int} \\ f_{i,5}^{int} \\ f_{i,6}^{int} \end{pmatrix} \quad (4.4)$$

where each component of force, $f_{i,k}^{int}, k = 1, \dots, 6$ is evaluated using the linear-elastic approach

$$f_{i,k}^{int} = \sum_{j=1}^{6,n} f_{i,j,k}^{int} \quad (4.5)$$

$$f_{i,j,k}^{int} = - (d_{i,j,k} \dot{q}_k + k_{i,j,k} q_k) \quad (4.6)$$

where d and k represent the material damping and stiffness coefficients, respectively.

Grouping the damping and stiffness coefficients into one matrix gives the equation of motion after rearrangement. This equation represents the behaviour of the total system of rigid partial masses that make up the shaft, and considers both general global motion and small body motion (vibrations) [121]:

$$M \cdot \ddot{q} + D \cdot \dot{q} + K \cdot q = f^{ext} + p^* \quad (4.7)$$

The vector of external forces and moments, f^{ext} , is the sum of excitation forces, f^* , and external loads, f^a . External loads and moments applied to the shaft, f^a , are determined functions given in time and are input as both time-varying and static loads on the system. The non-linear excitation force term, f^* , represents the reaction forces from the lubricated component level bearing model.

$$f^{ext} = f^* + f^a \quad (4.8)$$

Partial mass displacements (q_i) and velocities (\dot{q}_i) at the bearing locations are output from the dynamic model and used as boundary conditions within the lubricated component level bearing model at each time step of the simulation. This model returns resultant forces and torques on the inner race of each bearing (f_i^*) which are then used to solve the equation of motion (Equation 4.7) within the dynamic model (see Figure 4.1).

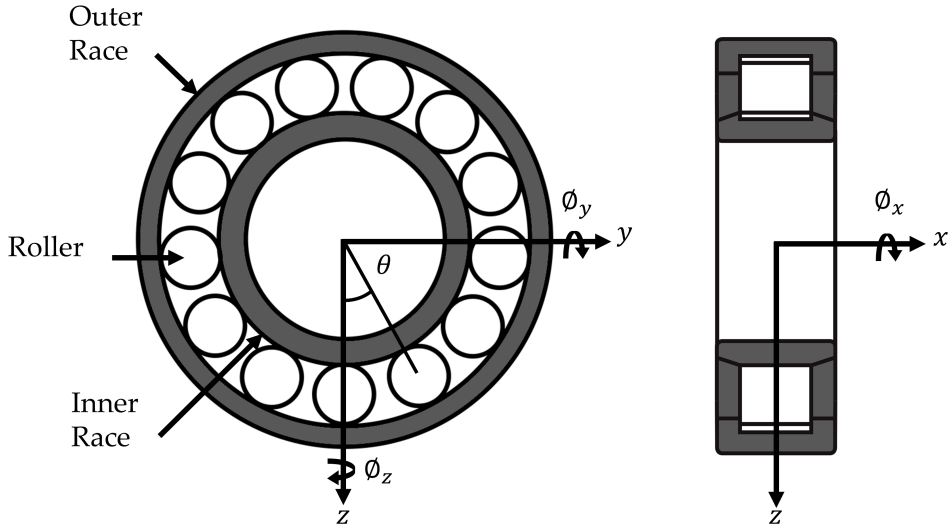


Figure 4.3 Bearing schematic.

4.3.1 Lubricated Component Level Model

The displacement and velocity vectors from each node connecting the shaft to the bearings (q_i and \dot{q}_i respectively) comprise six-DOF. For this lateral DOF model, translations in z and y are considered, as well as angular displacement around the rotational axis, x . A schematic of the bearing is shown in Figure 4.3.

Between the roller and raceways, under sufficient load, the pressures in the non-conformal contact are high enough to cause elastic deformation of the surfaces and a significant increase in lubricant viscosity. This, combined with relative motion between contacting bodies, leads to the generation of an EHL contact. The stiffness of the EHL film is typically 1-2 orders greater than the stiffness of the contacting bodies [27]. In this analysis, the film stiffness was calculated using:

$$K_{EHL} = \frac{dw}{dh_c} \quad (4.9)$$

The lowest average film stiffness was 5.1×10^9 N/m, which is over one order greater than the contacting material stiffness. The material therefore dominates the stiffness of the contact, and the stiffness of the EHL film can be neglected. The film is modelled as a rigid element that is present between the roller and race [100] [101] [102].

The contact deformation (δ) is therefore a function of the displacement of the inner bearing race, angular displacement of the roller about the rotational axis (θ), central

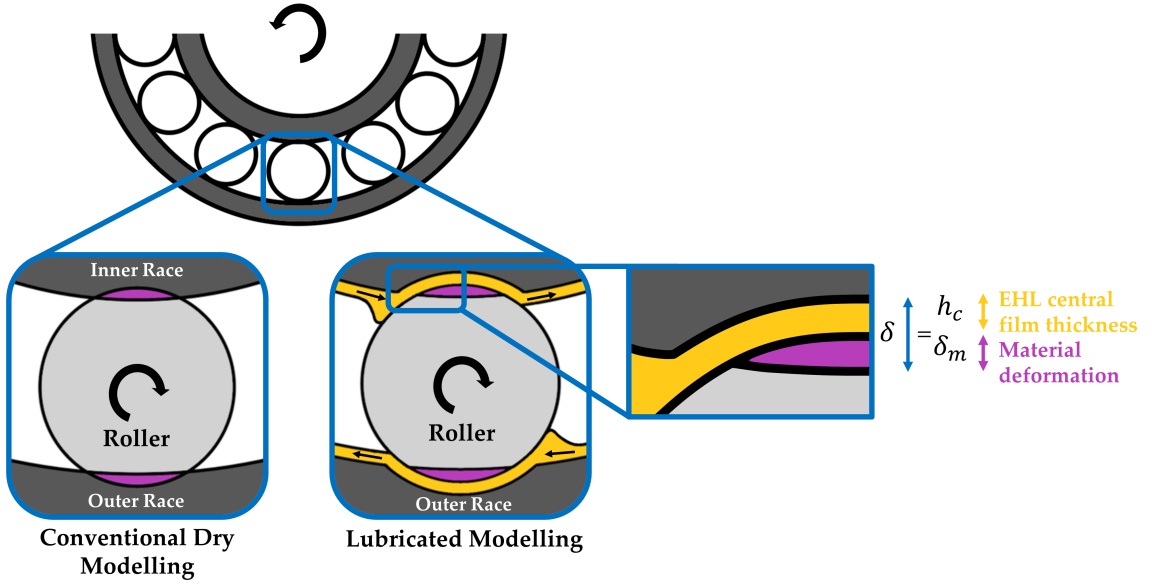


Figure 4.4 Dry vs lubricated roller-race contact.

EHL film thickness (h_c) and any clearance or radial preload ($\pm C$) within the bearing [29] [31]:

$$2\delta = 2(h_c - C) + z \cos(\theta) + y \sin(\theta) \quad (4.10)$$

Figure 4.4 demonstrates this more clearly. The total contact deformation is the summation of (h_c) and the material deformation, (δ_m) predicted from the dry-Hertzian contact assumption. Conventional dry analysis only accounts for the dry material deformation at the contact.

The extrapolated central film thickness for a line contact, assuming a fully flooded contact inlet, is therefore obtained from [52]:

$$h_c = R_r \left[3.06 G^{*0.56} U^{*0.69} W^{*-0.1} \right] \quad (4.11)$$

where the following dimensionless parameters are used:

$$W^* = \frac{W}{E_r R_r l_a}, U^* = \frac{\eta_0 U}{E_r R_r}, G^* = E_r \alpha \quad (4.12)$$

Comprehensive analytical models [122] [123] account for the tilting and skew of the rolling elements. Skew has the effect of varying the entrainment speed along the length of the roller, and tilt will affect the contact gap. Due to the stiff housing and shaft used in this analysis, the tilt and skew angles are very small. The entraining motion and

contact gap along the contact length can be considered consistent, and a 1-dimensional analysis for EHL film thickness is therefore appropriate [22].

The bearings are modelled with light preload due to mounting interference. In practical applications, preload is applied to prevent skidding and chaotic behaviour due to the emergence of zero stiffness regions [124]. In contrast, excessive preload can lead to frictional power loss and wear. Assuming pure rolling, the speed of entraining motion is given by [125] [126]:

$$u = \frac{R\omega}{r} \left(\frac{(R+2r)}{(R+r)} \right) \quad (4.13)$$

Due to the dependency of load on film thickness, an iterative approach is performed to calculate the contact force. Convergence criteria for the EHL film must be met at each time step of the simulation before the bearing forces are returned to the system level model and the equations of motion are solved:

$$\frac{h_c^m - h_c^{m-1}}{h_c^{m-1}} \leq 0.001 \quad (4.14)$$

where m represents the iteration number.

Individual roller-race contact forces are calculated based on the contact deformation. In the case of a rolling element, a cylindrical body of finite length, the contact problem is non-Hertzian. The surfaces cannot be modelled as locally quadratic due to the presence of crowned (rounded) edges [127]. The most widely used technique to calculate the force-deflection relationship is the contact slicing technique. Whilst this does not reflect edge stress concentrations, these stresses are only distributed over a small area and hence can be neglected for the purpose of force equilibrium [128]. In general, this technique is favoured for its simplicity, speed, and sufficient accuracy. The contact slicing technique employed in this study was developed by Andreason [11] for modelling these non-Hertzian line contacts.

Modelling the roller-race contacts as a line contact between a cylindrical roller and a flat surface, Lundberg's [119] expression between contact force per unit length (w) and deformation (δ) was used.

$$\frac{\delta}{l_a} = \frac{2w}{\pi E_r l_a} \ln \frac{\pi E_r l_a}{w} \quad (4.15)$$

where E_r is the equivalent elastic modulus of the two materials and l_a is the active length of the roller. This assumes that the pressure distribution is uniform along the length of the contact, and elliptical across it. This neglects side leakage along the contact

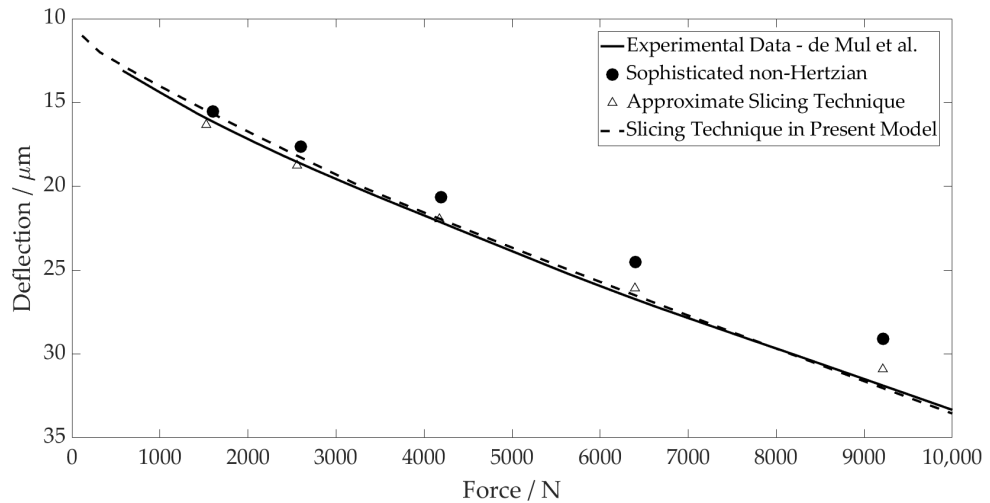


Figure 4.5 Contact level validation.

(x_c) due to the contact dimensions in this direction being much larger than dimensions across it (y_c) . This is valid apart from the small regions at the edges of the contact.

From Equation 4.15, contact forces per unit length of an individual slice along the roller-race contact can be calculated. This is valid if there is no separation of the bodies, i.e., the contact deformation does not become negative ($\delta_k > 0$).

$$w_s = \pi E_r l_s \left(\frac{0.5 \delta_s}{7.358 l_s} \right)^{1.11} \quad (4.16)$$

where s represents the slice number, and l represents the slice length.

The application of the slicing technique was validated against open literature [13]. The study compared results obtained from an experimental rig with numerical results calculated using both the approximate slicing technique and the sophisticated non-Hertzian technique [129]. By replicating the geometry of the test bearing used in their analysis, the application of Andreason's slicing technique used for this analysis was validated with good agreement (see Figure 4.5). This method is a much faster way of calculating contact load and moment than more sophisticated methods by [13], yet still maintains high accuracy.

The total contact load W and moment T are obtained by summing the contributions from all loaded slices:

$$W = \sum_s w_s l_s \quad (4.17)$$

$$T = \sum_s w_s l_s x_{c,s} \quad (4.18)$$

with $x_{c,s}$ being the distance to the centre of each slice in the conjunction coordinate system. It is assumed that total contact deflection is shared equally between the inner and outer races despite slight differences in contact geometry. The entrainment velocity is equal at each contact, which is the governing parameter for the lubricated contact force differences.

Experimental measurements show that the damping of a rolling element bearing arises from multiple sources [27], including:

1. Lubricant film damping at the contacts.
2. Material damping due to Hertzian deformations.
3. Interface damping between assembled components

These measurements show that damping decreases with rotational speed, tending towards a constant value. Sopanen and Mikkola [17] summarize the findings of Mitsuya et al. [130] and Aini et al. [30], concluding that the film damping is moderate. The linearized viscous damping method adopted in their study is therefore also adopted here. The damping force for each roller is obtained as a factor of the contact stiffness and contact penetration velocity [131]. This is defined as:

$$|F_d| = -f_{\text{damp}} K_c \dot{q} \quad (4.19)$$

where K_c is the contact stiffness, and the damping factor, f_{damp} , is in the range of $(0.25 - 2.5) \times 10^{-5}$ as reported by [131].

At each time step of the analysis, these calculations are performed for each individual roller in the complement. The total bearing force acting on the inner race is solved by splitting the total contact force on each roller into its components and summing their contributions.

$$f_{z,i}^* = \sum_N W \cos(\theta) - \sum_N F_d \cos(\theta) \quad (4.20)$$

$$f_{y,i}^* = \sum_N W \sin(\theta) - \sum_N F_d \sin(\theta) \quad (4.21)$$

Due to the bearing preload, contact is maintained throughout the rollers' orbit; hence no emerging clearances are modelled in the lubricated analysis. The contact separation is also unaffected by rolling element centrifugal forces, which are negligible when compared to the contribution of the dynamic load and the EHL film in this study. These have therefore been neglected.

Table 4.1 Cylindrical Roller Bearing Specification

Parameter	Value
Inner race bore diameter	25 mm
Pitch diameter	60 mm
Roller diameter	8.8 mm
Roller length	15 mm
Number of rollers	17
Radial interference	2 μm

Table 4.2 Bearing Rheological Properties

Parameter	Value
Pressure viscosity coefficient (α)	$2.1 \times 10^{-8} \text{ Pa}^{-1}$
Atmospheric lubricant dynamic viscosity	0.08 Pa.s
Lubricant inlet density (ρ_0)	$833.8 \text{ kg} \cdot \text{m}^{-3}$
Modulus of elasticity of contacting solids	210 GPa
Poisson's ratio of contacting solids	0.3

Surface measurements of the rollers used in this analysis were taken using an Alicona InfiniteFocus Variation Microscope. The composite surface roughness value of a roller and inner race was calculated to be 91.3 nm. This gives a lambda value of 5.88 for the thinnest EHL film at 1000 rpm. Asperity interaction is not considered as the EHL film fully supports the load. Due to the pure rolling and zero sliding assumption, friction at the contacts is therefore neglected and the analysis is performed under isothermal conditions.

The bearing geometry is detailed in Table 4.1. Rheological and material properties are detailed in Table 4.2, representing ambient operating conditions in an individual hub-motor transmission.

4.3.2 Representative Excitation Methodology

The system level model is decomposed, with excitation forces calculated externally before application within the model. A separate electrified transmission model is used

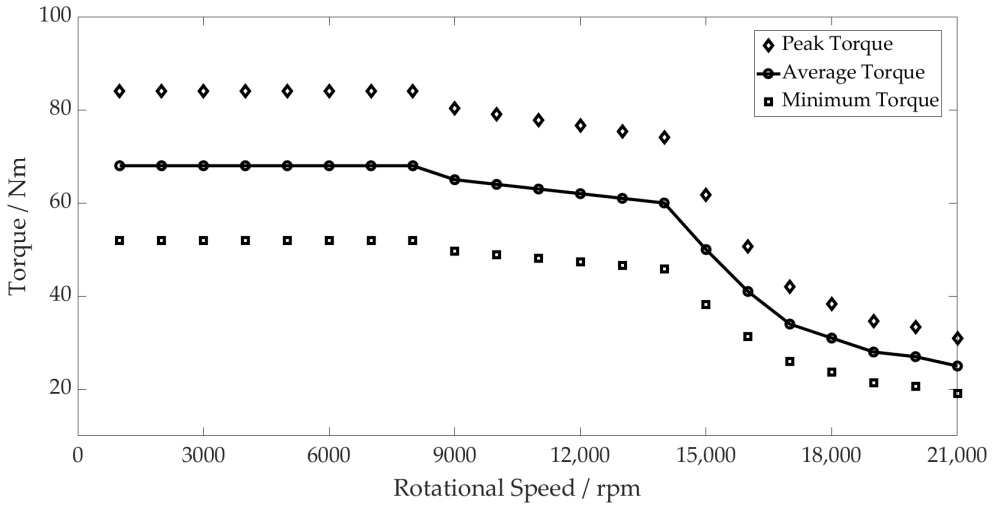


Figure 4.6 PMSM torque profile and maximum and minimum torque fluctuation.

to generate realistic excitation forces and torques from a spur gear pair and a permanent magnetic synchronous motor (PMSM). This system represents the first stage of an electric hub motor used in automotive applications.

Radial and tangential gear pair forces at the pinion centre, as well as torque fluctuations of the electric motor are extracted to be used as inputs to the system level model. These are applied as external forces to the shaft, f^a , from Equation 4.8. All bodies in this separate system were modelled as rigid, so that structural excitation forces did not contribute to the resultant forces at the pinion.

The motor has a peak torque of 68 Nm, and a maximum operating speed of 21 000 rpm. The torque transfer through the gear pair reduces as the speed increases due to the torque profile of the PMSM, as shown in Figure 4.6. Stator tooth forces from the PMSM are neglected in the model due to their minimal contribution to lateral forces once resolved. For input to the model, the radial and normal forces are simplified by adopting sinusoidal inputs of the same magnitude and frequency of the gear pair at different speeds. The torque ripple from the motor is simplified using the same method.

4.3.3 Co-Simulation of Coupled Models

A coupled simulation approach is employed to implement the lubricated components level bearing model within the flexible multi-body dynamic (FMBD) environment. AVL EXCITE™ Power Unit R2022.1 contains integrated “Link to MATLAB” functionality, whereby joints within the model can be replaced with a user function created in MATLAB Simulink® R2022b.

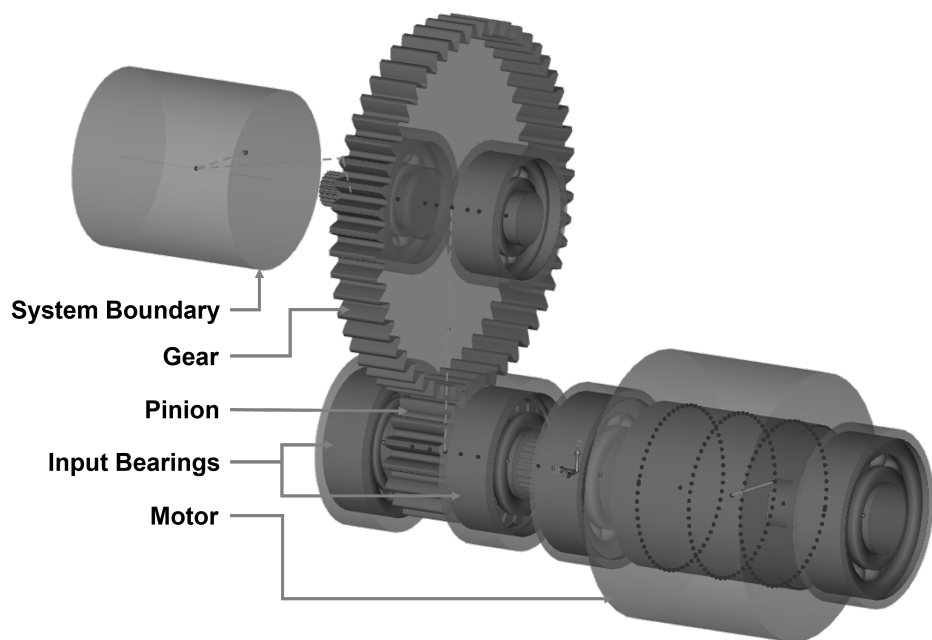


Figure 4.7 Hub motor excitation model.

Table 4.3 Pinion Geometry

Parameter	Value
Number of teeth	17
Normal module	0.004 <i>m</i>
Normal pressure angle	20 °
Helix angle at pitch circle	0 °
Active tip diameter	0.076 <i>m</i>
Active root diameter	0.065 <i>m</i>
Width	0.035 <i>m</i>

Table 4.4 Gear Geometry

Parameter	Value
Number of teeth	51
Normal module	0.004 m
Normal pressure angle	20 °
Helix angle at pitch circle	0 °
Active tip diameter	0.212 m
Active root diameter	0.202 m
Width	0.030 m



Figure 4.8 Communication vector and degrees of freedom.

Connected Degrees of Freedom Connections are created between bodies in the FMBD software using pins. Pins are assigned to specific nodes on the shaft and housing. The pins transmit a 6-element vector that describe the 6 DOF of the connection point. The first 3 elements represent translational DOFs, whilst the latter represent rotational DOFs. This are concatenated into a single communication vector that is then transferred to MATLAB®.

Two vectors are transferred from EXCITE to MATLAB® one containing displacement information in all 6 DOF and the other containing velocity information. Force vectors of equal size are then computed within the component level model in MATLAB® and returned to EXCITE™ Power Unit.

The connection to MATLAB® is facilitated via an S-function. Therefore, a Simulink® model is required. A generic block developed by AVL, the EXCITE™ Power Unit Simulink® block, is used for this purpose:

Output Port Output data from the FMBD model is organised in vector format, of size $6n$ where n is the total number of connections being passed from MATLAB® to EXCITE™ Power Unit. To access data for each connection, and then split this into specific DOFs, two levels of Demux elements are needed.

1. The first level of Demux splits the output vector into n pins, of size 6 to represent the DOFs at each pin.

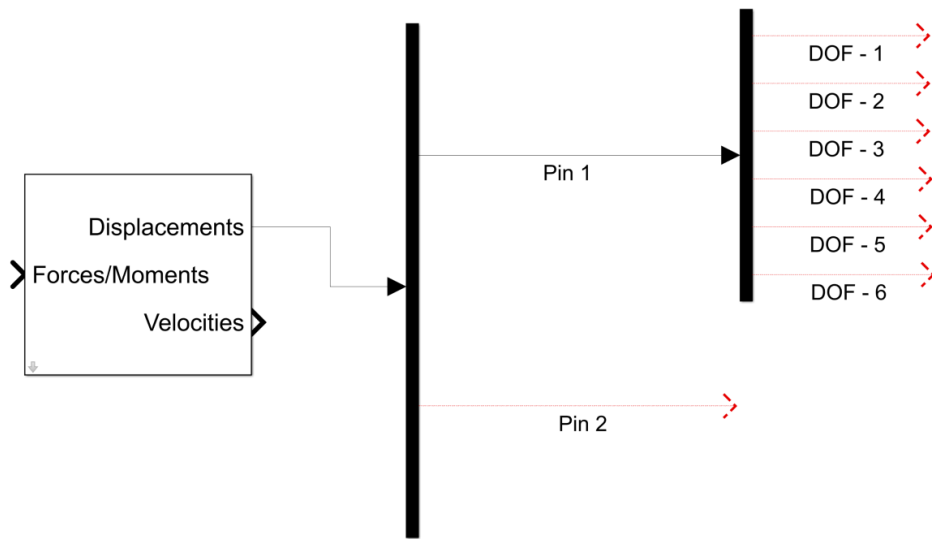


Figure 4.9 Output port Demux blocks and degrees of freedom.

2. The second level of Demux blocks splits the 6-element vector for each pin into the 6 scalar values that represent the data for each DOF. These can then be used as inputs to the MATLAB® function block within the Simulink® model.

Input Port At the input port to the EXCITE™ Power Unit Simulink block, a vector of $6n$ elements must be passed. This requires two Mux blocks: the first to combine the DOFs of each pin, and the second to combine all of these connection vectors into a single vector that is passed to EXCITE™ Power Unit.

Simulink Model To integrate the lubricated bearing model into the Simulink® model, the MATLAB® Function block is used. The input variable sizes are defined at the beginning of the function, and the appropriate DOFs are connected to the block in the order of which they appear in the function. The function blocks and hence lubricated bearing models are highlighted in 4.11, as well as the ports and the demux blocks that split the DOFs.

The coupled simulation supported by EXCITE™ Power Unit is explicit in nature. This means that there is no iteration at each time step between the dynamic solver and the bearing model. A sufficiently fine time step is therefore required to prevent numerical divergence of results due to error accumulation. It was found that a time step of $1e-6$ s was fine enough to ensure numerical convergence, whilst also remaining computationally efficient.

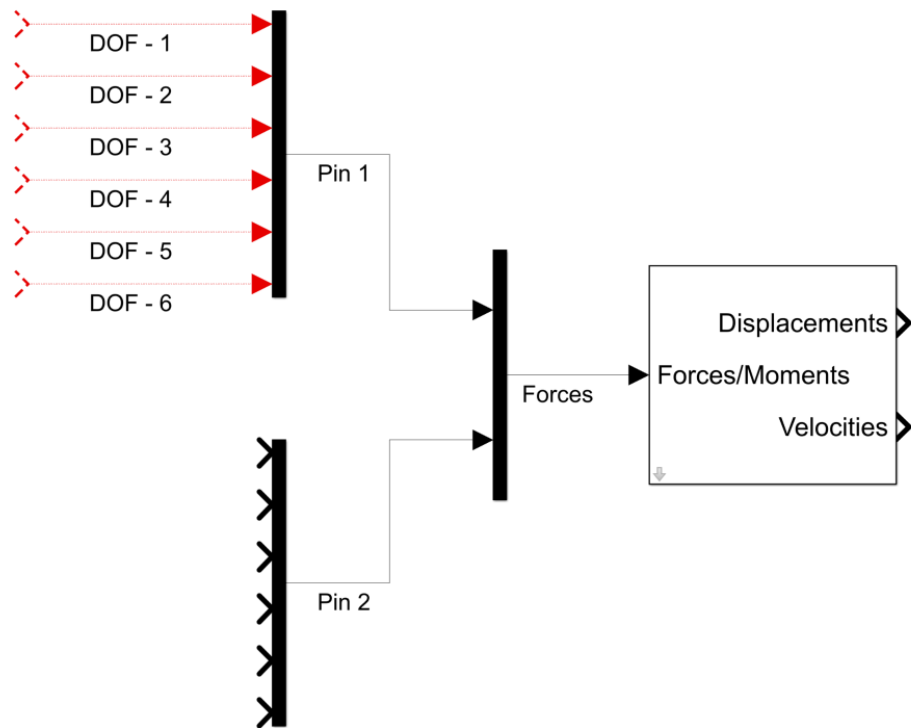


Figure 4.10 Input port Mux blocks and degrees of freedom.

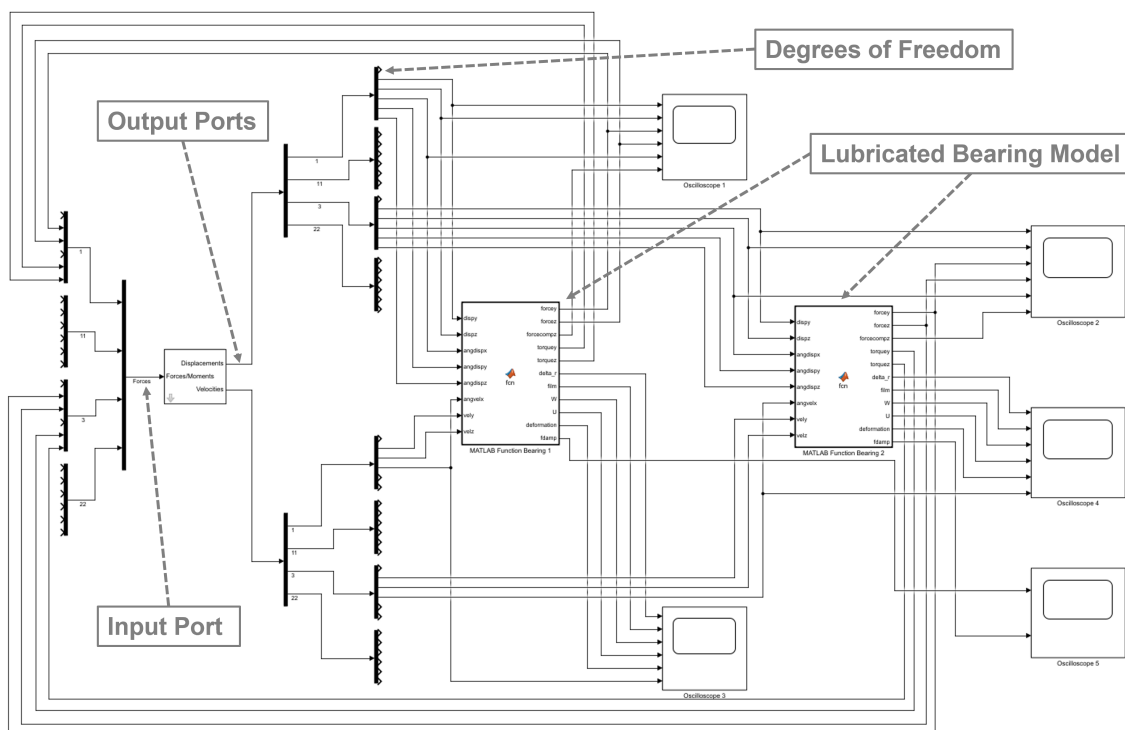


Figure 4.11 Simulink® model schematic.

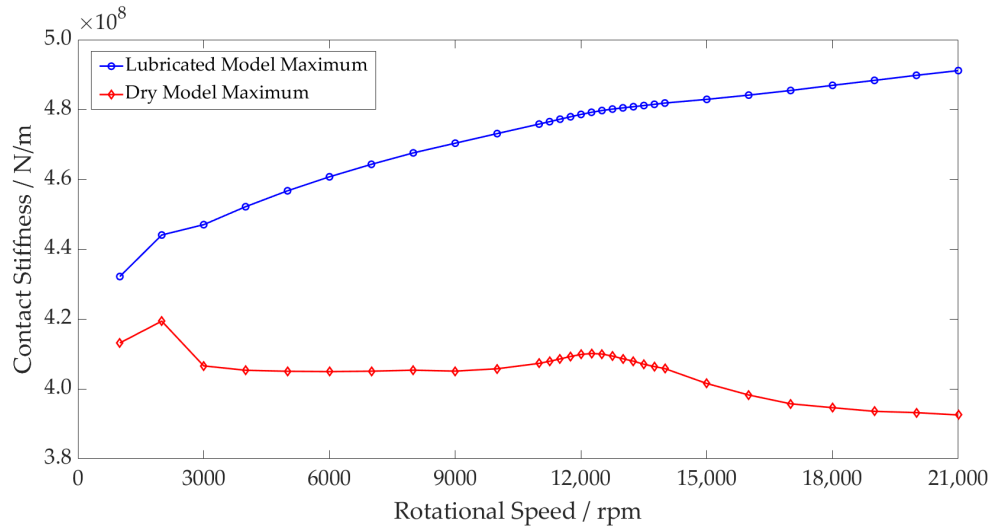


Figure 4.12 Rolling element contact stiffness - Dry vs lubricated maximum values.

4.4 Results and Discussion

A quasi-dynamic speed sweep has been performed from 1 000 to 21 000 *rpm*. The simulations are performed every 1000 *rpm*, refined to 250 *rpm* intervals throughout a period of system resonance between 12 000 *rpm* and 14 000 *rpm*. The operating envelopes are generated by plotting the maximum and minimum values from the steady-state signals at each speed interval. The conjunction level results are obtained from an individual roller and its contact with the inner raceway. The component and system level results are taken from the geometric centre of the inner bearing race, corresponding to the bearing seat on the shaft. The following figures represent results in the *y*-direction, the largest component of excitation due to the tangential force from the gear meshing.

The contact level results (Figure 4.12) show a difference in the contact stiffness between the dry and lubricated models. The dry model follows the torque profile of the motor, with stiffness decreasing as the contact forces reduce. The period of resonance leads to the larger amplitude excitation of the shaft, resulting in an increase in the contact stiffness due to the force-deflection non-linearity. The lubricated model, however, shows an increase in the contact stiffness throughout the speed sweep. This is due to the higher levels of deformation at the contact as the lubricant is entrained, which increases with the shaft rotational velocity. This behaviour was experimentally observed by Dietl, concluding that the oil-wedge between the rolling elements and raceways reduces the internal clearance of the bearing and increases its stiffness [27]. The contact stiffness in the lubricated bearing model under the same operating conditions is therefore 24.9% greater at 21 000 *rpm*.

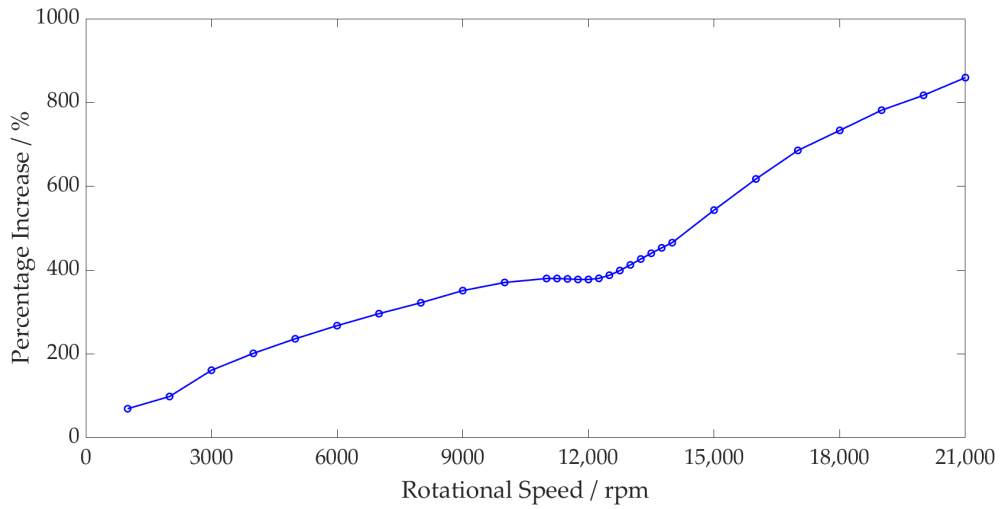


Figure 4.13 Rolling element contact force - Dry vs lubricated percentage increase.

The peak contact force has been compared between both models. The percentage increase between the dry and lubricated models is shown in Figure 4.13. This more clearly shows the disparity between both models at the contact, with the largest difference being 9.6 times at maximum speed. During resonance, the inner race force reaches a peak of 1 514 N, resulting in surface deformation magnitudes of 0.92 μm and 3.81 μm at the dry and lubricated conjunctions, respectively. As noted in previous works [15], higher loads lead to a greater surface deformation to the film thickness ratio, causing the percentage difference between the dry and lubricated models to reduce. Once the loads reduce as the speed increases, the percentage increase continues to rise.

The total bearing stiffness is a combination of all contact stiffnesses between the elements and raceways. These contact stiffnesses vary non-linearly with force, resulting in the total bearing stiffness varying accordingly. For the dry model, this is clearly demonstrated, with the greater total bearing stiffness at the peak of the resonance due to the greater bearing forces (see Figure 4.14). This does not, however, capture the change of the total bearing stiffness with speed; the average bearing stiffness does not change. The lubricated bearing is not only stiffer than the dry bearing, but this stiffness also increases with speed. This is shown in Figure 4.14 by the non-linear increase in the average lubricated bearing stiffness values compared to the constant values for the dry model. The combination of these two factors leads to the lubricated model having a 16.6% greater maximum total bearing stiffness at 21 000 rpm than the dry model.

Due to the greater total stiffness of the bearing, the shaft displacement of the lubricated model is lower both on average and peak to peak for the same applied force in comparison to the dry model (see Figure 4.15). Through the period of resonance, the

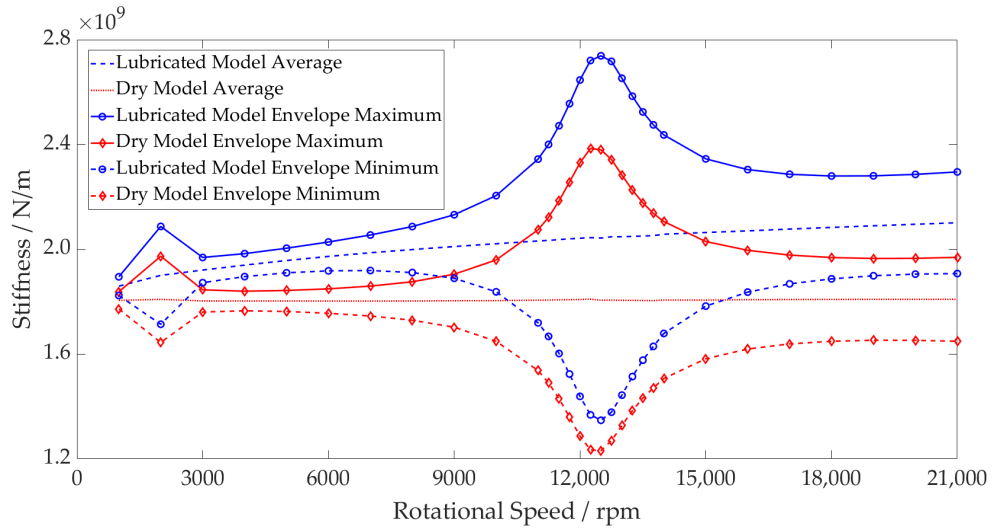


Figure 4.14 Inner race stiffness - Dry vs lubricated operating envelope.

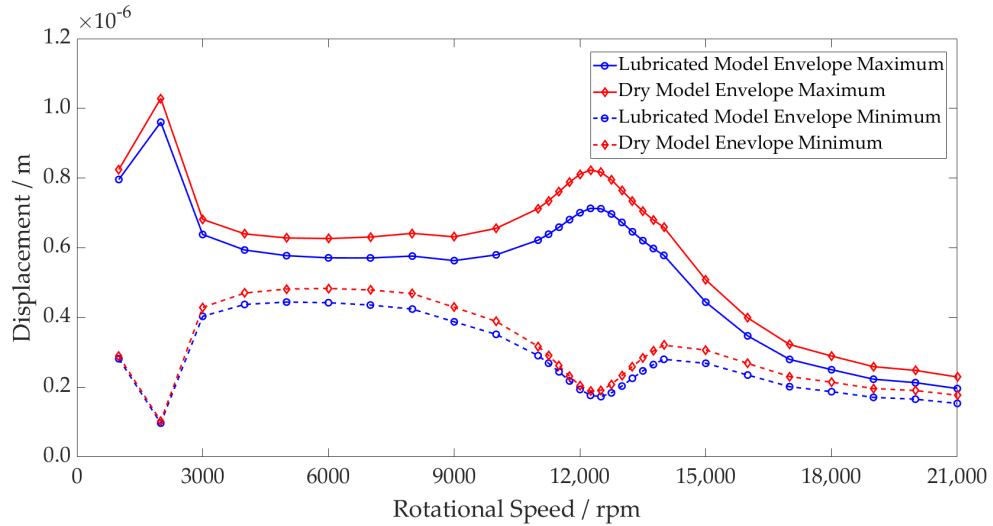


Figure 4.15 Inner race displacement - Dry vs lubricated operating envelope.

large inner race forces result in the roller–race separation of the unloaded rollers within the dry model. This leads to greater shaft displacement as the inner race moves into this region of zero stiffness until roller–race contact is made, and a reaction force is established.

Figure 4.16 shows that the acceleration peak of the system resonance occurs at 12 500 rpm (3 5420Hz) for the lubricated model as opposed to 12 250 rpm (3 470 Hz) for the dry model. This shift in natural frequency indicates a stiffer overall system. The magnitude difference between the dry and lubricated models can also be attributed to the unloaded regions of the dry bearing. The contact deformation arising from the loading of the inner race is sufficient to cause the rollers geometrically opposite to become

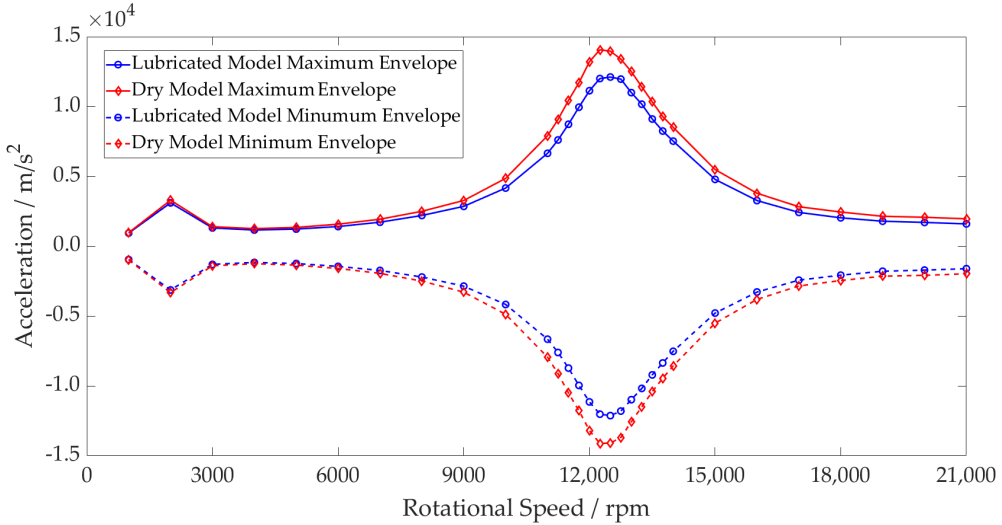


Figure 4.16 Inner race acceleration - Dry vs lubricated operating envelope.

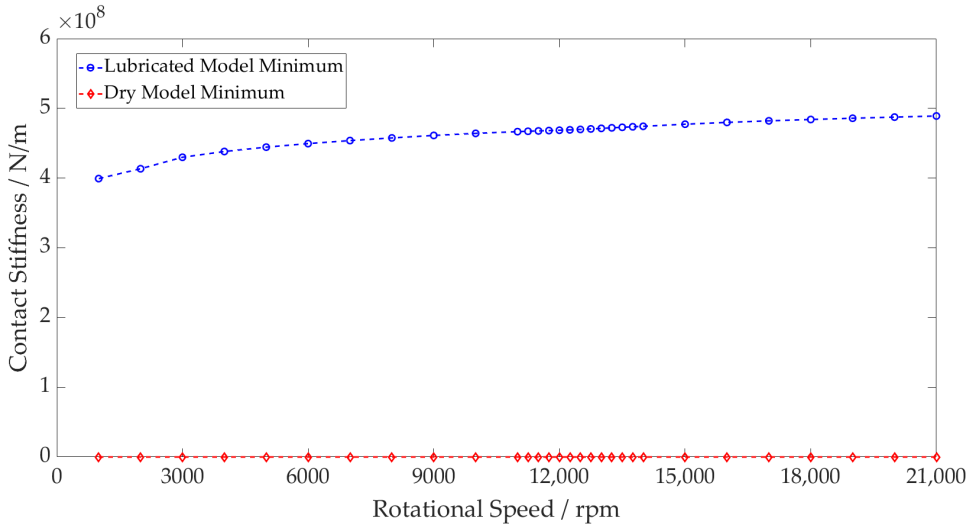


Figure 4.17 Rolling element contact stiffness - Dry vs lubricated minimum values.

separated from their contacts. Contact is lost between the roller and raceway, leading to zero contact stiffness. The inner race moves into this region until it is reacted by a contact force once again. These regions of zero stiffness are shown in Figure 4.17, where the minimum stiffness of an individual rolling element and raceway contact in the dry model drops to zero due to separation. For the lubricated model, contact is maintained throughout.

Analysing the conjunction level results from the lubricated model, the contact force due to the gear mesh frequency is shown superimposed on the ball pass frequency as an individual element passes through the loaded region of the bearings (Figures 4.18 and 4.19). The higher contact forces result in a reduction in the central film thickness, also

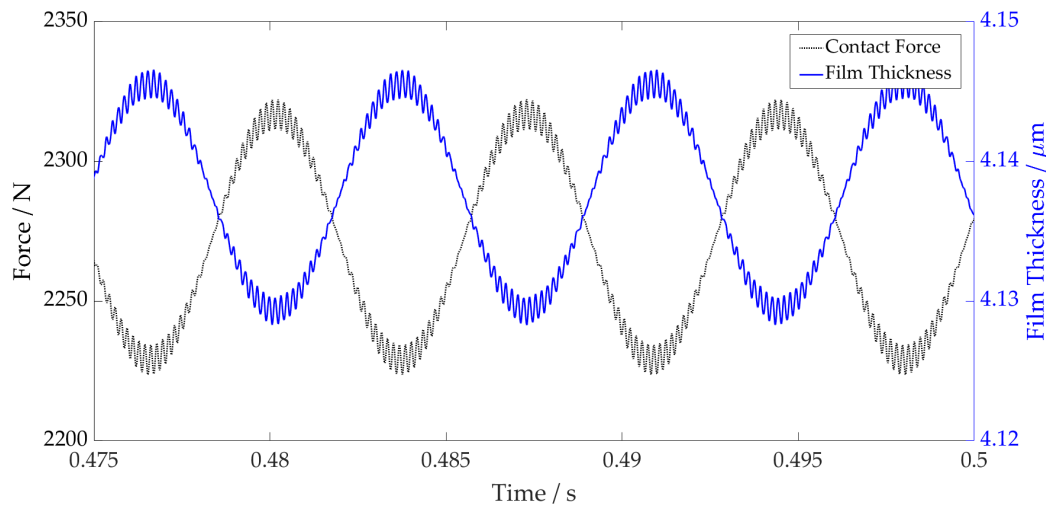


Figure 4.18 Film thickness vs contact force 21 000 rpm.

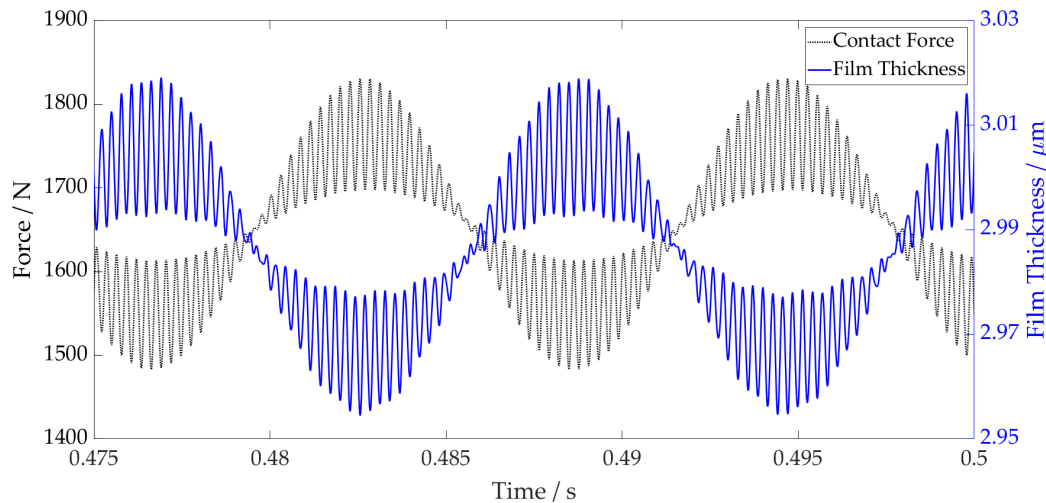


Figure 4.19 Film thickness vs contact force 12 500 rpm.

shown when observing the variation in film thickness for both plots. At 12 500 rpm, the force and film thickness fluctuations are much larger due to the high excitation levels of the shaft during resonance. At 21 000 rpm, even with a much lower torque transfer through the gear pair, the contact forces are greater than at 12 500 rpm. This is due to the contribution of the film enhancing the total contact deflection and hence increasing the contact force.

4.4.1 Conclusions

The new methodology presented has been developed to implement a lubricated bearing model within a flexible system level model. The following conclusions are drawn:

1. Simulations have been performed up to 21 000 rpm with realistic excitation forces from a first stage reduction gear pair and electric motor. The FMBD model implicitly includes the lubricant film at the roller–race contact within the bearing; The conjunction level and system level results have been analysed to compare the lubricated and conventional dry-bearing modelling techniques. This is something that has not, to the authors’ knowledge, been reported previously in the open literature.
2. Results show that the film thickness reaches $4.15 \mu\text{m}$ at 21 000 rpm. This leads to 9.6 times greater contact forces and hence 24.9% greater contact stiffness between the dry and lubricated models due to the lubricant entrainment and non-linear Hertzian force–deflection relationship.
3. The contribution of all the rolling elements leads to the lubricated model having a 16.6% greater maximum total bearing stiffness at 21 000 rpm than the dry model. Moreover, this stiffness is shown to increase with speed due to the film thickness increasing with the entrainment velocity; this is something that dry models do not account for.
4. This increase in the total bearing stiffness leads to a change in the stiffness of the total system. By modelling the shaft as a flexible body, the influence on the natural frequency of the system is seen. The resonant peak at 12 500 rpm shifts 250 rpm higher in the lubricated model, which coincides with the higher frequency excitation from the gear meshing.

Understanding the influence of the roller bearings on the transmission stiffness is of particular importance in automotive applications, and this change shows the effect of the lubricant film on the already complex contact phenomena. Neglecting the effect of the lubricant film can lead to an underestimation of the bearing stiffness, impacting the accuracy of dynamic analyses such as noise, vibration and harshness (NVH) prediction.

As transmissions operate at higher speeds with more complex interconnected structures and noise paths, it is important that these behaviours are modelled accurately. Furthermore, underestimation of the contact forces will also lead to a miscalculation of contact pressures, impacting future sub-surface stress and wear analyses for the life predictions of these crucial critical machine elements.

Chapter 5

Artificial Neural Networks for EHL Film Thickness Predictions

5.1 Introduction

Tribodynamic modelling generally employs analytical equations for the prediction of film thickness in elastohydrodynamic contacts; chosen due to their timely solution. Whilst computationally efficient, these do not achieve the accuracy of the full numerical solution outside the bounds of the data used to generate the analytical equations. In the context of dynamic simulation, a full numerical solution at each time step of a system level model would, however, yield excessive computation time. This has led to the emerging use of data driven solutions, such as machine learning, in the field of tribology. These can achieve accuracy much closer to the numerical solution, whilst significantly improving computational time.

This chapter details the development of an Artificial Neural Network (ANN) for prediction of central film thickness at the roller-race conjunction. ANNs are trained using data generated by the numerical EHL solution, with the data set constrained to realistic operating conditions using the Greenwood regimes of lubrication. Multiple ANNs are compared to find the optimum structure, accounting for training time and accuracy. The ANN is then deployed explicitly, using the boundary conditions of a simple bearing model to test the film thickness accuracy and speed of solution. The trained ANN is then deployed implicitly in the system level FMBD introduced in Chapter 4, replacing the analytical film equations in the model.

The aim of this chapter is to improve the accuracy of the central film thickness estimation, while maintaining a timely solution in the context of a full dynamic solution. This workflow employed is not only relevant to roller bearings; it can be applied to a

wide range of contacts and different sources of training data depending on the modelling requirements.

5.2 Numerical vs Analytical Film Thickness Estimations at High Entrainment Velocities

Two main approaches exist for determination of the complex non-linear problem of film thickness in lubricated contacts. The first approach involves employing numerical methods [49], where systems of partial differential equations are formulated to describe the state of the contact and then solved iteratively [36]. While this method yields accurate results and is applicable to a wide range of operating conditions, it is computationally intensive due to its iterative nature. The second approach involves developing regressed analytical equations from experimental or numerical studies which can be used for specific lubrication regimes. These equations offer quick estimates of key parameters, such as central [52] and minimum film thickness [132]. However, whilst more computationally efficient than the full numerical solution, this approach has limitations.

The applicability of regressed equations is often limited to the range of data used for their development. There is also a requirement for extensive effort in collecting experimental or numerical data to develop them. The entrainment velocities considered in this work (up to 32 m/s) exceed the typical range over which the regressed equations are experimentally derived. Whilst it is possible to exceed the range of input data, it must be done with caution [98].

Figure 5.1 shows a comparison between the central film thickness calculated using the numerical method (see Section 3.3), and the analytical equation (Equation 3.15) across a speed range of $1\,000 - 21\,000\text{ rpm}$. The bearing used for this comparison is the same as in Section 4.3. Geometry is detailed in Table 4.1, with rheological and material properties detailed in Table 4.2.

It is shown that as rotational speed and hence entrainment velocity increase, the film thickness prediction of the numerical and analytical calculations diverge. At $21\,000\text{ rpm}$, entrainment velocities of 30.7 m/s leads to a 22.6% difference between the methods, with the analytical equation overestimating the film thickness.

The implementation of ANNs within tribology is one way to overcome the computational expense of the full numerical solution and this limited validity of the analytical approach. Overcoming the above stated discrepancy is not the only advantage of a numerical EHL informed ANN. Since an ANN can be trained using a wide range of

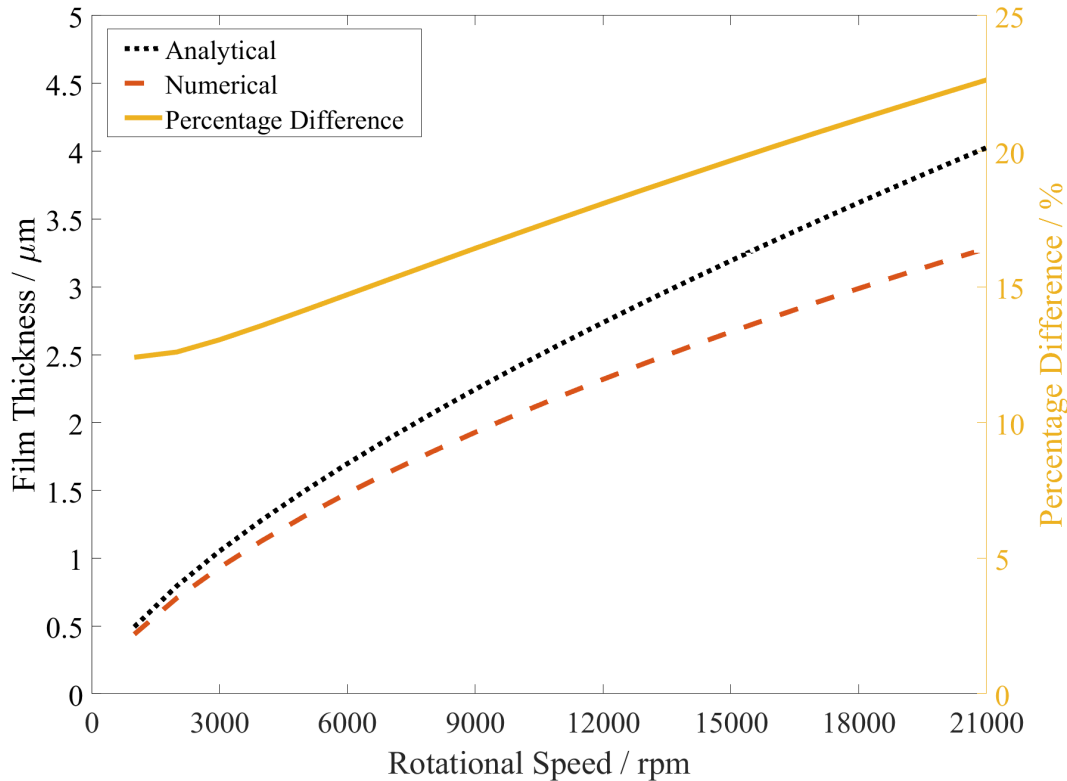


Figure 5.1 Central film thickness - EHL vs analytical.

input data, the effects of other tribological phenomena such as starvation and thermal effects can also be considered. Furthermore, the training of such ANNs is not bound to only numerical inputs; the results of experimental testing could be used to generate an experimentally validated ANN.

5.3 ANN Fundamentals

An Artificial Neural Network (ANN) is a computational model that is inspired by the biological neural networks present in the natural brain [133]. ANNs are a subset of machine learning (ML) that can be trained using supervised, unsupervised, or reinforcement learning techniques. In supervised learning, ANNs are particularly useful for regression tasks, where they can model complex non-linear relationships between inputs and outputs. ANNs compare their outputs with target values during training and, due to their structure, can adapt for a wide range of applications. The goal of this training is to minimize the error, and to improve the ability of the network to generalize and make accurate predictions for new, unseen data.

ANNs consist of a set of interconnected processing elements known as neurons. These are represented computationally as nodes, and the terms are often used inter-

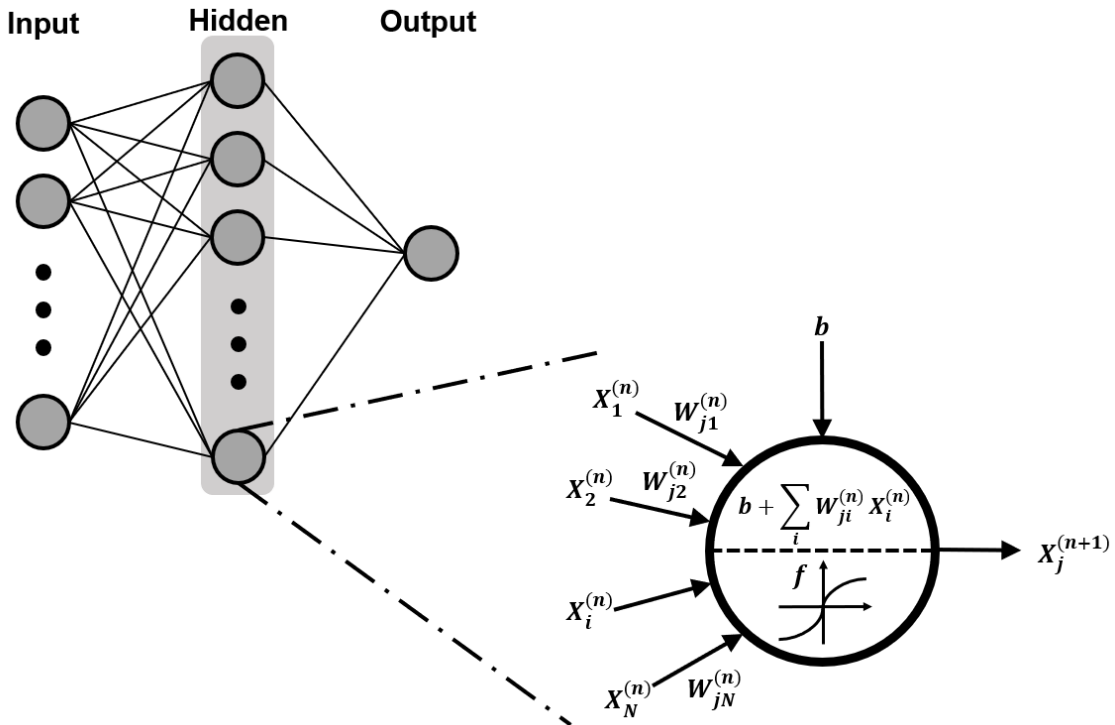


Figure 5.2 ANN schematic

changeably. These elements have the ability to adapt to input data for the purpose of solving complex non-linear functions. The neurons are organized into three main layers, shown in Figure 5.2: Input layer; Hidden layer(s) and Output layer. The adaptation is performed using weighted connections that link each neuron layer. These weightings are adjusted during the learning process, and determine the strength of the connections between neurons.

The following section provides descriptions of the common terms that will be referenced throughout this chapter.

5.3.1 Network Architecture

- **Input layer:** Input data is assigned to input nodes in the first layer of the network. In the case of the film thickness estimation, nine input variables and hence nine nodes are required.
- **Hidden layer(s):** These layers are located between the input and output layer. There can be multiple hidden layers, each consisting of multiple nodes. Multi-layer networks enable the resolution of non-linear problems, whereas single layer networks (no hidden layers) are limited to linear problems [134].

- **Output layer:** The output layer represents the final computed results. For the film thickness estimation, the output consists of a single node corresponding to the predicted central film thickness.

The type of ANN used in this study is called a multi-layer feedforward backpropagation neural network. Forward propagation through the network is used to make predictions based on the input data. Backpropagation is then performed to calculate prediction error and modify the network to minimize this. This process is repeated until the desired prediction accuracy is achieved.

5.3.2 Forward Propagation

Input data propagates through the neural network in the following manner:

1. **Weights:** The input data to the nodes is multiplied by corresponding weights, and a bias term is added (see Figure 5.2). The general equation for ANNs is:

$$z = f(b + \sum_i W_{ji}^{(n)} X_i^{(n)}) \quad (5.1)$$

where z represents the activated output of the neuron. W_{ji} is the weight connecting the i -th neuron of the previous layer to the j -th neuron of the current layer in the n -th layer. $X_i^{(n)}$ is the input value to the neuron from the i -th neuron in the previous layer. The bias is represented by b , and f represents the activation function applied to the weighted sum.

2. **Activation function:** The weighted sum $(b + \sum_i W_{ji}^{(n)} X_i^{(n)})$ is passed through an activation function, f , which introduces non-linearity to the system to enable the learning of complex patterns.
3. **Bias:** The bias term, b , is able to shift the activation function's output. It ensures that a neuron can still activate even in the case where all input values are zero.
4. **Output generation:** Data is propagated through the system until it reaches the final prediction at the output layer.

5.3.3 Backpropagation

The learning process of an ANN is achieved by adjusting the weights in the network. This is done using a process called backpropagation [135]:

1. **Loss function:** During training, the target output of the ANN is known. The predicted output of the ANN is therefore measured against this using a loss function. In the case of ANNs used for regression, mean squared error (MSE) is used.
2. **Backpropagation:** This error is backpropagated through the system to determine the contribution of each weight to that error.
3. **Optimization:** Optimization algorithms, such as Levenberg-Marquardt [136] [137] [138], are used to update the weights and biases to reduce the loss.
4. **Epochs:** The above process repeats over multiple cycles, known as epochs. This is performed until the desired MSE is achieved.
5. **Overfitting:** This is the phenomenon whereby an ANN becomes too specialised at learning the training data, and as a result performs poorly with new, unseen data. This occurs when the network extensively adjusts its internal parameters to fit noise or outliers in the training set [140]. It is therefore necessary to limit the number of epochs once sufficient performance is achieved.

5.4 Methodology

This section details the following methodology:

1. Generating training data for the ANN using the numerical EHL method, and constraining this input data to a range valid for machine element contacts.
2. Evaluating the best ANN structure for the central film thickness estimation.
3. Testing the ANN using by calculating bearing film thickness explicitly based on kinematic condition obtained from a dynamic bearing model.
4. Embedding the ANN within a FMBD model to calculate and implicitly consider the film thickness within the bearing at each time step of the simulation.

The workflow describing the EHL data generation, variable constraints, training methodology and structure evaluation is presented in Figure 5.3. This workflow resulted in a structurally optimised trained ANN that could be used for the explicit and implicit modelling tests.

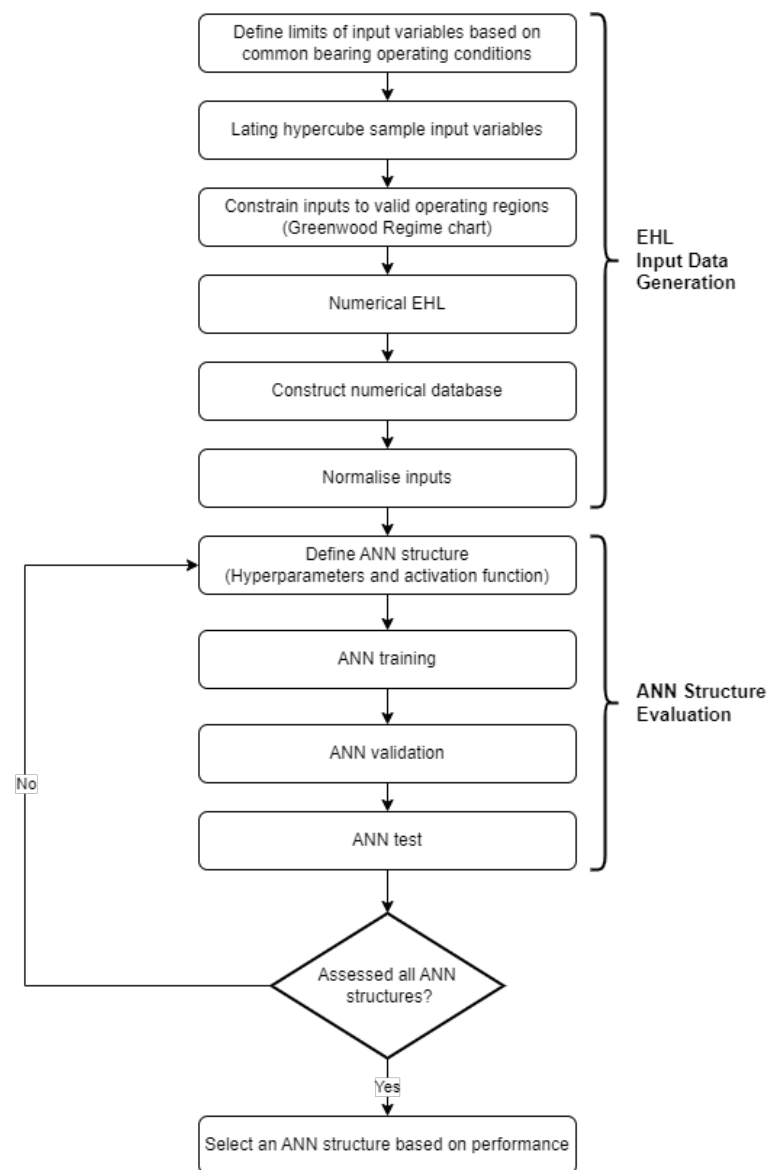


Figure 5.3 ANN data flow, models and training flowchart

5.4.1 EHL Input Data Generation

Training an ANN requires an often comprehensive data set. For this study, the training data was generated using the numerical EHL model presented in 3.3. This approach was selected due to the large size of the dataset required for training, and the relatively low resource-intensive nature to generate this. It is important to note that the training data could also be obtained from experimental work, which would further enhance the applicability of this approach for future studies.

Sampling Input Variables

Due to the large design space covered by the high number and range of input parameters, a robust sampling technique must be chosen to create the training data set. In traditional random sampling, each of the parameters is randomly sampled within its defined range. This may lead to insufficient coverage of the parameter space and simple bias, as it lacks a systematic approach to ensure even distribution [144].

The Latin Hypercube Sampling (LHS) method was utilised by Marian et al. [92], and was chosen for this study. It is a statistical method used to efficiently sample a high-dimensional parameter space, such as that required for the central film thickness calculation. LHS is derived from Latin Hypercube Design (LHD), where each parameter's range is divided into equal intervals along each dimension. Each interval is then randomly assigned to a unique position within its corresponding dimension. The process results in a matrix, where each row represents a combination of parameter values. Contrary to the random sampling method, LHS ensures that each interval is sampled exactly once per dimension, preventing clustering and improving representation across the space [144]. This ensures lower computational effort required for ANN training, despite the high number of input variables and value ranges.

The LHD is a $n_s \times n_f$ matrix, where n_s and n_f represent the number of simulations the number of factors respectively. LHS enhances LHD by introducing a randomization component. The randomly selected samples within each interval undergo permutation, ensuring that samples are not biased by the order of selection.

LHS elements are generated by subtracting a random number between zero and one $Z_r \in [0, 1]$ from each LHD element $x_{ij,LHD}$. This is then divided by the number of test points [145]:

$$x_{ij,LHS} = \frac{x_{ij,LHD} - Z_r}{n_s} \quad (5.2)$$

This equation rescales the LHD values to a range between 0 and 1. By subtracting a random number between 0 and 1 and dividing by the total number of sample points, the

resulting Latin hypercube samples are spread evenly across the interval (0,1) for each parameter. This is important, because it allows the Latin hypercube samples to be easily transformed to any desired range or distribution. This transformation to the design space is done using the limits of the tribological parameters in Table 5.2.

The quality of the test field (freedom of correlation and uniform distribution) can be assessed based on the distances between data points [146]. The MaxiMin criterion in the MATLAB® Statistics and Machine Learning toolbox was used to optimise the LHS. This maximises the the minimum distance between individual test points such that the LHS test field is uniformly distributed:

$$\text{MaxiMin} = \left[\sum_{1 \leq i < j \leq n_1} d(x_i, x_j)^{-\xi} \right]^{-\frac{1}{\xi}} \quad (5.3)$$

where d represents all distances in the test field, and subscripts i and j are indexes for the parameter and sample point respectively. ξ represents the application dependant factor which determines the degree of importance assigned to the distances [145].

Constraining the Input Data Bounds

The performance of ANNs is heavily reliant upon the quality of the data set provided for training. To construct a training database, Marian et al. [92] utilised a Finite Element Method (FEM) solver for film thickness calculations. The database covered a very large range of lubricant and material properties for relatively low entrainment speed conditions ($< 0.4 \text{ m/s}$ for the 2D line contact studies). Contact conditions for some combinations of these input parameters exceed realistic conditions within common machine elements, including bearings. To further improve upon this methodology, the input data range required constraining.

The Greenwood Regime chart [147] was used for this purpose. The regions of the chart, as shown in Figure 5.4, are:

- Isoviscous Rigid (IR)
- Isoviscous Elastic (IE)
- Piezoviscous Rigid (PR)
- Piezoviscous Elastic (PE)

The bounds indicate the transition between the lubrication regimes, which are classified based on material, rheological and geometric properties. To find which

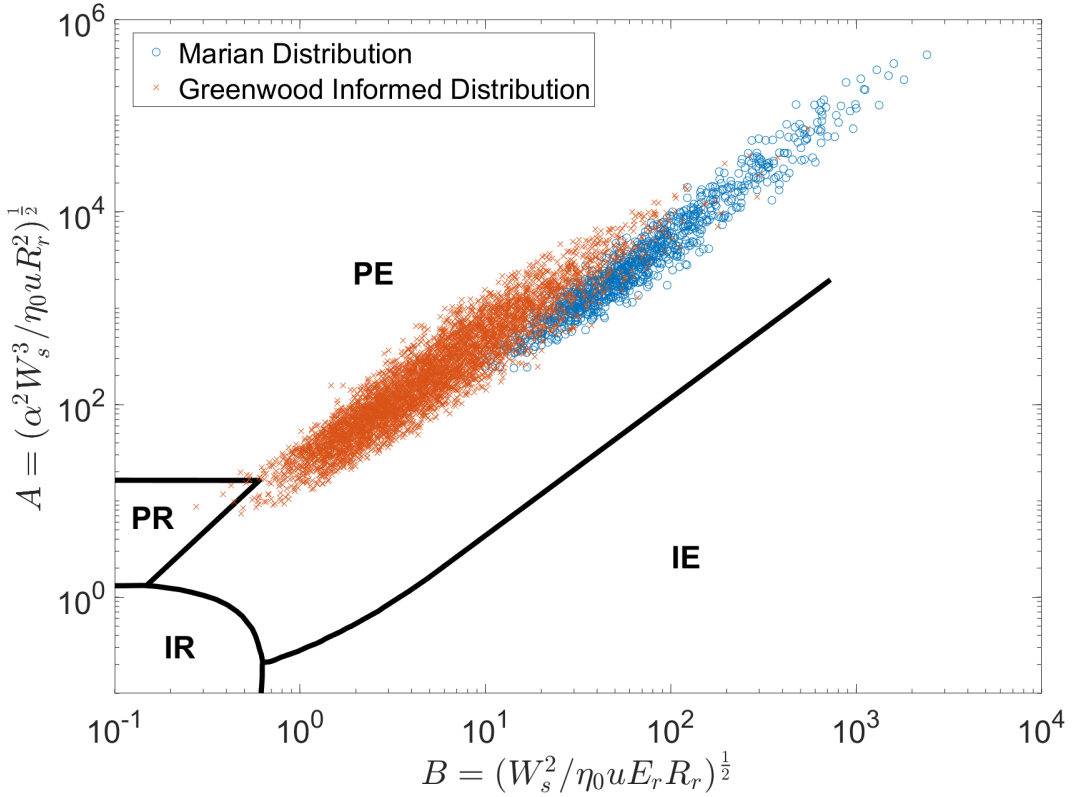


Figure 5.4 Greenwood informed training data vs Marian et al. [92].

regime a contact is operating within, the dimensionless elasticity (G_e) and viscosity (G_v) parameters can be calculated:

$$G_e = \left(\frac{\alpha^2 W_i^3}{\eta_0 u R_r^2} \right)^{1/2} \quad (5.4)$$

$$G_v = \left(\frac{W_i^2}{\eta_0 u E_r R_r} \right)^{1/2} \quad (5.5)$$

The PE region signifies an EHL contact, where pressures are high enough to elastically deform the material and increase the viscosity of the lubricant. The IR region relates to the hydrodynamic regime of lubrication, where the contact load does not deform the surface and viscosity remains constant. Since these investigations are focussed on improving the EHL film thickness estimation, the training data set was required to fall within the PE region of the Greenwood plot.

The initial range of each parameter is shown in Table 5.1. A training data set was then generated using these limits. The input data was then constrained further to ensure Hertzian pressures, P , were between 300 MPa and 3.5 GPa, as well as redistributing any

Table 5.1 Range of ANN film thickness calculation parameters

Parameter	Unit	Minimum	Maximum
Load	N	150	5000
Entrainment Velocity	m/s	0.6	30
Reduced Radius	m	0.0001	0.02
Reduced Elastic Modulus	GPa	200	250
Pressure-Viscosity Coefficient	GPa^{-1}	10	30
Lubricant Viscosity	$Pa.s$	0.0005	0.1
Lubricant Density	kg/m^3	7750	8050
Poisson's Ratio	—	0.3	0.35
Contact Length	m	0.001	0.050

points that fell outside of the PE and PR regions. A flowchart to explain the process of constraining the input variables is shown in Figure 5.5.

A comparison of an the unconstrained and constrained input variables used for the training data is shown in Figure 5.6. It is shown that for the same number of data points (5 000), the constrained data cloud is concentrated over a smaller region of the chart. This improved the point density in regions of interest, increasing the likelihood that the training data more closely matches the test data.

Constructing the Numerical Database

The 1D EHL model presented in Section 3.3 was used to generate the numerical database for training the ANN. The variables corresponding to each constrained data point in Figure 5.6 were used as inputs to the calculation. The target output of central film thickness was calculated.

5.4.2 ANN Structure Evaluation

The general structure of the ANN is described in the following format, as per [80]:

$$N_{in} - [N_{h1} - N_{h2} - N_{h3}]_t - N_{out} \quad (5.6)$$

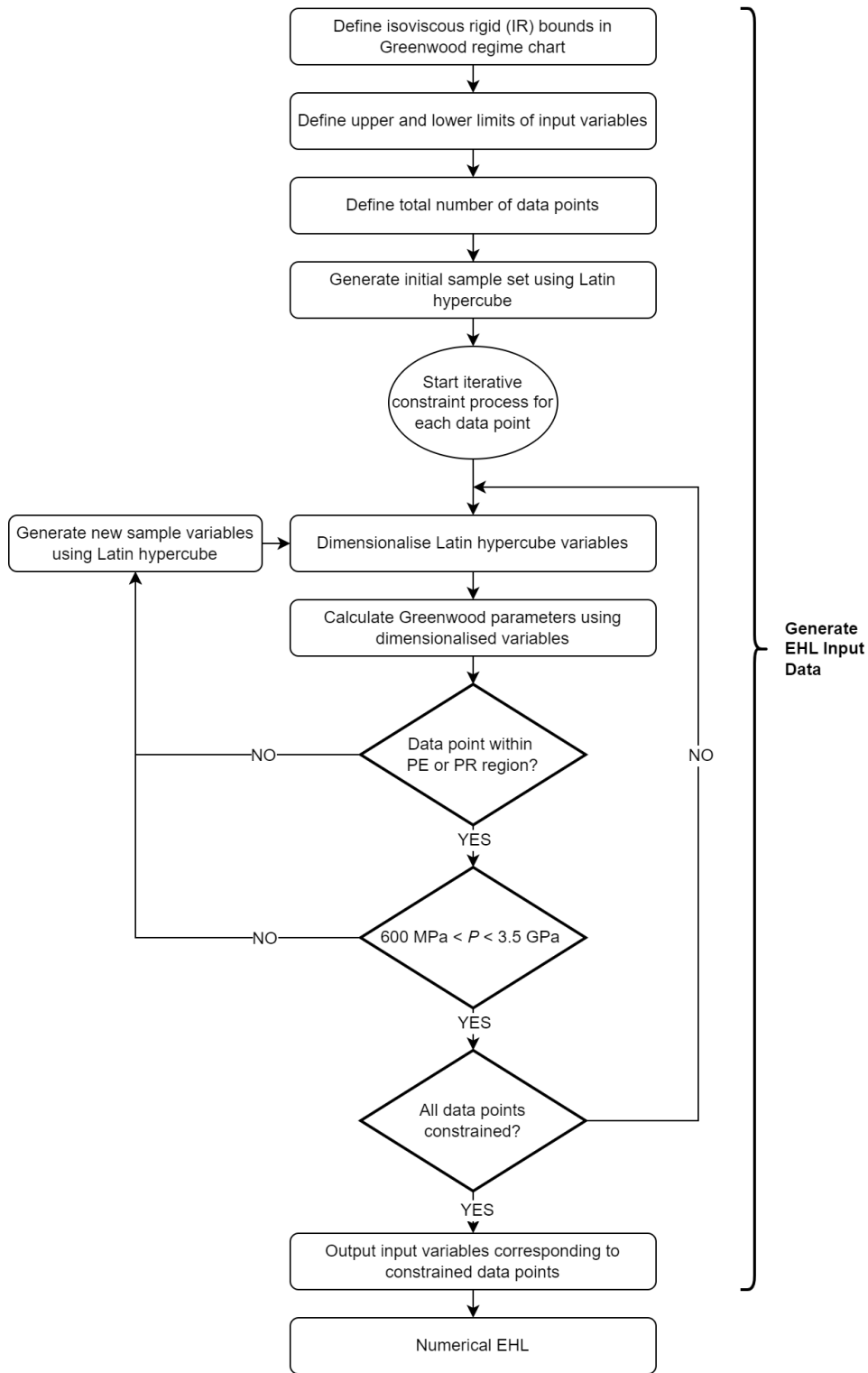


Figure 5.5 Workflow to constrain training input data using Greenwood regimes

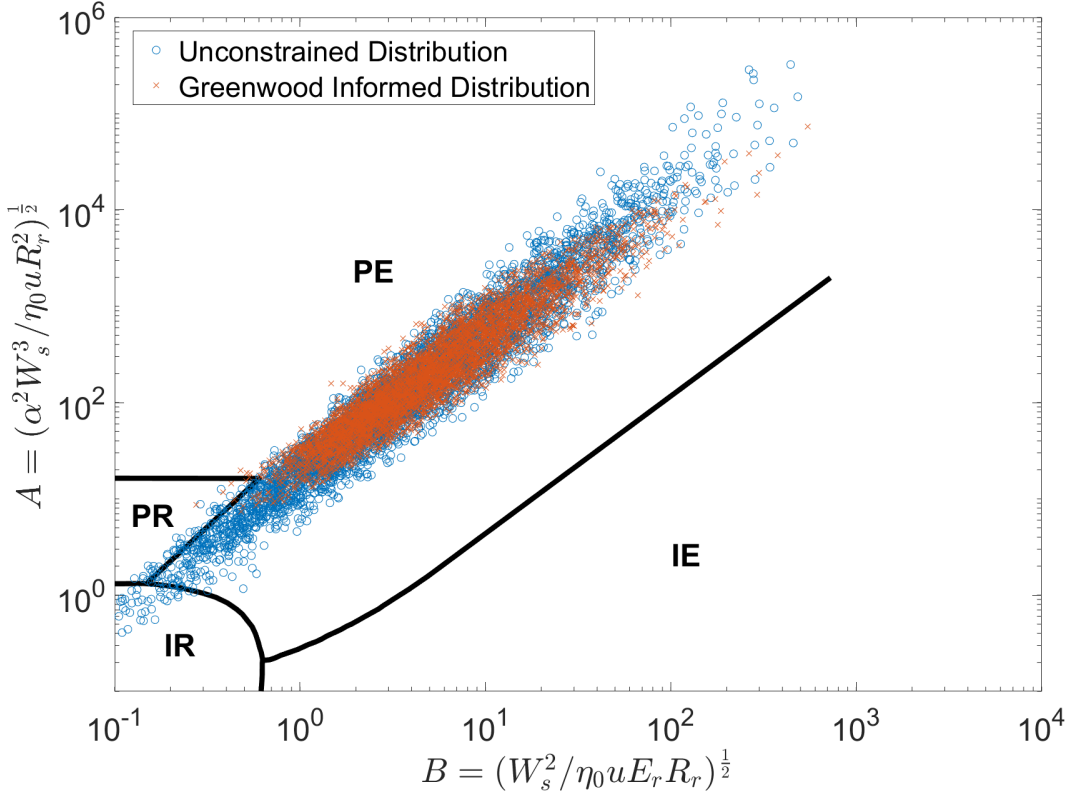


Figure 5.6 Greenwood informed training data vs unconstrained data.

The number of neurons in each layer is denoted by N , with the input and output layers indicated by the subscripts *in* and *out*, respectively. Subscripts $h1$, $h2$, and $h3$ denote the hidden layers, with t being the total number of hidden layers. A graphic representation of the structure used for the film thickness estimations is show in Figure 5.7. As the structural complexity of ANNs increases, the training time increases due to the greater number of neurons and layers. Implementations of ANN in the field of tribology, specifically film thickness predictions, are typically limited to between one and three hidden layers [139].

The structure of an ANN affects both its training time and prediction accuracy. To evaluate the performance of different ANN structures, and hence select an appropriate structure for this application, a sensitivity study was performed. The study comprised of over 500 different ANN structures. The input data range remained constant across all structures, while the variables listed in Table 5.2 were adjusted. This involved varying the hyperparameters: the number of hidden layers varied from one to four, and the number of neurons from 10 to 20. Three activation functions: Hyperbolic tangent, Logistic sigmoid and Rectilinear were evaluated. The wall time for each training data point generation was recorded, as well as the total training time of each ANN structure.

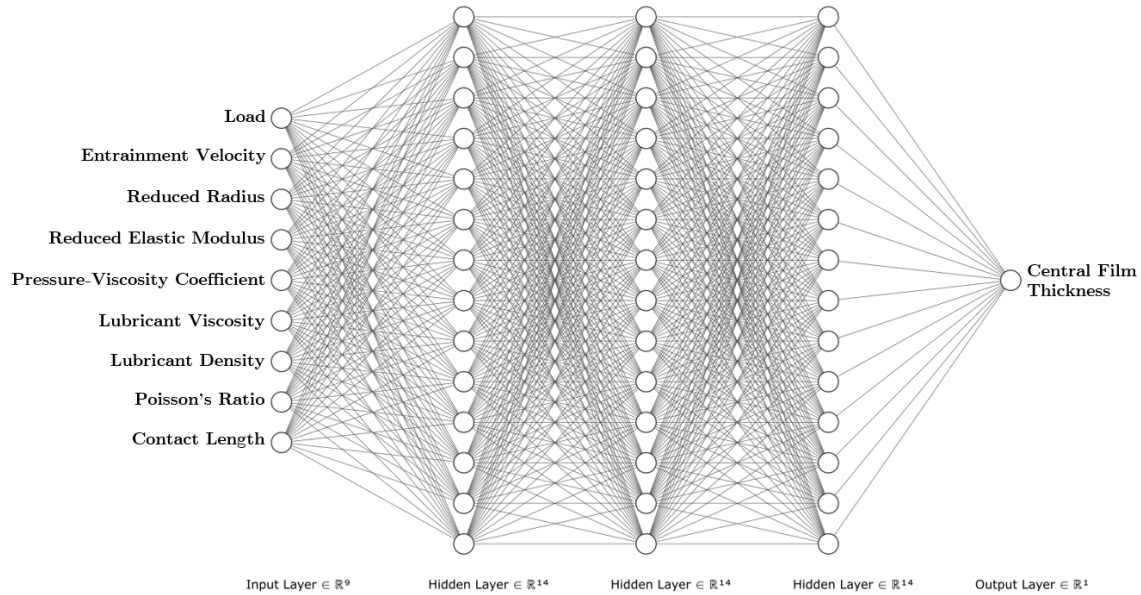


Figure 5.7 ANN structure to predict EHL central film thickness (9 – [14 – 14 – 14]3 – 1)

Table 5.2 Sensitivity study of ANN structure

Variable	Value
Number of training data points	600 - 1500
Number of hidden layers, t	1 - 4
Number of neurons, N	10 - 20
Activation function type	Hyperbolic tangent (Tanh), Logistic sigmoid (LogSig), Rectilinear (ReLU)

Selection of the final structure to be used for film thickness estimation in the bearing models was based on total training time, coefficient of determination (R^2), and the potential for the ANN to overfit. R^2 (Equation 5.12) was evaluated for the test data sets, since this gives an accurate indication of the networks ability to predict film thickness with unseen input variables.

The following sections describe the evaluation process of each network structure.

Training, Validation and Test Datasets

The dataset was first divided into three sets: the training set, the validation set, and the test set, each containing 70 %, 15 % and 15 % of the training data respectively:

1. **Training Set:** The training set is the portion of the dataset used to train the ANN, containing the input data and the corresponding output data. As aforementioned, the ANN adjusts the internal parameters based on this data to learn the underlying patterns.
2. **Validation Set:** The validation set is used to tune the performance of the ANN during the training process. It is an independent dataset that the network has not seen before, allowing for the evaluation of its generalization capabilities. The network's performance on the validation set is monitored during training to make decisions on adjusting hyperparameters (number of hidden layers, neurons per hidden layer, activation functions), or stopping the training process to prevent overfitting.
3. **Test Set:** The test set is a completely independent dataset that is not used during training or validation. It is used to assess the final performance and generalization ability of the trained ANN. By evaluating the network on unseen data, the test set provides an unbiased estimate of the model's performance in actual use.

For this sensitivity study, the size of the training data set was varied (600, 1000, 2000 and 5000) to observe its effect on the quality of the predictions. A limit of 1000 epochs was also implemented, restricting the ANN to 1000 full iterations through the entire training set. This was found to be sufficient to improve accuracy while preventing overfitting.

Data Normalization

The input and target parameters were normalized using the min-max normalisation function:

$$\tilde{x} = \frac{x - x_{\min}}{x_{\max} - x_{\min}}(u - l) + u \quad (5.7)$$

where u , and l represent the upper and lower normalized unit values of 1 and -1 respectively. The dimensional target input value is denoted by x , and the final normalised input or output parameter of the ANN is denoted by \tilde{x} . x_{\max} and x_{\min} are retained to dimensionalise the output variable after the prediction.

Activation Functions

As suggested in [92], four suitable activation functions for the hidden layers were selected for testing. These are mathematical functions that are applied to the output of

each neuron in a layer of the neural network. They introduce non-linearity which allows the network to learn complex input-output relationships. Activation functions help determine the output of a neuron based on the weighted sum of its inputs. A description of each function is provided below:

- **Sigmoid (logistic):** This function transforms the input values into a range between 0 and 1. It has continuously differentiable smooth S-shaped curve and is given by the following formula [141]:

$$\text{log sig}(x) = \frac{1}{1 + e^{-x}} \quad (5.8)$$

Sigmoid functions may suffer from the "vanishing gradient" problem where the partial derivative reaches zero [142], leading to slower convergence during training.

- **ReLU (Rectified Linear Unit):** This function outputs the input value directly if it is positive, and zero otherwise. The mathematical definition is:

$$\text{ReLU} = \begin{cases} x, & x \geq 0 \\ 0, & x \leq 0 \end{cases} \quad (5.9)$$

The gradient is 1 when the neuron is activated, and zero when it is deactivated. This function is computationally efficient and addresses the vanishing gradient problem to an extent [142].

- **Tanh (Hyperbolic Tangent):** The hyperbolic tangent or tanh function is defined as:

$$\tanh(x) = \frac{2}{1 + e^{-2x}} - 1 \quad (5.10)$$

The formulation and behaviour is very similar to sigmoid. It produces values which range from -1 to 1, having a centred mean around zero.

- **Linear:** A simple linear activation was used on the output.

Evaluating the Network Performance

During backpropagation of the ANN, the Mean Squared Error (MSE) was used to evaluate the network's performance:

$$MSE = \frac{1}{N} \sum_{i=1}^N (t_i - y_i)^2 \quad (5.11)$$

where t_i and y_i are the target and predicted value respectively. The total number of training points being trained, validated or tested is denoted by N .

To assess the goodness of fit of the ANN, the statistical metric R^2 , known as the coefficient of determination, was used. This measures the proportion of variance in the dependant variable (film thickness) that is predictable from the input variables (Table 5.1) in the model. This value ranges from 0 to 1, with a higher value indicating the best fit of the model to the data. This was post-processed after training and is calculated as follows:

$$R^2 = 1 - \frac{\sum_{i=1}^N (t_i - y_i)^2}{\sum_{i=1}^N (y_i - \bar{y})^2} \quad (5.12)$$

where \bar{y} is the mean of the target sample. The numerator of the fraction, $\sum_{i=1}^N (t_i - y_i)^2$, represents the sum of squared residuals, which quantifies the variation in the target variable that is not explained by the model. The denominator, $\sum_{i=1}^N (y_i - \bar{y})^2$, is the total sum of squares, which captures the total variation in the target variable [92].

Preventing Overfitting

Early stopping and regularisation was used to prevent statistical overfitting during training [143]. Early stopping halts the training process before the model reaches the maximum number of epochs. This is done by monitoring the performance (MSE (Equation 5.11)) of the network against the validation set during training. Once the performance reaches a plateau, or begins to degrade, the training is stopped early. Regularisation adds additional constraints to the learning process. It modifies the performance criteria by accounting for the change in mean square of the network weights and biases (Mean Squared Weight (MSW)). This is calculated in Eq. 5.13:

$$MSW = \frac{1}{N} \sum_{j=1}^N w_j^2 \quad (5.13)$$

where w_j is the individual weight value associated with the j -th neuron or connection in the network.

By applying an adjustment factor, denoted as γ' , the weights and biases can be reduced during propagation (Eq. 5.14), thus mitigating the risk of overfitting and improving the network's generalization capability.

Table 5.3 Roller Bearing Parameters

Parameter	Value
Inner race diameter	31.5 mm
Roller diameter	7.5 mm
Roller length	15 mm
Number of rollers	12
Radial interference	5 μm
Young's modulus	218 GPa
Poisson's ratio	0.33

Table 5.4 Operating Conditions

Parameter	Value
Radial force	6000 N
Rotational velocity	10 000 rpm

$$MSE_{reg} = \gamma' * MSW + (1 - \gamma') * MSE \quad (5.14)$$

5.4.3 Explicit Bearing Film Thickness Predictions

After identifying a suitable training data size and structure, an ANN was trained to estimate the EHL central film thickness. These results could then be compared to the analytical (Equation 4.11) and numerical (Section 3.3) methods for calculating the film thickness under realistic bearing operating conditions.

The FMBD model used in Chapter 4 was used for this study. The shaft was modelled as a rigid body, and loading in the radial direction was purely static to remove the influence of additional dynamic effects. The shaft was constrained to one rotational and two lateral degrees of freedom. Bearing properties and operating conditions are shown in Table 5.3 and Table 5.4 respectively.

The bearing was modelled as dry, without the influence of the EHL film at the roller-race contacts. The kinematic and dynamic results necessary for the film thickness estimation were extracted from an individual roller at each time step of the simulation.

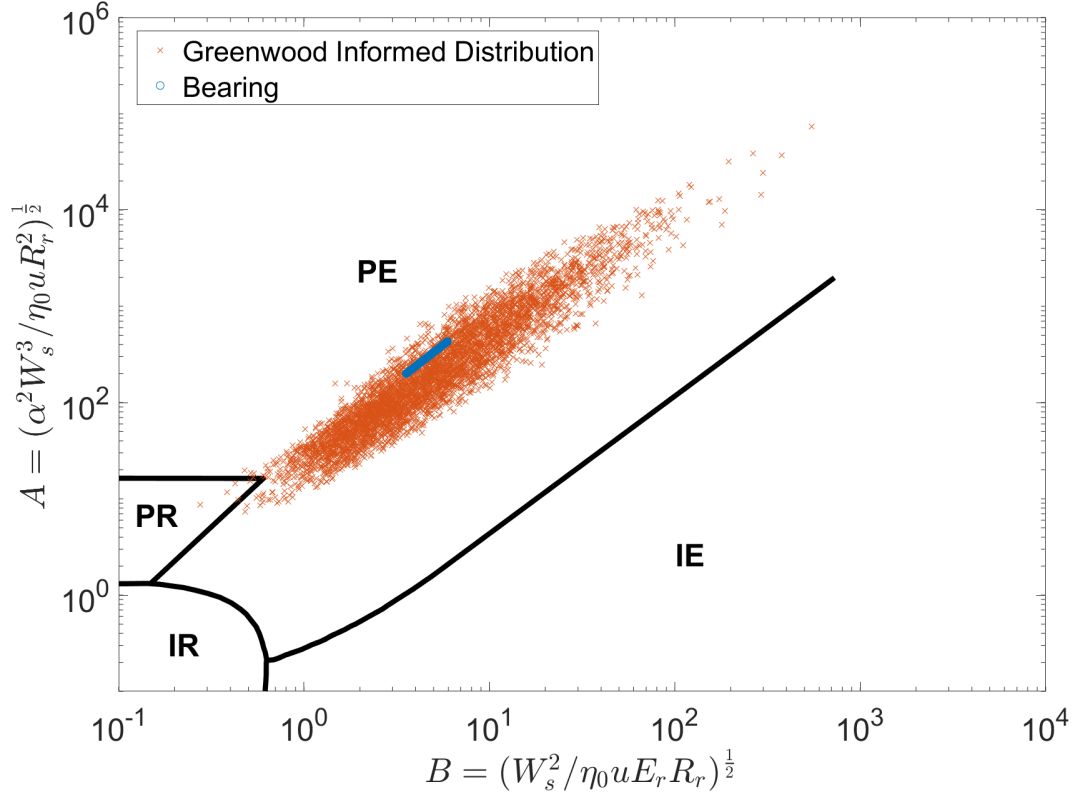


Figure 5.8 Bearing operating conditions vs Greenwood informed training data.

These results include roller load, contact entrainment velocity, and reduced radius of the contact between the roller and inner-race.

The loading pattern is cyclic in nature as the roller enters and exits the most highly loaded region of the bearing, corresponding to the radial force vector applied to the inner race. Sufficient preload ensures constant contact between elements and raceways so that the regime does not deviate from EHL. The contact reduced radius (3.03 mm) and entrainment speed (15.7 m/s) do not change throughout the orbit as they are a function of bearing geometry and constant operating speed. The normal contact load fluctuation is shown in Figure 5.9.

The operating conditions of the bearing were within the range of validity of the training data set. This is demonstrated in Figure 5.8 whereby the Greenwood parameters for the bearing operating points are calculated and overlayed on the training data cloud.

The structure chosen for this study was based on the conclusions drawn in Section 5.5.1. A structure of 3 hidden layers with 14 neurons per layer was selected ($9 - [14 - 14 - 14]_3 - 1$). Logistic sigmoid was selected as the activation function for the hidden layers. This structure is represented graphically in Figure 5.7.

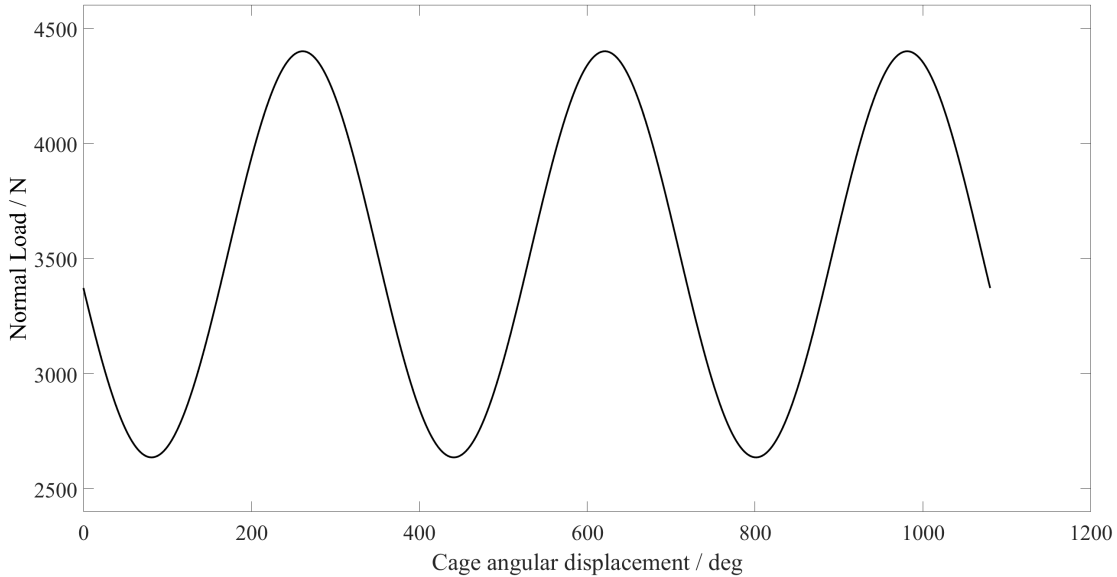


Figure 5.9 Normal contact load vs cage angular displacement

5.4.4 Implicit Bearing Film Thickness Predictions

Same model as in Section 4.3, but with ANN instead of the analytical formulae. TODO.

5.5 Results and Discussion

The following data was obtained using consumer grade hardware with the following specifications: Intel® Core™ i7-9750H CPU 6 cores @ 2.60GHz, 32GB RAM; GPU: NVIDIA GeForce GTX 1650. identical hardware was used for both the full numerical and the ANN solutions to provide performance comparisons and assess the suitability of ANNs for film thickness calculations in FMBD solvers.

5.5.1 ANN Structure Evaluation

The 1D EHL model presented in Section 3.3 was used to generate the numerical database for training the ANN. Each numerical solution and hence training point took an average of 5.88 s to compute. The construction of the entire database on a single core therefore has a wall time of between 58.8 min and 489 min for 600 and 5000 points respectively. This wall time is noted for baseline comparisons, and can be significantly improved if parallelisation across multiple cores is utilised.

Tables 5.5 - 5.7 present the R^2 values obtained from 600 training data points, considering different activation functions described in Section 5.4.2. The number of layers and neurons was varied for each activation function. Among the activation functions

Table 5.5 R^2 performance of ANN structures using 600 data points and a LogSig activation function

Activation Function: LogSig												Key $R^2 [-]$	
R^2		Number of Neurons											
		10	11	12	13	14	15	16	17	18	19	20	
Number of Layers	1	0.997	0.995	0.998	0.998	0.999	0.999	0.999	0.998	0.998	0.995	0.999	0.990
	2	0.999	0.999	0.999	0.997	1.000	0.996	0.998	0.998	0.997	0.997	0.995	0.993
	3	1.000	0.998	0.998	0.999	0.997	0.997	0.997	0.998	0.993	0.995	0.996	0.997
	4	0.997	0.999	0.997	0.997	0.999	0.998	0.993	0.989	0.989	0.975	0.990	1.000

tested, the rectilinear (ReLU) function consistently underperformed when compared to the logistic sigmoid (LogSig) and hyperbolic tangent (Tanh) functions across all network structures. Similar to the work of Marian et al. [139], the optimum layers was found to be between two and three, however the activation function was shown to be the dominating determinate of R^2 performance.

The LogSig activation function demonstrated the best R^2 performance, even for lower complexity structures. This was therefore selected for each hidden layer to assess the influence of training data quantity R^2 performance. Tables 5.8 - 5.11 present the training times for networks with varying numbers of training points and structural configurations. The results indicate that training time increases with the number of layers and neurons in the network. However, training time exhibits a much stronger positive correlation with the number of data points rather than with the complexity of the network structure.

Figure 5.10 illustrates the influence of the number of training points on the R^2 value when using the LogSig activation function. The results indicate that 600 data points are sufficient to train an ANN to the accuracy required for the central film thickness prediction ($R^2 = 0.99791$). Increasing the dataset to 5 000 data points resulted in an R^2 value of 1, however this came with significant time cost for structures with higher complexity; reaching 600 s for 4 layers of 20 neurons and a total of 1000 epochs. Combined with a data generation time of 489 min, this represents a computationally inefficient trade-off between accuracy and training cost. It is therefore concluded that 1000 - 2000 training data points are sufficient to achieve accurately trained neural networks for predicting the central film thickness while maintaining computational efficiency.

The results of this study guided the decision for the network structure to be used for the bearing models. A structure of 3 hidden layers with 14 neurons per layer was selected ($9 - [14 - 14 - 14]_3 - 1$). Logistic sigmoid was selected as the activation function for the hidden layers. This was trained using 2000 data points.

Table 5.6 R^2 performance of ANN structures using 600 data points and a Tanh activation function

Activation Function: Tanh												Key $R^2 [-]$	
R^2		Number of Neurons											
		10	11	12	13	14	15	16	17	18	19	20	
Number of Layers	1	0.998	0.999	0.995	0.998	0.998	0.994	0.998	0.999	0.998	0.998	0.998	0.99
	2	0.999	0.998	0.998	0.999	0.996	0.998	0.996	0.996	0.996	0.993	0.994	0.993
	3	0.999	0.992	0.996	0.995	0.992	0.989	0.989	0.985	0.994	0.970	0.984	0.997
	4	0.997	0.997	0.992	0.994	0.991	0.983	0.982	0.978	0.990	0.989	0.983	1.000

Table 5.7 R^2 performance of ANN structures using 600 data points and a Tanh activation function

Activation Function: ReLU												Key $R^2 [-]$	
R^2		Number of Neurons											
		10	11	12	13	14	15	16	17	18	19	20	
Number of Layers	1	0.985	0.991	0.994	0.993	0.993	0.994	0.992	0.994	0.995	0.987	0.990	0.990
	2	0.993	0.996	0.995	0.993	0.992	0.984	0.989	0.993	0.992	0.993	0.992	0.992
	3	0.986	0.983	0.996	0.988	0.984	0.980	0.992	0.992	0.988	0.986	0.988	0.988
	4	0.981	0.990	0.975	0.928	0.951	0.986	0.985	0.986	0.986	0.982	0.985	0.985

Table 5.8 Training time of ANN structures with LogSig activation function and 600 data points

600 Data Points, Activation Function: LogSig												Key Time [s]	
Training Time [s]		Number of Neurons											
		10	11	12	13	14	15	16	17	18	19	20	
Number of Layers	1	0.76	0.96	1.16	1.01	1.49	1.30	1.41	1.72	1.12	0.90	1.13	0.00
	2	1.01	2.93	1.94	1.43	1.88	1.80	1.56	1.80	1.33	2.51	1.77	10.00
	3	2.81	1.29	2.58	2.22	2.27	1.52	1.67	2.26	2.06	1.94	3.57	100.00
	4	1.64	5.97	2.21	2.79	6.70	2.66	4.36	2.51	2.76	2.61	2.90	600.00

Table 5.9 Training time of ANN structures with LogSig activation function and 1000 data points

1000 Data Points, Activation Function: LogSig												Key Time [s]	
Training Time [s]		Number of Neurons											
		10	11	12	13	14	15	16	17	18	19	20	
Number of Layers	1	1.00	1.10	1.36	1.11	1.89	2.20	2.09	1.01	1.58	2.83	1.10	0.00
	2	3.25	1.66	2.33	2.72	4.00	3.07	2.35	2.81	5.35	1.97	3.77	10.00
	3	2.74	6.35	4.76	5.58	4.17	2.36	4.88	7.56	7.18	6.55	5.18	100.00
	4	2.59	2.29	8.12	6.47	7.17	3.81	7.70	11.46	19.01	12.14	8.92	600.00

Table 5.10 Training time of ANN structures with LogSig activation function and 2000 data points

2000 Data Points, Activation Function: LogSig												Key Time [s]	
Training Time [s]		Number of Neurons											
		10	11	12	13	14	15	16	17	18	19	20	
Number of Layers	1	0.90	2.47	1.70	1.74	4.38	2.61	2.49	1.81	4.54	2.58	2.67	0.00
	2	6.06	7.19	10.66	13.38	6.20	6.54	6.76	14.61	16.32	7.86	20.32	10.00
	3	18.72	13.45	4.55	5.19	21.54	23.88	26.00	25.44	27.50	11.66	19.71	100.00
	4	11.49	18.79	16.06	6.69	41.55	30.72	28.04	67.86	14.78	62.17	57.13	600.00

Table 5.11 Training time of ANN structures with LogSig activation function and 5000 data points

5000 Data Points, Activation Function: LogSig												Key Time [s]	
Training Time [s]		Number of Neurons										Time [s]	
		10	11	12	13	14	15	16	17	18	19	20	
Number of Layers	1	1.74	4.06	3.12	3.24	3.82	3.78	2.11	11.73	3.45	14.25	12.07	0.00
	2	10.86	22.86	37.50	30.99	20.02	19.95	38.09	11.02	48.89	134.95	37.88	10.00
	3	14.53	33.38	34.62	116.81	61.86	57.12	140.49	124.75	228.28	71.22	85.55	100.00
	4	94.66	36.71	139.61	70.20	13.33	229.45	88.24	155.37	217.48	500.54	600.01	600.00

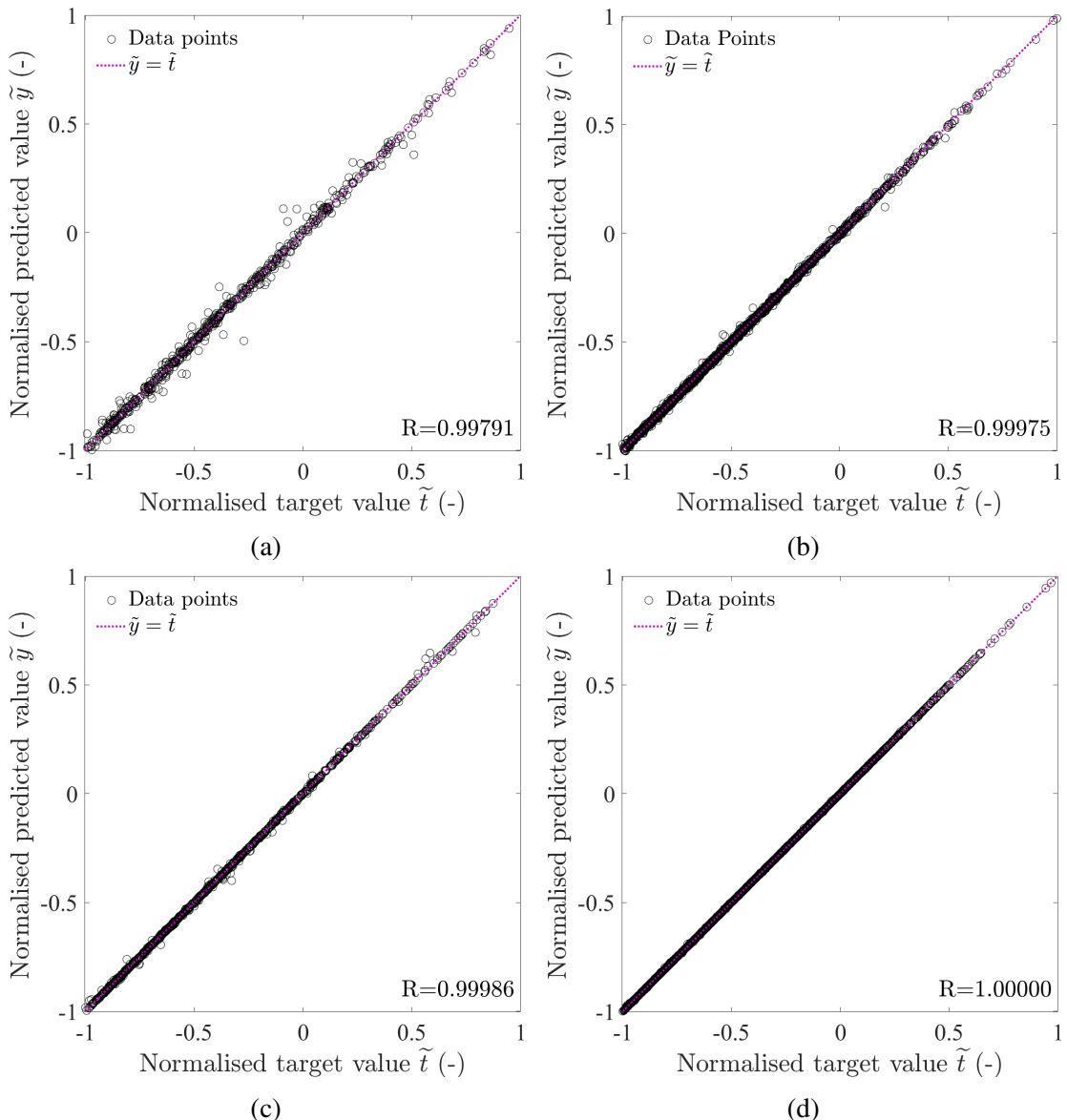


Figure 5.10 R^2 performance of ANN structure ($N=14$, $t=3$) using a Logistic Sigmoid activation function at each hidden layer: a) 600 points, b) 1000 points, c) 2000 points, d) 5000 points

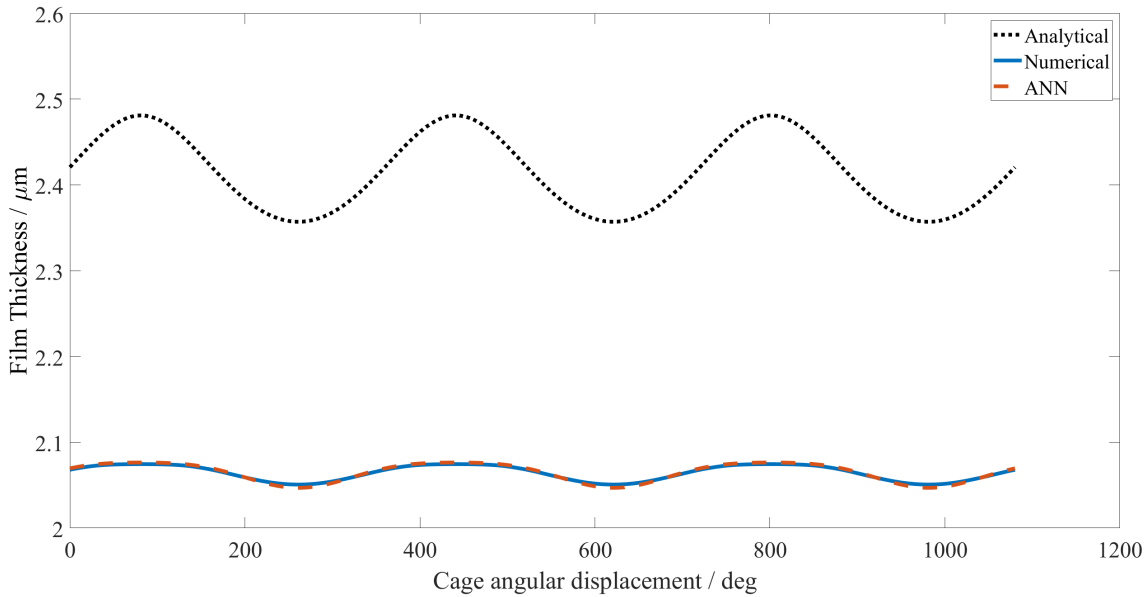


Figure 5.11 ANN, numerical and analytical central film thickness comparisons.

5.5.2 Explicit Bearing Film Thickness Predictions

The performance of the selected ANN was compared to the computed numerical and analytical results during several operating cycles of the bearing model presented in Section 5.4.3.

Figure 5.11 demonstrates that the ANN prediction of film thickness (orange) matches very closely with the numerical calculation (blue). The fluctuations arise due to the varying contact load, with a peak of $2.076 \mu\text{m}$ and $2.074 \mu\text{m}$ for the ANN and numerical model respectively. By comparison, the analytical equation overestimates the peak film thickness to be $2.481 \mu\text{m}$.

Table 5.12 demonstrates the relative performance of the ANN for both computation time and MSE for the analysis in Figure 5.11. The ANN demonstrates a ~ 1500 factor computation time reduction in comparison with the ANN, whilst maintaining excellent accuracy as shown by the MSE. The analytical solution is a factor of ~ 75 faster than the ANN, but is significantly less accurate. As discussed in Section 5.2, this will increase with entrainment velocity and complexity of modelling requirements.

The ANN film thickness prediction also shows excellent agreement across the speed range from 1 000 - 21 000 rpm . Figure 5.12 demonstrates the accuracy of the ANN prediction, with an MSE of $3.18 \times 10^{-4} \mu\text{m}^2$ across the speed range. This proves the effectiveness of this solution across a broad operating range.

Table 5.12 Film thickness computation methodology performance relative to the numerical solution

Method	Time per point	MSE
	[s]	[μm^2]
Numerical	4.87E + 00	-
Analytical	4.43E - 05	1.24E - 01
ANN	3.10E - 03	3.89E - 06

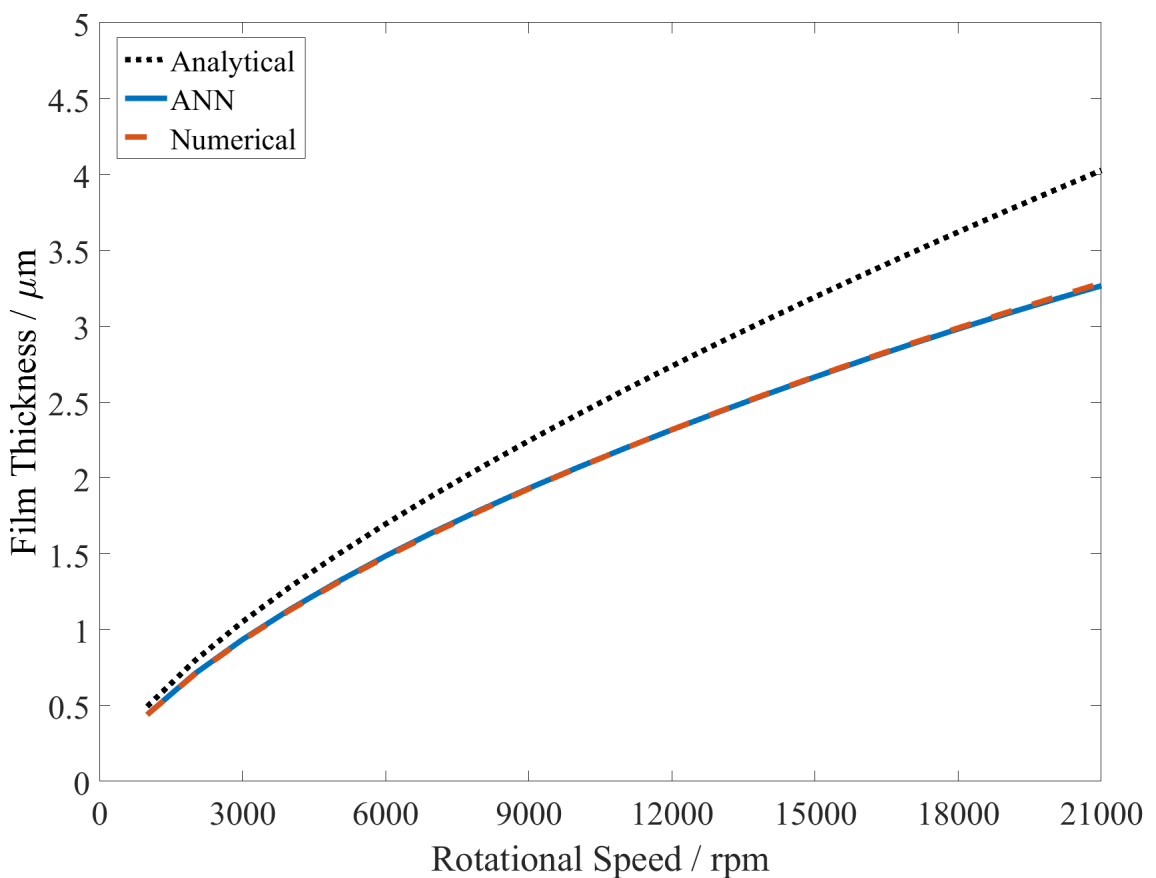


Figure 5.12 Central film thickness - EHL vs ANN vs analytical speed sweep. thickness comparisons at increasing rotational speeds

5.6 Conclusions

A tribological ANN has been trained and employed to calculate the central EHL film thickness at a roller-race conjunction. Different ANN structures were evaluated to find the optimum structure for the film thickness estimation. Numerically generated training data was sampled using Latin Hypercube Sampling (LHS), and constrained to realistic contact conditions using the Greenwood regime. This ensured a high quality dataset; essential for high prediction accuracy. The trained ANN was then used to calculate film thickness in a roller bearing using a simple dynamic bearing model under constant load. The ANN was then employed in an FMBD model, where the film thickness was estimated implicitly at each time step of a dynamic simulation and considered in the prevailing contact mechanics.

1. Each numerical solution to generate a training data point took 5.88 s. The single core wall time for 600 and 5 000 training points was 58.8 min and 489 min respectively. The numerical solution database could benefit from explicit parallelisation ie. use of multiple computational cores of the CPU.
2. 600 training points achieved sufficient coefficient of determination performance ($R^2 = 0.99791$) to accurately predict central film thickness. Whilst 5000 points resulted in an R^2 value of 1, training of the network and effort to generate this quantity of training data rendered it computationally inefficient.
3. An ANN structure with three hidden layers, each containing 14 neurons and using a logistic sigmoid activation function, was found to be optimal for the operating bounds investigated in this study when trained on 2,000 data points.
4. The analytical equations increasingly deviate from the numerical calculation at high entrainment velocities; up to 22.6 % at 21 000 rpm for the bearing examined in this study. At the same speed, the ANN had an error of 1.58 %. Across a speed range from 0 - 21 000 rpm, the MSE of the ANN was $3.18 \times 10^{-4} \mu\text{m}^2$.
5. For the bearing case study presented, the mean squared error (MSE) of the ANN film thickness prediction was $3.89 \times 10^{-6} \mu\text{m}^2$ when benchmarked against the numerical solution for a fluctuating contact load. This is a dramatic improvement over the MSE of the analytical model which was $1.24 \times 10^{-1} \mu\text{m}^2$.
6. The ANN was shown to be ~ 1 500 times faster than the numerical solution with a very small margin of error. The ANN is a factor of ~ 75 times slower than the analytical equation, but a factor of 3×10^4 more accurate when comparing MSE performance against the numerical method.

This study has proven ANNs to be an accurate and computationally efficient method of calculating EHL film thickness. Despite having no physical understanding of the system, this data-driven solution has proved accurate and computationally efficient for the film thickness estimation. This computational efficiency and accuracy lends itself very well to tribological models in FMBD solvers. It must be noted that the ability of the ANN to extrapolate beyond the bounds of the training data set must be addressed. Excessive extrapolation may lead to instability in the dynamic solution. However, by selecting a sufficient design space and robust sampling method such as LHS, this risk can be mitigated.

Roller bearings are only one application of these ANNs. The use cases extend far beyond roller bearings, to key components in automotive, machining and other industrial applications where interactions between contiguous surfaces exist. Many of these machine elements operate within the regions that this ANN was trained to cover, making it a deployable solution across many applications with very little computational training effort.

Chapter 6

Conclusions and Future Works

6.1 Overall Conclusions

This thesis presents investigations into the influence of considering the elastohydrodynamic (EHL) film implicitly at the roller-race conjunction in high-speed rolling element bearings modelling. A coupled tribological and dynamic approach was used to assess how the EHL film affects bearing dynamics at the operating speeds and loads of electrified powertrains.

This work highlights the impact of the lubricant film on bearing dynamics, particularly at high-speeds where the EHL film thickness increases substantially. The film thickness can exceed that of the contact deformation predicted by the dry Hertzian assumption, significantly influencing contact force and stiffness predictions which are underestimated in non-lubricated analyses. The following conclusions have been drawn from the results and analyses contained in this research:

1. Experimental and tribological tests were conducted at speeds of up to 15 000 *rpm*, with a radial load of 750 *N* applied to a shaft-bearing system. The results showed that dry modelling of a roller bearing underestimates the contact load by 149% at 15 000 *rpm*. This discrepancy is attributed to the additional deformation incurred as a result of lubricant entrainment into the EHL contact. The central film thickness increased from 0.1 μm - 1.9 μm for a quasi-dynamic speed sweep from 0 - 15 000 rpm, leading to an increasing difference in contact load between dry and lubricated modelling with speed. However, at higher bearing loads, such as during system resonance, the contact load difference reduces to 21% due to the contact deformation predicted by the dry Hertzian assumption closely matching the magnitude of the film (1.58 μm at 14 134 *rpm*). This therefore concludes that the dominating difference between these modelling techniques occurs at higher

rotational speed and low load. This matches the operating characteristics and magnitudes of electrified transmissions, and hence the consideration of the film at the roller-race conjunction cannot be neglected in their modelling.

2. To assess the impact of this contact load calculation disparity on bearing dynamics, a coupled simulation approach was developed to integrate a lubricated bearing model within a system-level FMBD model. The approach implicitly considers the influence of the EHL film on the bearing contact mechanics at each time step of the dynamic analysis. Quasi-dynamic simulations were performed up to 21 000 *rpm* using loading conditions from a first stage gear pair coupled to a 54 kW permanent magnet synchronous motor (PMSM) with a peak torque of 68 Nm. Results show that the lubricant film increases contact stiffness by up to 24.9 % at 21 000 rpm when compared to conventional dry analyses. This is due to the non-linear force-deflection relationship at the contact. The contribution of the lubricated contact stiffnesses increases the total bearing stiffness by 16.9 %. This total stiffness consequently increases the natural frequency of the system from 3470 Hz to 3542 Hz, corresponding to a 250 rpm increase from the dry estimation at 12 500 rpm. Implicit inclusion of the film in the analysis was therefore shown to affect the predicted NVH response of the system. The increased bearing stiffness also reduced the total radial displacement of the shaft across the entire speed range.
3. At high entrainment velocities of 30.7 m/s, it was shown that the analytical film thickness equations deviate from the numerical solution and underestimate the estimated film thickness by 22.6%. This corresponded to 21 000 rpm in the bearings under investigation. An ANN was trained using a broad value range of tribological input data to predict EHL central film thickness. The training input data was constrained using the Greenwood regimes of lubrication, improving data cloud point density and achieving a coefficient of determination (R^2) of 0.99791 with just 600 data points.
4. In static bearing tests, the central film thickness for entrainment velocities of 1.53 m/s - 30.7 m/s were predicted by the ANN. Unlike the 22.6% over-prediction of the central film using the analytical equations, the ANN under predicted the film by just 1.53% at 21 000 rpm, having a mean squared error (MSE) of just $3.18 \times 10^{-4} \mu\text{m}^2$ across the speed range. Static operating points with time-varying contact loads were also investigated at 10 000 rpm. Across the loading cycle, the ANN achieved an MSE of $3.89 \times 10^{-6} \mu\text{m}^2$ when benchmarked against the

numerical solution for a fluctuating contact load. This is a dramatic improvement over the MSE of the analytical model which was $1.24 \times 10^{-1} \mu\text{m}^2$.

5. The ANN was shown to be ~ 1 500 times faster than the numerical solution with a very small margin of error when tested across 750 data points spanning a large value range of film thickness input variables. The ANN is a factor of ~ 75 times slower than the analytical equation, but a factor of 3×10^4 more accurate when comparing MSE performance of both against the numerical method.
6. The ANN has been embedded within an FMBD system model to calculate EHL film thickness and consider it implicitly in the evaluation of the bearing dynamics. This establishes a workflow that will further enhance contact modelling in FMBD simulations.

6.2 Contributions to Knowledge

The main novelties and contributions to knowledge from this thesis are summarised below:

1. A novel experimental test rig was constructed to measure the kinematic motion of a bearing at rotational speeds and loads up to 750 N and 15 000 rpm respectively. The bearing orbital motion was measured and used for conjunction and component level tribological analysis. The methodology of coupling experimental test with numerical tribological models has not been previously reported in this manner at these speeds. The outcome of this demonstrated the requirement of implicitly modelling the EHL film in future high-speed applications, since it contributed to a 149% contact load increase at 15 000 rpm when compared to conventional dry analyses.
2. A coupled co-simulation approach was established to implicitly consider the EHL film in roller bearings within a high-speed system-level FMBD model. The model replicates the operating conditions of a 54 kW permanent magnet synchronous motor (PMSM) coupled to a first stage gear pair, operating at speeds up to 21 000 rpm. This was the first time in open literature that an implicitly lubricated multi-physics bearing model has been considered in the context of electrified powertrain dynamics. The outcome of this demonstrated that the increased contact deflection, due to the lubricant film inclusion, increases total bearing stiffness by 24.9 % at 21 000 rpm. This effectively behaves as a non-linear, speed dependant radial preload on the bearing. The contribution of this

stiffness increased the natural frequency of the system, and hence affected NVH response. This proves the requirement to consider the EHL film implicitly for rolling element bearing modelling under the high speeds, low load operating conditions of electrified powertrains.

3. An ANN was trained using input data calculated using a 1D numerical EHL model. A wide value range of input variables necessary for the EHL central film thickness calculation were used to train the model. The value range was consistent with common machine element contacts, with its applicability also extending to gear pairs and cam contacts. The novel methodology of constraining the training data using the Greenwood regime ensured high data quality whilst only requiring 600 training data points. The ANN achieved an MSE of $3.89 \times 10^{-6} \mu\text{m}^2$ when benchmarked against the numerical solution, whilst reducing calculation time by a factor of 1 500. This methodology will further contribute to the computational efficiency and accuracy of tribological ANNs.
4. The ANN was embedded within an FMBD system-level model to calculate EHL film thickness and consider it implicitly in the evaluation of the bearing and system dynamics. The film thickness evaluation achieves the accuracy of numerical models without the associated computational limitations. This modelling method of combining component level ANN within a flexible system has not been previously reported.

6.3 Addressing the Research Questions

The primary objective of this work was to investigate the interaction between tribology and dynamics in rolling element bearings, with particular focus on the significance of this multi-physics interaction in high-speed automotive applications. On reviewing the conclusions drawn from this thesis, it can be demonstrated that the research questions presented in Section 1.1 have been addressed.

The findings of this thesis are to be implemented into the commercial software AVL EXCITETM M to support future rolling element bearing development. The influence of the lubricant film in dynamic analysis is of particular interest. The workflow of coupling contact level artificial neural networks into system level FMBD models is also of significance. This approach has applications beyond rolling element bearings, as a generic contact approach could also improve non-conformal contact modelling for gears and cams.

6.4 Future Works

The novel approaches presented in this thesis open up further opportunities to advance this area of research.

- For wider adoption of the ANN solution, the ability to extrapolate beyond the bounds of the training data must be addressed. Extrapolation errors in the film thickness estimation could yield unrealistic film thickness values, introducing potential impulses to the dynamic system. This could affect the stability of an FMBD model and lead to divergence.
- Develop methodology for integrating ANNs into FMBD software. A suggested approach is to train the model using known input variables and kinematic conditions in a first stage static analysis. This trained model could then be called at each time step of the dynamic simulation. Alternatively, a library of trained models could be established using Greenwood regime constraints outlined in this work.
- Expand the training data set for the ANN to include experimental measurements from high-speed mini traction machines.

References

- [1] E. Parliament and of the Council of 19 April 2023, “Regulation (eu) 2023/851,” pp. 1–19, 4 2023.
- [2] W. Cai, X. Wu, M. Zhou, Y. Liang, and Y. Wang, “Review and development of electric motor systems and electric powertrains for new energy vehicles,” *Automotive Innovation*, vol. 4, pp. 3–22, 2021. [Online]. Available: <https://doi.org/10.1007/s42154-021-00139-z>
- [3] T. A. Harris and M. N. Kotzalas, *Essential Concepts of Bearing Technology*, 5th ed. Taylor and Francis Group, 2007.
- [4] R. Stribeck, “Ball bearings for various loads,” *Trans. ASME*, vol. 29, pp. 420–463, 1907.
- [5] G. Lundberg and A. Palmgren, “Dynamic capacity of roller bearings,” *Acta Polytechnica; Mechanical Engineering Series, Royal Swedish Academy of Engineering Sciences*, vol. 2, pp. 96–127, 1952.
- [6] A. Palmgren, *Ball and Roller Bearing Engineering*, 3rd ed. SKF Industries, 1959.
- [7] A. B. Jones, “A general theory for elastically constrained ball and radial roller bearings under arbitrary load and speed conditions,” *Journal of Fluids Engineering, Transactions of the ASME*, vol. 82, pp. 309–320, 1960.
- [8] T. Harris, *Roller Bearing Analysis*, 5th ed. CRC Press, 11 2006.
- [9] H. Sjovall, “The load distribution within ball and roller bearings under given external radial and axial load,” *Teknisk Tidskrift, Mek.*, vol. 9, 1933.
- [10] J. Rumbarger, “Thurst bearings with eccentric loads,” *Mach des.*, pp. 172–179, 1962.

- [11] S. Andréason, “Load distribution in a taper roller bearing arrangement considering misalignment,” *Tribology*, vol. 6, pp. 84–92, 6 1973. [Online]. Available: <https://linkinghub.elsevier.com/retrieve/pii/0041267873902418>
- [12] J. Y. Liu, “Analysis of tapered roller bearings considering high speed and combined loading.” *American Society of Mechanical Engineers*, pp. 564–572, 1976.
- [13] J. M. de Mul, J. M. Vree, and D. A. Maas, “Equilibrium and associated load distribution in ball and roller bearings loaded in five degrees of freedom while neglecting friction—part ii: Application to roller bearings and experimental verification,” *Journal of Tribology*, vol. 111, pp. 149–155, 1 1989. [Online]. Available: <https://asmedigitalcollection.asme.org/tribology/article/111/1/149/432349/Equilibrium-and-Associated-Load-Distribution-in>
- [14] B. R. Jorgensen and Y. C. Shin, “Dynamics of machine tool spindle/bearing systems under thermal growth,” *Journal of Tribology*, vol. 119, pp. 875–882, 1997.
- [15] ——, “Dynamics of spindle-bearing systems at high speeds including cutting load effects,” *Journal of Manufacturing Science and Engineering*, vol. 120, pp. 387–394, 5 1998. [Online]. Available: <https://asmedigitalcollection.asme.org/manufacturingscience/article/120/2/387/434744/Dynamics-of-SpindleBearing-Systems-at-High-Speeds>
- [16] J. M. de Mul, J. M. Vree, and D. A. Maas, “Equilibrium and associated load distribution in ball and roller bearings loaded in five degrees of freedom while neglecting friction—part i: General theory and application to ball bearings,” *Journal of Tribology*, vol. 111, pp. 142–148, 1 1989. [Online]. Available: <https://asmedigitalcollection.asme.org/tribology/article/111/1/142/432329/Equilibrium-and-Associated-Load-Distribution-in>
- [17] J. Sopanen and A. Mikkola, “Dynamic model of a deep-groove ball bearing including localized and distributed defects. part 1: Theory,” *Proceedings of the Institution of Mechanical Engineers, Part K: Journal of Multi-body Dynamics*, vol. 217, pp. 201–211, 9 2003. [Online]. Available: <http://journals.sagepub.com/doi/10.1243/14644190360713551>
- [18] C. T. Walters, “The dynamics of ball bearings,” *Journal of Tribology*, vol. 93, pp. 1–10, 1971.

- [19] L. D. Meyer, F. F. Ahlgren, and B. Weichbrodt, “An analytic model for ball bearing vibrations to predict vibration response to distributed defects,” *Journal of Mechanical Design*, vol. 102, pp. 205–210, 4 1980. [Online]. Available: <https://asmedigitalcollection.asme.org/mechanicaldesign/article/102/2/205/430940/An-Analytic-Model-for-Ball-Bearing-Vibrations-to>
- [20] C. S. Sunnersjö, “Varying compliance vibrations of rolling bearings,” *Journal of Sound and Vibration*, vol. 58, pp. 363–373, 1978.
- [21] M. Matsubara, H. Rahnejat, and R. Gohar, “Computational modelling of precision spindles supported by ball bearings,” *International Journal of Machine Tools and Manufacture*, vol. 28, pp. 429–442, 1988. [Online]. Available: [http://dx.doi.org/10.1016/0890-6955\(88\)90056-9](http://dx.doi.org/10.1016/0890-6955(88)90056-9)
- [22] P. K. Gupta, “Dynamics of rolling-element bearings—part i: Cylindrical roller bearing analysis,” *Journal of Lubrication Technology*, vol. 101, pp. 293–302, 7 1979. [Online]. Available: [https://asmedigitalcollection.asme.org/tribology/article/101/3/293/410262/Dynamics-of-RollingElement-BearingsPart-I](https://asmedigitalcollection.asme.org/tribology/article/101/3/305/410221/Dynamics-of-RollingElement-BearingsPart-IIhttps://asmedigitalcollection.asme.org/tribology/article/101/3/293/410262/Dynamics-of-RollingElement-BearingsPart-I)
- [23] R. Aini, H. Rahnejat, and R. Gohar, “A five degrees of freedom analysis of vibrations in precision spindles,” *International Journal of Machine Tools and Manufacture*, vol. 30, pp. 1–18, 1990.
- [24] H. Rahnejat and S. Rothberg, *Mulit-body dynamics: Monitoring and simulation techniques III*, 1st ed. Wiley, 2004.
- [25] H. Questa, M. Mohammadpour, S. Theodossiades, C. Garner, S. Bewsher, and G. Offner, “Tribo-dynamic analysis of high-speed roller bearings for electrified vehicle powertrains,” *Tribology International*, vol. 154, p. 106675, 2 2021. [Online]. Available: <https://linkinghub.elsevier.com/retrieve/pii/S0301679X20305004>
- [26] B. J. Stone, “The state of the art in the measurement of the stiffness and damping of rolling element bearings,” *CIRP Annals - Manufacturing Technology*, vol. 31, pp. 529–538, 1982.
- [27] P. Dietl, “Damping and stiffness characteristics of rolling element bearings-theory and experiment,” Ph.D. dissertation, 1997.

- [28] L. Bizarre, F. Nonato, and K. Cavalca, “Formulation of five degrees of freedom ball bearing model accounting for the nonlinear stiffness and damping of elastohydrodynamic point contacts,” *Mechanism and Machine Theory*, vol. 124, pp. 179–196, 6 2018. [Online]. Available: <https://linkinghub.elsevier.com/retrieve/pii/S0094114X1830106X>
- [29] H. Rahnejat and R. Gohar, “The vibrations of radial ball bearings,” *Proceedings of the Institution of Mechanical Engineers, Part C: Journal of Mechanical Engineering Science*, vol. 199, pp. 181–193, 1985.
- [30] R. Aini, H. Rahnejat, and R. Gohar, “Vibration modeling of rotating spindles supported by lubricated bearings,” *Journal of Tribology*, vol. 124, pp. 158–165, 2002.
- [31] M. Mohammadpour, P. Johns-Rahnejat, and H. Rahnejat, “Roller bearing dynamics under transient thermal-mixed non-newtonian elastohydrodynamic regime of lubrication,” *Proceedings of the Institution of Mechanical Engineers, Part K: Journal of Multi-body Dynamics*, vol. 229, pp. 407–423, 12 2015. [Online]. Available: <https://doi.org/10.1177/1464419315569621> <http://journals.sagepub.com/doi/10.1177/1464419315569621>
- [32] J. Sopanen and A. Mikkola, “Dynamic model of a deep-groove ball bearing including localized and distributed defects. part 2: Implementation and results,” *Proceedings of the Institution of Mechanical Engineers, Part K: Journal of Multi-body Dynamics*, vol. 217, pp. 213–223, 9 2003. [Online]. Available: <http://journals.sagepub.com/doi/10.1243/14644190360713560>
- [33] N. Sawalhi and R. B. Randall, “Simulating gear and bearing interactions in the presence of faults. part i. the combined gear bearing dynamic model and the simulation of localised bearing faults,” *Mechanical Systems and Signal Processing*, vol. 22, pp. 1924–1951, 2008.
- [34] J. Liu and Y. Shao, “Vibration modelling of nonuniform surface waviness in a lubricated roller bearing,” *JVC/Journal of Vibration and Control*, vol. 23, pp. 1115–1132, 2017.
- [35] F. Nonato and K. L. Cavalca, “An approach for including the stiffness and damping of elastohydrodynamic point contacts in deep groove ball bearing equilibrium models,” *Journal of Sound and Vibration*, vol. 333, pp. 6960–6978, 2014. [Online]. Available: <http://dx.doi.org/10.1016/j.jsv.2014.08.011>

- [36] R. Gohar and H. Rahnejat, *Fundamentals of Tribology*. WORLD SCIENTIFIC (EUROPE), 9 2018. [Online]. Available: <https://www.worldscientific.com/worldscibooks/10.1142/q0152>
- [37] K. L. Johnson, *Contact Mechanics*. Cambridge University Press, 1985.
- [38] E. V. Zaretsky, “Rolling bearing life prediction, theory, and application,” *NASA/TP—2013-215305/REV1*, 2016. [Online]. Available: <https://ntrs.nasa.gov/api/citations/20160013905/downloads/20160013905.pdf>
- [39] H. Hertz, “On the contact of elastic solids,” *J. Reine Angew. Math.*, vol. 92, pp. 156–171, 1881.
- [40] S. Kabus, M. R. Hansen, and O. Mouritsen, “A new quasi-static cylindrical roller bearing model to accurately consider non-hertzian contact pressure in time domain simulations,” *Journal of Tribology*, vol. 134, pp. 1–10, 2012.
- [41] R. Teutsch and B. Sauer, “An alternative slicing technique to consider pressure concentrations in non-hertzian line contacts,” *Journal of Tribology*, vol. 126, pp. 436–442, 2004.
- [42] O. Reynolds, “On the theory of lubrication and its application to mr. lowe’s experiments,” *Philosophical Transactions of the Royal Society of London*, vol. 177, pp. 157–234, 1886. [Online]. Available: https://scholar.google.com/scholar?q=related:zTMHxIMaYncJ:scholar.google.com/&hl=en&as_sdt=0,39&as_ylo=1886&as_yhi=1886#0
- [43] H. M. Martin, “Lubrication of gear teeth,” *Engineering (London)*, vol. 102, pp. 119–121, 1916.
- [44] W. Peppler, “Untersuchung über die druckübertragung bei belasteten und geschmierten umlaufenden achsparallelen zylindern,” *Maschinenelemente-Tagung*, vol. 42, 1936.
- [45] A. Meldahl, “Contribution to theory of lubrication of gears and of stressing of lubricated flanks of gear teeth,” *Brown Boveri Review*, vol. 28, pp. 374–382, 1941.
- [46] E. K. Gatcombe, “Lubrication characteristics of involute spur gears—a theoretical investigation,” *Trans. ASME*, vol. 67, pp. 177–185, 1945.
- [47] A. N. Grubin, *Fundamentals of the Hydrodynamic Theory of Lubrication of Heavily Loaded Cylindrical Surfaces*, book no. 3 ed. Central Scientific Research Institute for Technology and Mechanical Engineering, 1949.

- [48] A. I. Petrusovich, “Fundamental conclusion from the contact-hydrodynamic theory of lubrication,” *Izv. Akad. Nauk. SSSR (OTN)*, vol. 2, p. 209, 1951.
- [49] D. Dowson and G. R. Higginson, “A numerical solution to the elastohydrodynamic problem,” *Journal of Mechanical Engineering Science*, vol. 1, pp. 6–15, 1959.
- [50] D. Dowson and G. Higginson, “New roller bearing lubrication formula,” *Engineering*, pp. 158–159, 1961.
- [51] D. Dowson and G. R. Higginson, *Elastohydrodynamic Lubrication*. Pergamon, 1966.
- [52] D. Dowson and S. Toyoda, “A central film thickness formula for elastohydrodynamic line contacts,” *Proceedings of the Fifth Leeds-Lyon Symposium on Tribology, Mechanical Engineering Publications*, pp. 60–65, 1978.
- [53] A. M. Ertel, “Hydrodynamic lubrication based on new principles,” *Akad. Nauk SSSR Prikladnaya Matematika i Mekhanika*, vol. 3, pp. 41–52, 1939.
- [54] H. P. Evans and R. W. Snidle, “Elastohydrodynamic lubrication of point contacts at heavy loads.” *Proceedings of The Royal Society of London, Series A: Mathematical and Physical Sciences*, vol. 382, pp. 183–199, 1982.
- [55] B. J. Hamrock and B. O. Jacobson, “Elastohydrodynamic lubrication of line contacts,” *ASLE Transactions*, vol. 27, pp. 275–287, 1984.
- [56] B. J. Hamrock and D. Dowson, “Isothermal elastohydrodynamic lubrication of point contacts - 1. theoretical formulation.” *J Lubr Technol Trans ASME*, vol. 98 Ser F, pp. 223–229, 1976.
- [57] R. J. Chittenden, D. Dowson, J. F. Dunn, and C. M. Taylor, “Theoretical analysis of the isothermal elastohydrodynamic lubrication of concentrated contacts. i. direction of lubricant entrainment coincident with the major axis of the hertzian contact ellipse.” *Proceedings of The Royal Society of London, Series A: Mathematical and Physical Sciences*, vol. 397, pp. 245–269, 1985.
- [58] H. Okamura, *A contribution to the numerical analysis of isothermal elastohydrodynamic lubrication*. Elsevier, 1983, pp. 313–320.
- [59] L. G. Houptert and B. J. Hamrock, “Fast approach for calculating film thicknesses and pressures in elastohydrodynamically lubricated contacts at high loads.” *Journal of Tribology*, vol. 108, pp. 411–419, 1986.

- [60] A. A. Lubrecht, W. E. T. Napel, and R. Bosma, “Multigrid, an alternative method for calculating film thickness and pressure profiles in elastohydrodynamically lubricated line contacts,” *Journal of Tribology*, vol. 108, pp. 551–556, 1986.
- [61] C. H. Venner, W. E. ten Napel, and R. Bosma, “Advanced multilevel solution of the ehl line contact problem,” *Journal of Tribology*, vol. 112, pp. 426–431, 7 1990. [Online]. Available: <https://asmedigitalcollection.asme.org/tribology/article/112/3/426/435217/Advanced-Multilevel-Solution-of-the-EHL-Line>
- [62] F. Chevalier, A. A. Lubrecht, P. M. E. Cann, F. Colin, and G. Dalmaz, “Starvation phenomena in ehl point contacts: Influence of inlet flow distribution,” *Proceedings of 22nd Leeds-Lyon Symposium on Tribology, Elseviers Tribology Series*, vol. 31, pp. 213–233, 1995.
- [63] P. M. Lutz and G. E. Morales-Espejel, “A review of elasto-hydrodynamic lubrication theory,” *Tribology Transactions*, vol. 54, pp. 470–496, 3 2011. [Online]. Available: <http://www.tandfonline.com/doi/abs/10.1080/10402004.2010.551804>
- [64] P. E. Wolveridge, K. P. Baglin, and J. F. Archard, “The starved lubrication of cylinders in line contact,” *Proceedings of the Institution of Mechanical Engineers*, vol. 185, pp. 1159–1169, 6 1970. [Online]. Available: http://journals.sagepub.com/doi/10.1243/PIME_PROC_1970_185_126_02
- [65] B. J. Hamrock and D. Dowson, “Isothermal elastohydrodynamic lubrication of point contacts - 4. starvation results.” *American Society of Mechanical Engineers (Paper)*, pp. 223–228, 1976.
- [66] P. Yang, S. Qu, Q. Chang, and F. Guo, “On the theory of thermal elastohydrodynamic lubrication at high slide-roll ratios - line contact solution,” *Journal of Tribology*, vol. 123, pp. 36–41, 2001.
- [67] K. H. Kim and F. Sadeghi, “Three-dimensional temperature distribution in ehd lubrication: Part i—circular contact,” *Journal of Tribology*, vol. 114, pp. 32–41, 1 1992. [Online]. Available: <https://asmedigitalcollection.asme.org/tribology/article/114/1/32/435058/ThreeDimensional-Temperature-Distribution-in-EHD>
- [68] ——, “Three-dimensional temperature distribution in ehd lubrication: Part ii—point contact and numerical formulation,” *Journal*

- of Tribology, vol. 115, pp. 36–45, 1 1993. [Online]. Available: <https://asmedigitalcollection.asme.org/tribology/article/115/1/36/435348/ThreeDimensional-Temperature-Distribution-in-EHD>
- [69] X. Liu and P. Yang, “Analysis of the thermal elastohydrodynamic lubrication of a finite line contact,” *Tribology International*, 2002.
- [70] D. Zhu and S. zhu Wen, “A full numerical solution for the thermoelastohydrodynamic problem in elliptical contacts,” *Journal of Tribology*, vol. 106, pp. 246–254, 4 1984. [Online]. Available: <https://asmedigitalcollection.asme.org/tribology/article/106/2/246/435892/A-Full-Numerical-Solution-for-the>
- [71] W. Habchi, D. Eyheramendy, S. Bair, P. Vergne, and G. Morales-Espejel, “Thermal elastohydrodynamic lubrication of point contacts using a newtonian/generalized newtonian lubricant,” *Tribology Letters*, vol. 30, pp. 41–52, 2008.
- [72] R. Larsson, *EHL Film Thickness Behavior*. Springer US, 2013, pp. 817–827. [Online]. Available: http://link.springer.com/10.1007/978-0-387-92897-5_639
- [73] Y. H. Ali, R. A. Rahman, and R. I. R. Hamzah, “Artificial neural network model for monitoring oil film regime in spur gear based on acoustic emission data,” *Shock and Vibration*, vol. 2015, 2015.
- [74] I. Argatov, “Artificial neural networks (anns) as a novel modeling technique in tribology,” *Frontiers in Mechanical Engineering*, vol. 5, pp. 1–9, 2019.
- [75] E. O. Ezugwu, S. J. Arthur, and E. L. Hines, “Tool-wear prediction using artificial neural networks,” *Journal of Materials Processing Tech.*, vol. 49, pp. 255–264, 1995.
- [76] K. L. Rutherford, P. W. Hatto, C. Davies, and I. M. Hutchings, “Abrasive wear resistance of tin/nbn multi-layers: Measurement and neural network modelling,” *Surface and Coatings Technology*, vol. 86-87, pp. 472–479, 1996.
- [77] S. P. Jones, R. Jansen, and R. L. Fusaro, “Preliminary investigation of neural network techniques to predict tribological properties,” *Tribology Transactions*, vol. 40, pp. 312–320, 1997.
- [78] K. Genel, S. C. Kurnaz, and M. Durman, “Modeling of tribological properties of alumina fiber reinforced zinc-aluminum composites using artificial neural network,” *Materials Science and Engineering A*, vol. 363, pp. 203–210, 2003.

- [79] M. Hayajneh, A. M. Hassan, A. Alrashdan, and A. T. Mayyas, “Prediction of tribological behavior of aluminum-copper based composite using artificial neural network,” *Journal of Alloys and Compounds*, vol. 470, pp. 584–588, 2009.
- [80] Z. Zhang, K. Friedrich, and K. Velten, “Prediction on tribological properties of short fibre composites using artificial neural networks,” *Wear*, vol. 252, pp. 668–675, 2002.
- [81] L. Cavaleri, P. G. Asteris, P. P. Psyllaki, M. G. Douvika, A. D. Skentou, and N. M. Vaxevanidis, “Prediction of surface treatment effects on the tribological performance of tool steels using artificial neural networks,” *Applied Sciences (Switzerland)*, vol. 9, 2019.
- [82] S. Bhaumik, S. D. Pathak, S. Dey, and S. Datta, “Artificial intelligence based design of multiple friction modifiers dispersed castor oil and evaluating its tribological properties,” *Tribology International*, vol. 140, p. 105813, 2019.
- [83] J. E. Otero, E. de la Guerra Ochoa, E. C. Tanarro, P. L. Morgado, A. D. Lantada, J. M. Munoz-Guijosa, and J. L. M. Sanz, “Artificial neural network approach to predict the lubricated friction coefficient,” *Lubrication Science*, vol. 26, pp. 141–162, 4 2014. [Online]. Available: <https://onlinelibrary.wiley.com/doi/10.1002/ls.1238>
- [84] M. Afrand, K. N. Najafabadi, N. Sina, M. R. Safaei, A. Kherbeet, S. Wongwises, and M. Dahari, “Prediction of dynamic viscosity of a hybrid nano-lubricant by an optimal artificial neural network,” *International Communications in Heat and Mass Transfer*, vol. 76, pp. 209–214, 8 2016. [Online]. Available: <https://linkinghub.elsevier.com/retrieve/pii/S0735193316301610>
- [85] M. H. Esfe, H. Rostamian, S. Esfandeh, and M. Afrand, “Modeling and prediction of rheological behavior of al₂o₃-mwcnt/5w50 hybrid nano-lubricant by artificial neural network using experimental data,” *Physica A: Statistical Mechanics and its Applications*, vol. 510, pp. 625–634, 2018.
- [86] M. Ripa and L. Frangiu, “A survey of artificial neural networks applications in wear and manufacturing processes,” *Journal of Tribology*, pp. 35–42, 2004.
- [87] S. Panda, D. Chakraborty, and S. Pal, “Flank wear prediction in drilling using back propagation neural network and radial basis function network,” *Applied Soft Computing*, vol. 8, pp. 858–871, 3 2008. [Online]. Available: <https://linkinghub.elsevier.com/retrieve/pii/S1568494607000762>

- [88] I. Asiltürk and M. Çunkaş, “Modeling and prediction of surface roughness in turning operations using artificial neural network and multiple regression method,” *Expert Systems with Applications*, vol. 38, pp. 5826–5832, 2011.
- [89] J. G. A. Barbedo, “Impact of dataset size and variety on the effectiveness of deep learning and transfer learning for plant disease classification,” *Computers and Electronics in Agriculture*, vol. 153, pp. 46–53, 10 2018. [Online]. Available: <https://linkinghub.elsevier.com/retrieve/pii/S0168169918304617>
- [90] N. Wang and C. M. Tsai, “Assessment of artificial neural network for thermohydrodynamic lubrication analysis,” *Industrial Lubrication and Tribology*, vol. 72, pp. 1233–1238, 2020.
- [91] A. Almqvist, “Fundamentals of physics-informed neural networks applied to solve the reynolds boundary value problem,” *Lubricants*, vol. 9, p. 82, 8 2021. [Online]. Available: <https://www.mdpi.com/2075-4442/9/8/82>
- [92] M. Marian, J. Mursak, M. Bartz, F. J. Profito, A. Rosenkranz, and S. Wartzack, “Predicting ehl film thickness parameters by machine learning approaches,” *Friction*, 6 2022. [Online]. Available: <https://link.springer.com/10.1007/s40544-022-0641-6>
- [93] X. Hao, J. Zhai, J. Liang, Y. Chen, and Q. Han, “Time-varying stiffness characteristics of roller bearing influenced by thermal behavior due to surface frictions and different lubricant oil temperatures,” *Tribology International*, vol. 144, p. 106125, 2020. [Online]. Available: <https://doi.org/10.1016/j.triboint.2019.106125>
- [94] N. Akemi, H. Tsuha, and K. L. Cavalca, “Finite line contact stiffness under elastohydrodynamic lubrication considering linear and nonlinear force models,” *Tribology International*, p. 106219, 2020. [Online]. Available: <https://doi.org/10.1016/j.triboint.2020.106219>
- [95] F. Wang, M. Jing, J. Yi, G. Dong, H. Liu, and B. Ji, “Dynamic modelling for vibration analysis of a cylindrical roller bearing due to localized defects on raceways,” *Proceedings of the Institution of Mechanical Engineers, Part K: Journal of Multi-body Dynamics*, vol. 229, pp. 39–64, 2015.
- [96] J. Liu, Z. Shi, and Y. Shao, “An analytical model to predict vibrations of a cylindrical roller bearing with a localized surface defect,” *Nonlinear Dynamics*, vol. 89, pp. 2085–2102, 2017.

- [97] Y. Guo and J. Keller, “Validation of combined analytical methods to predict slip in cylindrical roller bearings,” *Tribology International*, vol. 148, p. 106347, 2020. [Online]. Available: <https://doi.org/10.1016/j.triboint.2020.106347>
- [98] R. Gohar, *Elastohydrodynamics*. Imperial College Press, 1988.
- [99] M. Denni, N. Biboulet, V. Abousleiman, and A. A. Lubrecht, “Dynamic study of a roller bearing in a planetary application considering the hydrodynamic lubrication of the roller/cage contact,” *Tribology International*, vol. 149, p. 105696, 2019. [Online]. Available: <https://doi.org/10.1016/j.triboint.2019.03.054>
- [100] T. L. H. Walford and B. J. Stone, “The sources of damping in rolling element bearings under oscillating conditions,” *Proceedings of the Institution of Mechanical Engineers, Part C: Journal of Mechanical Engineering Science*, vol. 197, pp. 225–232, 10 1983. [Online]. Available: http://journals.sagepub.com/doi/10.1243/PIME_PROC_1983_197_102_02
- [101] D. W. Dareing and K. L. Johnson, “Fluid film damping of rolling contact vibrations,” *Journal of Mechanical Engineering Science*, vol. 17, pp. 214–218, 8 1975. [Online]. Available: http://journals.sagepub.com/doi/10.1243/JMES_JOUR_1975_017_031_02
- [102] H. Mehdigoli, H. Rahnejat, and R. Gohar, “Vibration response of wavy surfaced disc in elastohydrodynamic rolling contact,” *Wear*, vol. 139, pp. 1–15, 1990.
- [103] J. Walker, H. Questa, S. R. Bewsher, C. Schweiger, and M. Sopouch, “Experimental design for characterization of force transmissibility through bearings in electric machines and transmissions,” in *10th International Styrian Noise, Vibration & Harshness Congress: The European Automotive Noise Conference*, 2018, pp. 1–6.
- [104] R. Takeda, G. Lisco, T. Fujisawa, L. Gastaldi, H. Tohyama, and S. Tadano, “Drift removal for improving the accuracy of gait parameters using wearable sensor systems,” *Sensors*, vol. 14, pp. 23 230–23 247, 12 2014. [Online]. Available: <http://www.mdpi.com/1424-8220/14/12/23230>
- [105] B. J. Hamrock and D. Dowson, *Ball Bearing Lubrication: The Elastohydrodynamics of Elliptical Contacts*. John Wiley and Sons, 1981.
- [106] H. Rahnejat, “Influence of vibration on the oil film in concentrated contacts,” Ph.D. dissertation, 1984.

- [107] J. A. Greenwood and J. H. Tripp, “The contact of two nominally flat rough surfaces,” *Proceedings of the Institution of Mechanical Engineers*, vol. 185, pp. 625–633, 1970.
- [108] C. R. Evans and K. L. Johnson, “Regimes of traction in elastohydrodynamic lubrication,” *Proceedings of the Institution of Mechanical Engineers, Part C: Journal of Mechanical Engineering Science*, vol. 200, p. 313–324, 1986.
- [109] K. A. Hoffmann and S. T. Chiang, *Computational Fluid Dynamics*, 4th ed. Engineering Education System, 2000.
- [110] C. Barus, “Isothermals isopietics and isometrics in relationship to viscosity,” *American Journal of Science 3rd Series*, vol. 45, pp. 87–96, 1893.
- [111] R. Gohar and H. Rahnejat, *Fundamentals of Tribology*, 3rd ed. World Scientific Publishing Europe Ltd., 2019.
- [112] C. Roelands, “Correlational aspects of the viscosity-temperature-pressure relationship of lubricating oils,” Ph.D. dissertation, 1966.
- [113] L. Houpert, “New results of traction force calculations in elastohydrodynamic contacts.” vol. 107, pp. 241–245, 1984.
- [114] D. Dowson and G. Higginson, *Elasto-hydrodynamic lubrication*. Pergamon Press, 1977.
- [115] R. F. Crouch and A. Cameron, “Viscosity-temperature equations for lubricants,” *J. Inst. Petroleum*, vol. 47, pp. 307–313, 1961.
- [116] M. Masjedi and M. M. Khonsari, “Film thickness and asperity load formulas for line-contact elastohydrodynamic lubrication with provision for surface roughness,” *Journal of Tribology*, vol. 134, 1 2012. [Online]. Available: <https://asmedigitalcollection.asme.org/tribology/article/doi/10.1115/1.4005514/439343/Film-Thickness-and-Asperity-Load-Formulas-for>
- [117] R. G. Budynas and J. K. Nisbett, *Shigley’s Mechanical Engineering Design*, 9th ed. McGraw-Hill, 2011.
- [118] B. J. Hamrock, “Film thickness for different regimes of fluid-film lubrication,” pp. 1–14, 1980.
- [119] G. Lundberg and E. Yhland, *Cylinder compressed between two plane bodies*. SKF, 1949.

- [120] T. Parikyan, T. Resch, and H. H. Priebsch, “Structured model of crankshaft in the simulation of engine dynamics with avl/excite,” in *Volume 3: Engine Systems: Lubrication, Components, Exhaust and Boosting, System Design and Simulation*, vol. 67. American Society of Mechanical Engineers, 9 2001, pp. 105–114. [Online]. Available: <https://asmedigitalcollection.asme.org/ICEF/proceedings/ICEF2001/80159/105/1081821>
- [121] G. Offner, “Modelling of condensed flexible bodies considering non-linear inertia effects resulting from gross motions,” *Proceedings of the Institution of Mechanical Engineers, Part K: Journal of Multi-body Dynamics*, vol. 225, pp. 204–219, 2011.
- [122] D. Nelia, I. Bercea, and V. Paleu, “Prediction of roller skewing in tapered roller bearings,” *Tribology Transactions*, vol. 51, pp. 128–139, 2008.
- [123] F. Majdoub, L. Saunier, C. Sidoroff-coicaud, and B. Mevel, “Tribology international experimental and numerical roller skew in tapered roller bearings,” *Tribology International*, vol. 145, p. 106142, 2020. [Online]. Available: <https://doi.org/10.1016/j.triboint.2019.106142>
- [124] B. Mevel and J. L. Guyader, “Routes to chaos in ball bearings,” pp. 471–487, 1993.
- [125] H. Spikes, “Basics of ehl for practical application,” *Lubrication Science*, vol. 27, pp. 45–67, 2015.
- [126] X. Shi and L. Wang, “Tehl analysis of high-speed and heavy-load roller bearing with quasi-dynamic characteristics,” *Chinese Journal of Aeronautics*, vol. 28, pp. 1296–1304, 8 2015. [Online]. Available: <http://dx.doi.org/10.1016/j.cja.2015.06.013><https://linkinghub.elsevier.com/retrieve/pii/S1000936115001181>
- [127] K. P. Singh and B. Paul, “Numerical solution of non-hertzian elastic contact problems,” *Journal of Applied Mechanics*, vol. 41, pp. 484–490, 6 1974. [Online]. Available: <https://asmedigitalcollection.asme.org/appliedmechanics/article/41/2/484/422784/Numerical-Solution-of-NonHertzian-Elastic-Contact>
- [128] T. A. Harris and M. N. Kotzales, *Advanced Concepts of Bearing Technology*, 5th ed. Taylor and Francis Group, 2007.
- [129] J. M. de Mul, J. J. Kalker, and B. Fredriksson, “The contact between arbitrarily curved bodies of finite dimensions,” *Journal of Tribology*, vol. 108, pp. 140–148, 1 1986. [Online]. Available: <https://asmedigitalcollection.asme.org/tribology/article/108/1/140/418690/The-Contact-Between-Arbitrarily-Curved-Bodies-of>

- [130] Y. Mitsuya, H. Sawai, M. Shimizu, and Y. Aono, “Damping in vibration transfer through deep-groove ball bearings,” *Transactions of the Japan Society of Mechanical Engineers Series C*, vol. 58, pp. 3714–3721, 1992.
- [131] E. Krämer, *Dynamics of Rotors and Foundations*. Springer Berlin Heidelberg, 1993. [Online]. Available: <http://link.springer.com/10.1007/978-3-662-02798-1>
- [132] D. Dowson, “Paper 10: Elastohydrodynamics,” *Proceedings of the Institution of Mechanical Engineers, Conference Proceedings*, 1967.
- [133] D. Sarkar, R. Bali, and T. Sharma, *Practical Machine Learning with Python: A Problem-Solver’s Guide to Building Real-World Intelligent Systems*. Apress L.P., 12 2017.
- [134] J. Bell, *Machine Learning: Hands-On for Developers and Technical Professionals*, 1st ed. Wiley, 11 2014.
- [135] C. M. Bishop, *Pattern Recognition and Machine Learning*. Springer, 2006, pp. 21–24.
- [136] K. Levenberg, “A method for the solution of certain non-linear problems in least squares,” *Quarterly of Applied Mathematics*, vol. 2, pp. 164–168, 1944. [Online]. Available: <https://about.jstor.org/terms>
- [137] D. W. Marquardt, “An algorithm for least-squares estimation of nonlinear parameters,” *Journal of the Society for Industrial and Applied Mathematics*, vol. 11, pp. 431–441, 1963.
- [138] B. M. Wilamowski and H. Yu, “Improved computation for levenberg–marquardt training,” *IEEE Transactions on Neural Networks*, vol. 21, pp. 930–937, 6 2010. [Online]. Available: <http://ieeexplore.ieee.org/document/5451114/>
- [139] M. Marian and S. Tremmel, “Current trends and applications of machine learning in tribology—a review,” *Lubricants*, vol. 9, p. 86, 9 2021. [Online]. Available: <https://www.mdpi.com/2075-4442/9/9/86>
- [140] X. Ying, “An overview of overfitting and its solutions,” *Journal of Physics: Conference Series*, vol. 1168, p. 022022, 2 2019. [Online]. Available: <https://iopscience.iop.org/article/10.1088/1742-6596/1168/2/022022>
- [141] J. Han and C. Moraga, *The influence of the sigmoid function parameters on the speed of backpropagation learning*, 1995, pp. 195–201. [Online]. Available: http://link.springer.com/10.1007/3-540-59497-3_175

- [142] S. Sharma, S. Sharma, and A. Athaiya, “Activation functions in neural networks,” *International Journal of Engineering Applied Sciences and Technology*, vol. 4, pp. 310–316, 2020. [Online]. Available: <http://www.ijeast.com>
- [143] T. M. Inc., “Improve shallow neural network generalization and avoid overfitting,” 2022. [Online]. Available: <https://uk.mathworks.com/help/deeplearning/ug/improve-neural-network-generalization-and-avoid-overfitting.html>
- [144] R. Preece and J. V. Milanovic, “Efficient estimation of the probability of small-disturbance instability of large uncertain power systems,” *IEEE Transactions on Power Systems*, vol. 31, pp. 1063–1072, 3 2016. [Online]. Available: <http://ieeexplore.ieee.org/document/7084698/>
- [145] K. Siebertz, D. van Bebber, and T. Hochkirchen, *Statistische Versuchsplanung*. Springer Berlin Heidelberg, 6 2017. [Online]. Available: <http://link.springer.com/10.1007/978-3-662-55743-3>
- [146] M. E. Johnson, L. M. Moore, and D. Ylvisaker, “Minimax and maximin distance designs,” Tech. Rep., 1990.
- [147] K. L. Johnson, “Regimes of elastohydrodynamic lubrication,” *Journal of Mechanical Engineering Science*, vol. 12, pp. 9–16, 2 1970. [Online]. Available: http://journals.sagepub.com/doi/10.1243/JMES_JOUR_1970_012_004_02